Title
Structure and Ion Transport in Hybrid Organic-Inorganic Copolymer Electrolytes

Author
Sethi, Gurmukh Kaur

Publication Date
2021

Structure and Ion Transport in Hybrid Organic-Inorganic Copolymer Electrolytes

By
Gurmukh Kaur Sethi

A dissertation submitted in partial satisfaction of the

requirements for the degree of

Doctor of Philosophy

in

Engineering- Materials Science and Engineering

in the

Graduate Division

of the

University of California, Berkeley

Committee in charge:

Professor Andrew M. Minor, Chair
Professor Nitash P. Balsara
Professor Mary Scott

Summer 2021

1. Abstract

Structure and Ion Transport in Hybrid Organic-Inorganic Copolymer Electrolytes

by

Gurmukh Kaur Sethi

Doctor of Philosophy in Engineering- Materials Science and Engineering

University of California, Berkeley

Professor Andrew M. Minor, Chair

Block copolymers mixed with lithium salts are promising electrolyte materials for next-generation lithium batteries. One block can aid in the transport of ions, while the other block can provide improved mechanical strength to counteract lithium dendritic growth, a common failure mechanism of lithium metal batteries. Block copolymers often exhibit microphase separation of the two blocks due to thermodynamic repulsions between the two unlike chemical moieties. Understanding the correlations between structure, salt concentration, mechanical strength, and ion transport is important for improving the performance of polymer electrolytes. Significant work in characterization of structure and ion transport has been performed in all-organic diblock copolymers mixed with lithium salts, namely, polystyrene-*block*-poly(ethylene oxide) (PS-*b*-PEO; SEO) and lithium *bis*(trifluoromethanesulfonyl) imide (LiTFSI). However, there is an emerging interest in replacing the mechanically rigid block with an inorganic material, such as polyhedral oligomeric silsesquioxane (POSS). POSS represents a silica caged structure with molecular weight close to 1 kg mol^{-1} and molecular size of 1 nm.

In this dissertation, mixtures of poly(ethylene oxide)-*block*- acryloisobutyl polyhedral oligomeric silsesquioxane (PEO-POSS) and acryloisobutyl polyhedral oligomeric silsesquioxane)-*block*- poly(ethylene oxide)-*block*- acryloisobutyl polyhedral oligomeric silsesquioxane (POSS-PEO-POSS) with LiTFSI are studied. PEO provides good ion solvation and transport, while POSS increases the modulus. PEO-POSS/LiTFSI and POSS-PEO-POSS/LiTFSI microphase separate into distinct morphologies which are a strong function of volume fraction, chain length, salt concentration, and temperature that differ from the phase behavior of SEO/LiTFSI. We study the relationships between the morphology, salt concentration, shear moduli, crystallinity of the POSS block, and ion-transport using small/wide angle X-ray scattering, electron microscopy, ac impedance spectroscopy, chronoampotherapy and rheology. Experiments show that PEO-POSS/LiTFSI and POSS-PEO-POSS/LiTFSI tends to segregate more strongly with increasing temperature, opposite of SEO/LiTFSI. The morphology is strongly dependent upon the crystallization of the POSS block. Block structure and morphology both, in turn, effect the electrochemical properties and the limiting current density.

Table of Contents

List of Figures

List of Tables

Acknowledgements

Thank you, first and foremost, to my family. Thank you, Mom. You were a constant emotional support during every milestone and challenge. I owe all of my accomplishments to your encouragement. Thank you to my one and only sister, Arshey. Your frequent life advice helped me to balance research and being a person. Your intuition has helped me in countless situations. Thank you, Richie, for your kindness. I immensely enjoy all the time I can spend with you and Nina. Thank you, Dada and Dadi. You have taught me the meaning of hard work, tenacity, and family. Your constant support and love were instrumental in my ability to pursue my dreams.

Thank you, Joe, for being my travel companion, partner, and best friend.

Thank you to my research adviser, Dr. Nitash Balsara. Nitash, I learned so much from your mentorship and support during my PhD. Thank you for building a collaborative and safe environment. I am very lucky be a member of the Balsara Lab.

Thank you to my research co-adviser, Dr. Irune Villaluenga. The work demonstrated in this thesis was entirely possible because of you. You dedicated so much time and effort in my education, and I will do my best to pay this forward. I will always consider myself your first graduate student. I wish you every success as a professor.

Thank you to the members of my dissertation committee, co-adviser Dr. Andrew Minor and Dr. Mary Scott. You have helped me throughout my career and have been instrumental to my growth as a researcher.

Thank you to those that inspired my love of research and ambition to pursue a PhD. Dr. Andrea Armani, you were an amazing undergraduate research adviser. You inspired me to pursue a career in research. Thank you to the PhD and post-doc members of the Armani lab for your mentorship: Dr. Alexa Hudnut, Dr. Andre Kovach, Dr. Victoria Sun, Dr. Vinh Diep (fellow fellow), Dr. Samantha McBirney, Dr. Michele Lee, Dr. Soheil Soltani (for countless hours in the cleanroom), Samuel Kushner-Lenhoff, and Dr. Simin Mehrabani. Dr. Nishita Deka and Audrey Harker, thank you for your help paving my path to Berkeley (Armani lab North). Thank you, Lea Fang and Martin Siron, for being my partners in crime during our undergraduate research in the Armani lab.

Dr. Michael Sailor, thank you for mentoring me as a high school student in your laboratory. This inspired me to pursue my PhD.

Thank you to all members of the Balsara lab, past and present, that I have had the pleasure to work with. Mahati, thank you for offering me great advice that aided in my decision to join this graduate program. Your exuberance and happiness inspire me. Katherine, thank you for being so honest in your advice as well as going out of your way to include me in Balsara lab culture. Kevin, your general insights to graduate school helped me adjust quickly. Jacob, you gave me great tips early on in my graduate work that saved me a lot of beating my head against the wall. Thank you for being a great thermodynamics teacher. Doug, I appreciated your insights into my research and your awesome rain gear.

Alex, I admired your diligence in research. Adri, thank you for patiently teaching me how to use the rheometer and mentoring me in Tan Hall.

Danielle, thank you for your mentorship. You taught me so much about how to maintain a lab, perform research efficiently, and become an adult. Prepping for your engagement photo shoot in the 62 office, making ice cream runs in summer, and trying to decode cryptic emoji texts were my favorite memories. Ksenia, thank you for your friendship and mentorship. I consider the massive hotel suite at APS in New Orleans as the place we became friends. I admire your work ethic and your incredible intelligence. Rita, you were such a great friend to have in the 62 lab. I loved having conversations in the offices and trips to the botanical gardens. You were always quick to lend a hand to any task.

Jackie, thank you for your blunt honesty and your friendship. I admire your tastes in food and your skills in softball. Whitney, we have had so many fun times including Mura Masa concerts and pre-gaming in Tan hall. I am excited to follow your career. Deep, thank you for being my first friend in the Balsara lab and for helping me adjust to life in Berkeley.

Mike, thank you for being my partner in crime. I like to think that your level-headedness and my craziness averaged out to two normal graduate students.

Kevin, your contribution to the lab have been very impressive, and I am excited to follow your successes. Lorena, thank you for being such an amazing friend. I have enjoyed all of our research-related and non-research related conversations. Your ability to simplify complex topics in presentations is truly admirable.

Alec, your work and contributions to Balsara lab research are truly outstanding. I am glad I was able to get to know you in the 62 lab. Zach, you have really gone above and beyond as a leader in the Balsara lab. It has been amazing to see how much responsibility you have taken on so quickly. Neel, your growth as a researcher has been immense. Thank you for all of your kindness.

Darby, thank you for being such a positive presence in the lab. You are kind-hearted, smart, and it has been a pleasure to get to know you. Morgan, I am astounded by how great of a researcher you have become in such a short time. I am excited to see you both take a leading role in maintaining the Balsara lab culture.

Karim, I appreciate your taste in music and your vigor for life. I am excited to see you mold the future culture of the Balsara lab. Vivaan, you have been an amazing mentee. I am so thrilled with all of your results so far, and I cannot wait to follow your career. Thank you for all of your hard work.

Thank you, Xi, for your willingness to collaborate on research projects. I am honored to have worked with someone so talented. Hee Jeung, I am very lucky to have worked alongside you. Your quiet determination and skill were a force to be reckoned with. I am excited to follow your successful career as a professor. Louise, I am so grateful to call you a friend and a labmate. Your cheerfulness is contagious and baking skills are superb. Thank you for encouraging me to study abroad and travel. I could not have done much of this work without your enthusiasm and support. Kim, thank you for sharing your love of rock climbing with me and helping me with my research. Your kindness and friendliness is unparalleled. Youngwoo, I am so grateful to have been your labmate. Your patience, care of the lab, and diligence was aspirational. Xiaopeng, it has been a pleasure getting to know you. I am inspired by your hard work and dedication to research during the pandemic times. David, thank you for all of your contributions to the NMR research in our lab. I thoroughly enjoy all of the memes you post to the Balsara lab slack.

Thank you to the undergraduates in the Balsara lab. Daniel, I appreciate your hard-work, sense of humor, and taste in music. Rohan, thank you for your hard work and diligence. I really appreciated your contributions to this work. Simar, you taught me so much. Thank you for helping me with electrochemistry and for being a great friend.

Thank you, Dr. Renaud Bouchet and Dr. Didier Devaux, for hosting me at Le Laboratoire d'Electrochimie et de Physicochimie des Matériaux et des Interfaces (LEPMI) at Grenoble Institut d'ingénierie et de management (INP), Université Grenoble Alpes in Grenoble, France. I learned about electrochemistry, full cell characterization, and solid-state batteries under your guidance. Thank you, Roselyne Jeanne-Brou and Jamie Isaac for your research help and friendship. This collaboration was supported by funding from the National Science Foundation Graduate Research Opportunities Worldwide Program.

Thank you to the beamline scientists who have supported this work at the Advanced Light Source, Beamline 7.3.3., Eric Schaible and Chenhui Zhu, as well as the beamline scientists

at Stanford Synchrotron Radiation Lightsource Beamline 1-5, Christopher Tassone and Tim Dunn.

My tuition and stipend have been supported by funding from the National Science Foundation Graduate Student Research Fellowship.

This dissertation is dedicated to my father, Sarmeet Singh Sethi.

1. Introduction

1.1 Motivation

It is necessary to improve renewable energy sources to meet increasing societal energy requirements. However, meeting this demand with a fossil-fuel economy will lead to severe environmental impact, including greenhouse gas emissions and deterioration of air-quality.[1–3] Long-life, low-cost reliable batteries are required to enable renewable energy storage and mitigate environmental impact. Although a commercial success, lithium-ion batteries containing a lithiated carbon anode and a lithium intercalation cathode have limitations. Only incremental improvements are possible without changing the battery chemistry.[4–8] Further, the commonly used cyclic and linear carbonates mixed with a lithium salt electrolytes used in lithium-ion battery pose an inherent safety risk due to high volatility and flammability.

One proposed solution is a solid-state battery, wherein the lithiated carbon/graphite anode is replaced by high energy density lithium metal.[9,10] However, this chemistry has not been widely commercially adopted due to uncontrollable lithium dendrite growth inducing poor cycling efficiency and safety concerns.[11–20] One strategy for enabling the lithium metal anode as well as increasing battery safety, is the implementation of non-liquid electrolytes.[21–27] One example is a polymer electrolyte, composed of a polymer and a lithium salt, have the potential to improve battery safety as they have high chemical stability and low vapor pressures.[28] It is difficult to find a single polymer electrolyte that has the aforementioned properties, in addition to high ionic conductivity and mechanical strength. Multiple chemical functionalities can be incorporated through endgroup modification or block architectures.[29,30] In this dissertation, the ion transport and structure-function properties of block copolymer electrolytes comprising mixtures of poly (ethylene oxide)-*block*-poly(acryloisobutyl polyhedral oligomeric silsesquioxane) and lithium salt are examined for high energy density lithium metal batteries.

1.2 Polymer electrolytes

Due to promising properties for battery technologies, polymer electrolytes have been studied since 1973, where Fenton *et. al.* demonstrated the ability of ether oxide-containing polymers to form stable complexes with salt.[31] The most prominent polymer electrolyte comprises poly(ethylene oxide) (PEO) mixed with lithium bis(trifluoromethanesulfonyl)imide (LiTFSI) salt.[32] In this system, lithium ions are coordinated by six ether oxygens.[33,34] Ions are typically transported by one of two mechanisms: backbone diffusion, where the ions travel with movement of the polymer chain, and segmental motion, where ions "hop" between solvation sites in the electrolyte.[35]

Segmental motion is the primary ion transport mechanism at higher polymer molecular weights (the entanglement threshold in PEO is 5,000 g/mol).[36,37] Newman's concentrated solution theory suggests that a polymer electrolyte containing a salt can be fully electrochemically characterized with the measurement of three independent ion transport coefficients and a thermodynamic factor.[38] Systematic studies of amorphous PEO/LiTFSI have been performed to fully describe the electrochemical properties at a variety of molecular weights above the entanglement threshold and salt concentrations.[39–41]

A limitation of PEO-based polymer electrolytes for electrochemical cells containing a lithium metal anode is the unstable deposition of lithium during discharge due to insufficient electrolyte mechanical strength. Monroe and Newman proposed that dendrite growth is suppressed when electrolyte modulus is on the order of MPa.[42,43] Barai and coworkers performed simulations to estimate the magnitude of applied current density as well as electrolyte modulus to enable stable lithium deposition.[44] More recently, we have discovered that the time dependence of dendrite growth suggests the creep modulus may be a more important parameter in determining an electrolytes' ability to mechanically suppress lithium protrusions and prevent the growth of lithium dendrites.

One proposed solution is to augment the PEO chain with a mechanically rigid moiety or chain. The addition of chemical species to PEO can impede segmental mobility. Thus, when incorporating chemical groups that improve the mechanical of a polymer electrolyte, it is important to investigate the resulting change in ion transport. It can be thus advantageous to decouple the ion-transport and mechanical properties. Block copolymers microphase separate into separate ionically conductive and mechanically rigid channels.[45–47] The most commonly studied block copolymer electrolyte is an all organic system: polystyrene-*block*-poly(ethylene oxide) (SEO) mixed with LiTFSI salt.[48–52] The focus of the research presented in this dissertation is poly (ethylene oxide)-*block*-poly(acryloisobutyl polyhedral oligomeric silsesquioxane) (PEO-POSS) and poly(acryloisobutyl polyhedral oligomeric silsesquioxane)-*block*- poly (ethylene oxide)-*block*-poly(acryloisobutyl polyhedral oligomeric silsesquioxane) (POSS-PEO-POSS) mixed with LiTFSI. The polyhedral oligomeric silsesquioxane (POSS) block, used extensively as a nanofiller in polymer matrices, is expected to mechanically stabilize the PEO chain to a greater extent than the all-organic counterpart (we investigate this claim in Chapter 2 of this dissertation).[53,54] The objective of the work outlined here is to understand the correlations between salt concentration, block structure, mechanical strength, and ion transport in hybrid organic-inorganic block copolymer electrolytes.

1.3 Structure of the dissertation

The dissertation is organized as follows. Chapter 2 presents an overview of the phase behavior, ionic conductivity, and viscoelastic properties of PEO-POSS/LiTFSI mixtures. The phase behavior is examined when salt is added to PEO-POSS using small-angle X-ray scattering (SAXS). The mechanical and ion transport is measuring using rheology and impedance spectroscopy and compared to the all-organic polymer electrolyte counterpart.

To understand the unusual phase behavior demonstrated in Chapter 2, Chapter 3 examines the phase behavior of 24 PEO-POSS/LiTFSI mixtures. A model derived from Leibler's Gaussian Random Phase Approximation is used to determine segregation strength from disordered SAXS scattering profiles, with slight modifications to the theory to account for the rod-like behavior of the POSS block. One expression is derived to calculate the segregation strength as a function of temperature and salt concentration, and the resulting phase behavior is mapped onto a classical diblock copolymer phase diagram.

To understand the molecular underpinnings of the phase transitions shown in Chapters 2 and 3, Chapter 4 investigates the crystallization of the POSS block effect on phase behavior using SAXS in 2 PEO-POSS and 1 POSS-PEO-POSS block copolymer mixed with LiTFSI. Wide angle X-ray scattering (WAXS) is used to examine the crystal structure formed by POSS homopolymer and salt containing block copolymers. Differential scanning calorimetry (DSC) is employed to confirm melting/crystallization temperatures seen in WAXS as well as compare the percent crystallinity of the POSS block as a function of block structure, molecular weight, and salt concentration. This chapter shows that crystallization of the POSS block plays a large role in the order-disorder and order-order transitions in hybrid organic-inorganic block copolymer electrolytes.

The effect of order/disorder on ion transport properties is investigated in Chapter 5. The ability to extend Newman's concentrated solution theory to a block copolymer system to model salt concentration gradient formation as a function of applied current density is investigated. The experimentally determined limiting current density is compared to the predicted values in a PEO-POSS/LiTFSI system that is ordered as well as a POSS-PEO-POSS/LiTFSI system that is largely disordered over the experimental salt concentration window. It is shown that structure plays a large role in our ability to use three-component concentrated solution theory to describe microphase separated block copolymer electrolytes.

2. Self-Assembly, Ion Transport, and Mechanical Properties of Hybrid Inorganic-Organic Diblock Copolymer Electrolytes†

ABSTRACT

Nanostructured solid polymer electrolytes comprising ion-conducting domains and rigid non-conducting domains are obtained by block copolymer self-assembly. We report on the synthesis and characteristics of mixtures of a diblock copolymer with an organic and inorganic block: poly(ethylene oxide) -*b*- poly(acryloisobutyl polyhedral oligomeric silsesquioxane) (PEO-POSS) with a lithium salt. In the neat state, PEO-POSS exhibits a classical order-to-disorder transition upon heating. Dilute electrolytes exhibit a dramatic reversal; a disorder-to-order transition upon heating is obtained, indicating that the addition of salt fundamentally changes interactions between the organic and inorganic chains. At higher salt concentrations, the electrolytes primarily form a lamellar phase. Coexisting lamellae and cylinders are found at intermediate salt concentrations and high temperatures. The conductivity and shear modulus of PEO-POSS are significantly higher than that of an all-organic block copolymer electrolyte with similar molecular weight and morphology, demonstrating that organic-inorganic block copolymers provide a promising route for developing the next generation of solid electrolytes for lithium batteries.

2.1. Introduction

The performances of classical liquid electrolytes have made significant advances in the past two decades; however, the intrinsic instability of liquid electrolytes results in safety issues. One solution is a solid polymer electrolyte, which has greater stability in lithium batteries[31,55–57]. Nanostructured electrolytes containing both soft, ion-conducting domains and rigid non-conducting domains offer the opportunity to simultaneously tune both mechanical and electrical properties. Such electrolytes are conveniently made by block copolymer self-assembly[58]. Most of the block copolymer electrolytes studied thus far comprise organic polymer chains for both the conducting and rigid domains[59–62]. In principle, both conducting and non-conducting domains could be made from inorganic molecules. Nanostructured hybrid materials are often made via block copolymer self-assembly, either using the domain structure of block copolymers as a template for synthesizing confined inorganic domains or by attaching molecular structures such as polyhedral oligomeric silsesquioxane (POSS) to a polymerizable monomer unit.

[†] This chapter is reported in Sethi, G. K., Jiang, X., Chakraborty, R., Loo, W. S., Villaluenga, I. & Balsara, N. P. Anomalous Self-Assembly and Ion Transport in Nanostructured Organic–Inorganic Solid Electrolytes. *ACS Macro Lett.* 1056–1061 (2018). doi:10.1021/acsmacrolett.8b00583

While such composite materials have been studied extensively, we are not aware of any systematic study of the thermodynamic interactions between polymers wherein one of the components contains an inorganic moiety. A fundamental understanding of self-assembly in such systems begins with the quantification of these interactions.

In this chapter, we report on the synthesis and characterization of a poly(ethylene oxide) -*b*- poly (acryloisobutyl polyhedral oligomeric silsesquioxane) (PEO-POSS) block copolymer. The block copolymer was synthesized using nitroxide mediated radical polymerization of a POSS containing monomer (isobutyl POSS-acrylate) using BlocBuilder functionalized PEO as the macroinitiator. The chemical structure of PEO-POSS is shown in Figure 2.1. Electrolytes were prepared by mixing lithium bis(trifluoromethane)sulfonimide (LiTFSI) salt into the block copolymer. We demonstrate that the neat block copolymer exhibits an order-to-disorder transition (ODT) upon heating. Adding a small amount of salt (0.02 mol of salt per mol of ethylene oxide monomers) causes a fundamental change in the thermodynamic properties: this mixture exhibits a disorder-to-order transition upon heating. In other words, salt stabilizes the disordered phase at low temperatures. All previous studies on the thermodynamics of block copolymer salt mixtures have concluded that the addition of salt stabilizes the ordered phase at low temperatures. However, disorder-to-order transitions upon heating have been reported in a number of neat diblock copolymer systems including polystyrene with certain poly(alkyl methacrylate)s[63,64], poly(ethylene oxide) with poly(2-vinylpyridine)[65], and poly(n-hexyl norbornene)-*b*-poly(cyclohexyl norbornene)[66]. Further addition of salt to PEO-POSS results in formation of ordered lamellar and hexagonally packed cylindrical phases. We also report on the electrical and mechanical properties of these PEO-POSS/LiTFSI mixtures. We show that both the ionic conductivity and shear modulus of our POSS-containing block copolymer electrolytes are significantly larger than those of conventional organic block copolymer electrolytes.

2.2. Experimental Methods

2.2.1. Synthesis of PEO-POSS block copolymer.

Materials**.** PEO-acrylate ($M_w = 5$ kg mol^{-1}), anhydrous ethanol, anhydrous *o*-xylene, diethyl ether and tetrahydrofuran (THF) were purchased from Sigma-Aldrich, acryloisobutyl polyhedral oligomeric silsesquioxane (POSS) was purchased from Hybrid Plastic, BlocBuilder MA was kindly provided by Arkema. All previous chemicals were used as received. Lithium bis(trifluoromethanesulfone)imide, $Li[N(SO_2CF_3)_2]$ (LiTFSI), was purchased from Novolyte and was dried at 120 °C for 48 hours before use.

Synthesis. PEO-POSS block copolymer was synthesized by nitroxide-mediated radical polymerization (NMP). First, PEO-acrylate was reacted with BlocBuilder MA in anhydrous ethanol at 100 ^{o}C under argon for 4h. PEO-based macroalkoxyamine was collected by precipitation in cold diethylether. Then, the acryloisobutyl POSS monomer was polymerized using the PEO-based macroalkoxyamine as initiator in anhydrous xylene at 115 °C for 24 h. The product was isolated by precipitation in cold diethyl ether and centrifuged at 6500 rpm for 10 min. This step was repeated three times to obtain a white solid powder. Molecular weight was determined using H-NMR of 1.9 kg mol^{-1} of POSS.

Electrolyte Preparation**.** Electrolytes were prepared by mixing each polymer with LiTFSI. Due to the hygroscopic nature of LiTFSI, all sample preparation was carried out in an argon glovebox (MBraun) where H_2O and O_2 levels were maintained below 0.6 ppm and 1 ppm respectively. PEO-POSS polymer was dried at 90 °C under vacuum in the glovebox antechamber for 48 h, and then transferred into the glovebox. Dry polymer and LiTFSI salt were dissolved into anhydrous THF and the solutions were mixed at 60 °C for a minimum of 12 h. Once the solutes were fully dissolved, the caps were removed from the vials allowing THF to evaporate and leave behind a homogeneous polymer/salt mixture. After drying on a hotplate at 90 °C for 48 h, the electrolytes were transferred to the glovebox antechamber and dried under vacuum for 48 h at 90 °C to remove all of the THF. The dry electrolytes color ranged from clear to pale yellow and had a waxy consistency at room temperature. Salt concentration is quantified by ratio of lithium to ethylene oxide moieties, $r = [\mathrm{Li}]\,[\mathrm{EO}]^{-1}$.

2.2.2. Shear Rheology.

The viscoelastic properties were studied using a strain-controlled Rheometric Scientific ARES (Advanced Rheometric Expansion System) rheometer. The polymer sample without salt was prepared by pressing at 90 °C for 72 h to remove air bubbles in an Argon glovebox in a 7.9 mm diameter mold each made of fabric-reinforced silicone rubber sheet with an adhesive back (McMaster-Carr). The rheometer was equipped with 8 mm diameter parallel plates, and a gap of 0.5 mm was utilized. The existence and extent of the linear viscoelastic regime were determined using a strain sweep test at 1 rad s^{-1} to determine the strains at which the storage (G') and loss (G'') moduli were constant. A strain in this linear regime was chosen such that the torque in the subsequent dynamic frequency sweep test was greater than 0.2 g of force. The thermal expansion of the plattens at each temperature was taken into account using a thermal expansion factor of 2.2 μm °C^{-1}.The experimental protocol consisted of heating the fixtures with the sample to 90 °C, holding isothermally for 30 min to equilibrate, then setting the gap separation and starting measurements.

2.2.3. Impedance Spectroscopy.

Stainless steel symmetric cells were prepared for ionic conductivity measurements of electrolytes using ac impedance spectroscopy. Electrolytes were heated to 90 °C and pressed into a 3.175 mm diameter hole within a 254 μm thick silicone spacer. Two 200 μm-thick stainless-steel electrodes were pressed on either side of the electrolyte-filled spacer. The silicone forms a good seal with stainless steel which prevents the polymers from leaking out of the cell. The thickness of each electrolyte was determined by measuring the thickness of the cell using a micrometer and subtracting the thickness of the electrodes. Aluminum tabs were secured to the electrodes using Kapton tape. The entire cell was hermetically sealed within Showa-Denko pouch material leaving only the tab ends exposed. This allows for electrochemical measurements to take place outside of the glovebox while an air- and water-free environment is maintained for the electrolyte. Once removed from the glovebox, each cell was placed in a custom-built heating stage to determine conductivity in the range of 30 °C to 130 °C. Complex impedance measurements were acquired using a Biologic VMP3 potentiostat for a frequency range of 1 Hz to 1 MHz at an amplitude of 50 mV. Measurements were repeated three times and the standard deviation was used to estimate error bars.

2.2.4. Transmission Electron Microscopy and Electron Tomography**.**

PEO-POSS electrolytes were hermetically sealed within Showa-Denko pouch material in an argon glovebox to remain air and moisture free and heated to the desired temperature for 30 minutes in an oil bath. Samples were then quenched in liquid nitrogen for 5 minutes before allowing to return to room temperature. The electrolytes were sectioned at -120 °C using cryo-microtome (Leica Ultracut 6) to obtained an ultrathin film (~100 nm). The ultrathin film was transferred to a copper grid with lacey carbon supporting film and stored in an argon glovebox immediately after cryo microtoming to minimize the effect of humidity. Poly(ethylene oxide)-rich domains were stained to increase contrast and stability under the electron beam by exposing the ultrathin film to ruthenium tetroxide vapor for 10 minutes at room temperature. HAADF-STEM micrographs were collected using FEI Tecnai F20 at 200 kV with camera length 140 cm. 5 nm gold colloid nanoparticles were deposited on the backside of the grid as fiducial markers. Single-axis tomography was performed using JEOL 3100FFC cryo transmission electron microscope at 300 kV. The tilt series were collected at cryogenic temperature in order to minimize irradiation damage. The tilting angle ranged from -62 to 62 degrees in 1.5-degree increments. Tomograms were reconstructed and filtered (nonlinear anisotropic diffusion filter) in IMOD. Tomogram of a small area was visualized in 3D in Chimera by adjusting the threshold[1-4].

2.2.5. NMR.

The composition of the organic-inorganic copolymers was determined using ^{1}H NMR ($CDCl_3$, Bruker AV400) measurements by integrating the characteristic peaks of the ethylene protons of PEO block at 3.7 ppm versus protons at 0.63-0.65 of the POSS block in Figure 2.1. ^{29}Si NMR ($CDCl_3$, Bruker AV400) was performed, revealing clear signals for Si at 67.2-67.5 ppm in Figure 2.2.

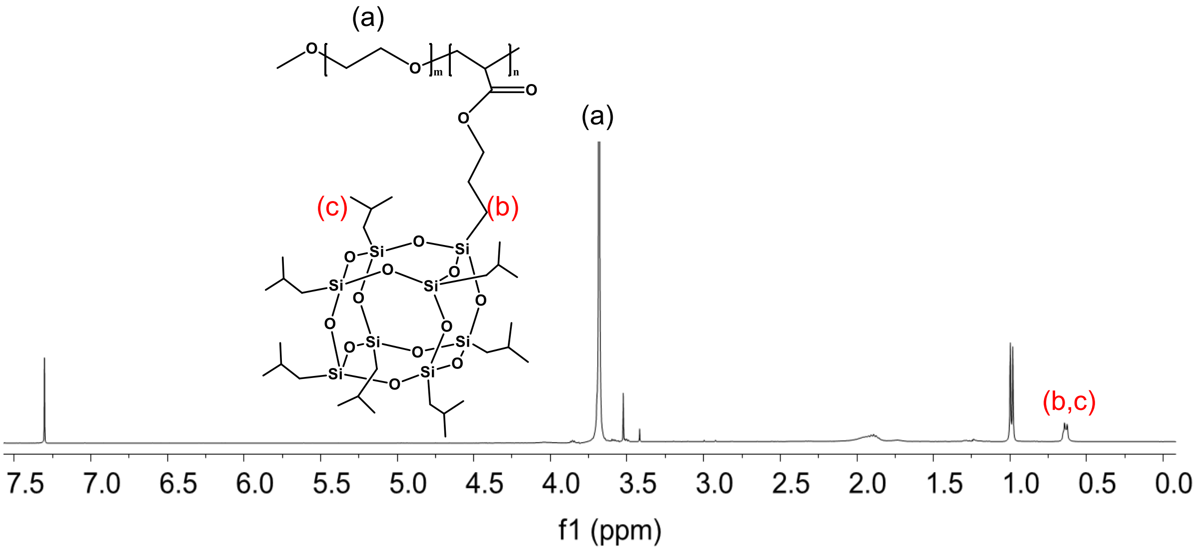

Figure 2.1 ^{1}H-NMR of PEO-POSS. A sharp peak due to PEO is visible at chemical shift, δ, 3.70 ppm and POSS at 0.63-0.65 ppm. The corresponding hydrogens are indicated on the PEO-POSS chemical structure labeled (a) from the PEO chain, (b) from the acrylate chain, and (c) from the isobutyl groups on the POSS molecule.

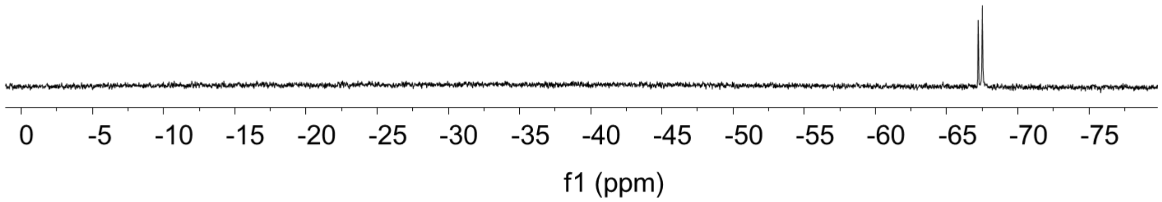

Figure 2.2 ^{29}Si-NMR of PEO-POSS indicating two close peaks at chemical shift, δ, at 67.2 and 67.5 ppm

2.2.6. Thermogravametric Analysis.

The polymer thermal degradation temperature was determined via thermogravametric analysis (TGA) using TA Instruments Q5500 TGA-MS at the Molecular Foundry, LBNL. Data are shown in Figure 2.3.

2.2.7. Gel Permeation Chromatography.

PEO-POSS was characterized by a Malvern Viscotek TDAmax system gel permeation chromatography (GPC) system with a mobile phase of THF using an injection volume of 100 µL and polymer concentration 2.0 g L^{-1}. GPC traces of PEO-POSS in relation to PEO-

Acrylate confirm the polymerization of the POSS block, shown in Figure 2.4 A small shoulder in the PEO-POSS is due to growing chains terminate by coupling. Due to the complex molecular structure of the PEO-POSS copolymer and potential interactions between the ionic group and the columns, we only use the GPC data to confirm addition of POSS segments onto the PEO chain. Quantification of the relations between elution volume and molecular weight is not possible.

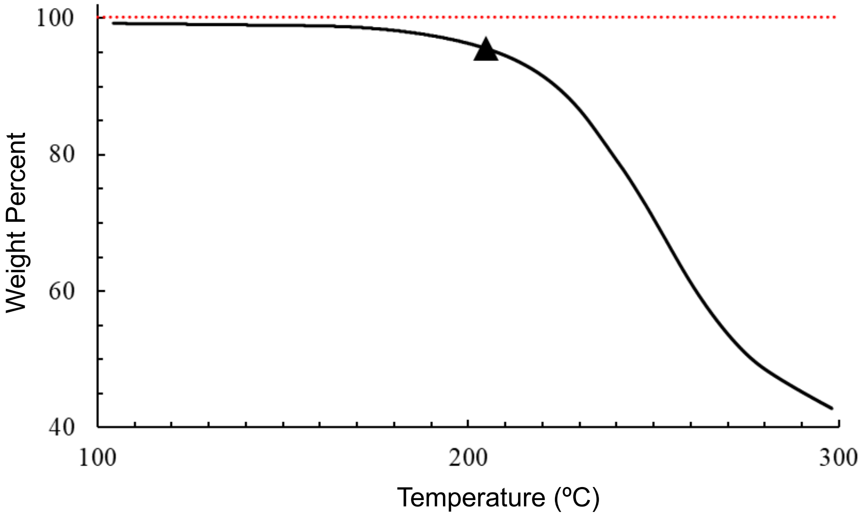

Figure 2.3. TGA data for PEO-POSS plotting weight percent versus temperature. 100% is marked in the y-axis with a dashed line. The temperature at 5% decrease in weight, T_{95}, is 207 °C, noted with a triangle.

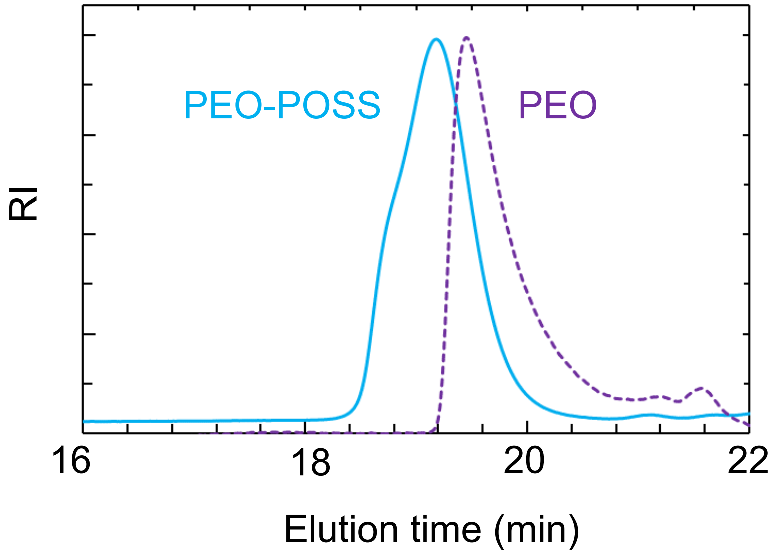

Figure 2.4. Gel Permeation Chromatography data of PEO-POSS and PEO-Acrylate.

2.2.8. Small Angle X-ray Scattering.

The morphologies of the electrolytes were determined by small-angle x-ray scattering (SAXS). Samples were prepared by pressing the polymer at 90 °C into 1 mm thick rubber spacers with a 1/8 in. inner-diameter and sealed with Kapton windows in custom-designed airtight holders. The samples were annealed at 110 °C under vacuum for at least 24 h. Measurements were performed at beamline 7.3.3. at the Advanced Light Source (ALS) at Lawrence Berkeley National Laboratory and beamline 1–5 at the Stanford Synchrotron Radiation Lightsource (SSRL) at SLAC National Accelerator Laboratory. Samples were mounted in a custom-built heating stage and held at each temperature for at least 30 min before taking measurements. Silver behenate was used to determine the beam center and sample-to-detector distance. The scattered intensity was corrected for beam transmission. Two-dimensional scattering patterns were integrated azimuthally using the Nika program for IGOR Pro[1] to produce one-dimensional scattering profiles and are reported as scattering intensity, I, as a function of the magnitude of the scattering vector, q; $q = 4\pi sin\theta/2\lambda$ where θ is the scattering angle, and λ is the wavelength of the x-rays equal to 1.2398 Å. The samples were heated from room temperature to the highest temperature of 132 °C in 20 °C increments and cooled in 5 °C increments.

2.2.9. Density Measurements.

Samples were heated to 120 °C, weighed, and filled into pre-weighed aluminum pans with a known volume of 0.04 mL. Pans were hermetically sealed in an argon glovebox and excess polymer was carefully cleaned from the pan. The final weight was recorded. Density of the PEO-POSS diblock copolymer was determined by dividing the mass by the known volume of sample pans. Measurements were repeated three times to obtain a standard deviation. Density obtained was 1.12 ± 0.03 g mL^{-1}.

2.3. Results and Discussion

Small angle X-ray scattering (SAXS) profiles of neat PEO-POSS at selected temperatures between 85 °C and 132 °C (both blocks are amorphous in this temperature range) are shown in Figure 2.5a where scattering intensity, I, is plotted as a function of the magnitude of the scattering vector, q. At 85 °C we obtain a primary scattering peak at $q = q^* = 0.32$ nm^{-1} and a second order scattering peak at $2q^*$. This is a standard signature of a lamellar phase. The center-to-center distance between adjacent PEO lamellae, d, given by $d = 2\pi/q^*$, is 19.6 nm. This morphology persists until 122 °C. At 127 °C, the intensity of the primary scattering peak diminishes significantly and the second order peak disappears. This SAXS profile indicates the presence of disordered concentration fluctuations. It is evident that neat PEO-POSS exhibits an order-to-disorder transition upon heating at 125 °C. This behavior, that is qualitatively similar to that of most organic block copolymers, suggests that PEO and POSS chains exhibit repulsive interactions[67–69]. At low temperatures, these interactions dominate, leading to an ordered phase. At high temperatures entropic effects dominate, leading to mixing of PEO and POSS segments. The estimated Flory Huggins interaction parameter, based on a reference volume of 0.1 nm^3, at 125 °C is 0.18 using a diblock copolymer phase diagram.[70]

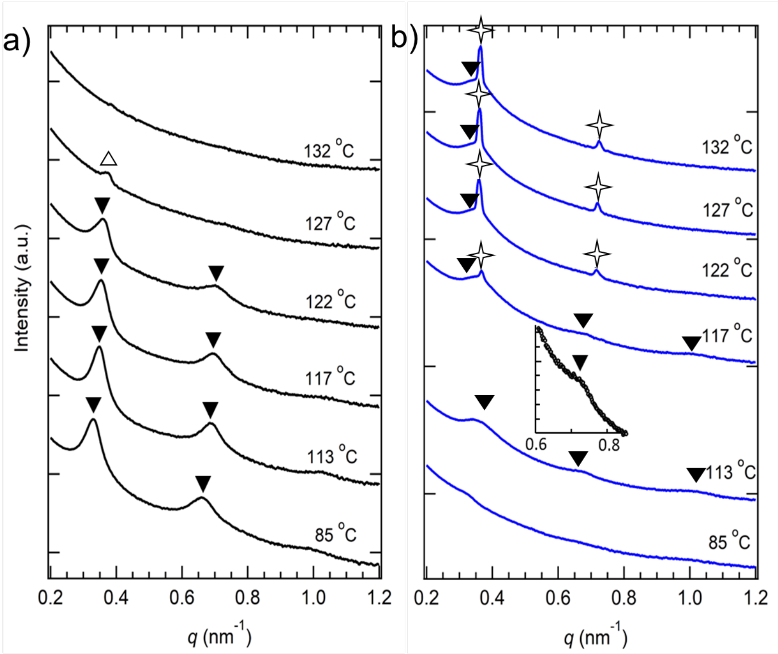

Figure 2.5. Scattering intensity of PEO-POSS at selected temperatures shown on the right, plotted as a function of the magnitude of the scattering vector, q (a) neat polymer and (b) PEO-POSS/LiTFSI mixture at r = 0.02. Profiles are shifted vertically. ▼, ✧, and △ indicate peaks characteristic of lamellae ($q = q^*$, $2q^*$, $3q^*$), coexisting lamellae, and disorder ($q = q^*$).

The SAXS profiles obtained from a PEO-POSS/LiTFSI mixture with r = 0.02 are shown in Figure 2.5b. At 85 °C, I is a monotonically decaying function of q, qualitatively similar to the 132 °C data obtained from neat PEO-POSS. We therefore conclude that the r = 0.02 sample is disordered at this temperature. Increasing the temperature to 113 °C results in broad SAXS peaks at $q = q^* = 0.33\ \mathrm{nm}^{-1}$ and at $q = 2q^*$; see inset in Figure 2.7b. The emergence of the higher order peak is taken to be a signature of the disorder-to-order transition. (There is a hint of a broad peak at $q = 3q^*$ in the 113 °C data in Figure 2.5b). Disorder-to-order transitions upon heating have been reported in several neat diblock copolymer systems[63–66,71–73]. Increasing the temperature further to 117 °C results in the appearance of sharp peaks at $q = q^* = 0.35\ \mathrm{nm}^{-1}$ and at $2q^*$ superposed on a broad scattering peak. The SAXS profile at 122 °C and above are characteristic of a well-ordered lamellar phase coexisting with a weakly ordered lamellar phase. The scattering peaks obtained from the well-ordered lamellar phase at r = 0.02 are significantly sharper than those seen in the neat copolymer (compare the 85 °C scattering profile in Figure 2.7b with 132 °C scattering profile in Figure 2.7c). This observation indicates that the high temperature ordered phase obtained in the salt-containing PEO-POSS sample exhibits better long-range order than the low temperature ordered phase in neat PEO-POSS. Whether this is due to the presence of salt or the annealing of defects at higher temperature is unclear at this juncture. We posit the presence of two coexisting ordered phases are phases with different salt concentrations[74].

It is well known that if salt interacts exclusively with the PEO block, one observes stabilization of the ordered phase[75–81]. In contrast, in salt-containing PEO-POSS at temperatures below 97 °C the addition of salt stabilizes the disordered phase. The data in Figure 2.7 suggests that the salt molecules interact with both PEO and POSS segments. While further work is needed to identify the nature of these interactions, they are strong enough to cause mixing between chains that are immiscible without salt. At sufficiently high temperatures, entropic contributions dominate, the relative importance of specific interactions diminishes, and PEO and POSS segments form separate domains

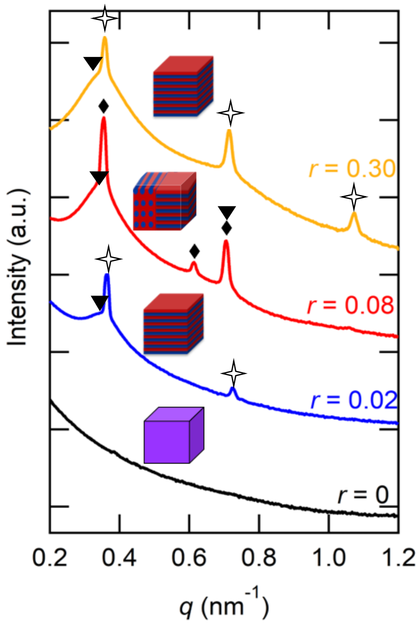

Figure 2.6. Scattering intensity of PEO-POSS/LiTFSI mixtures at 132 °C is plotted as a function of the magnitude of the scattering vector, *q*. The salt concentration of each profile is indicated on the right. Profiles are shifted vertically. ▼, ✧, ∆ and ◊ indicate peaks characteristic of lamellae (*q* = *q**, 2*q**, 3*q*), coexisting lamellae, disorder (*q* = *q**), and hexagonally packed cylinders (*q* = *q**, √3*q**, 2*q**).

The effect of added salt on the morphology of PEO-POSS electrolytes is shown in Figure 2.6 for a range of salt concentrations at 132 °C. The neat sample is disordered at this temperature, while all salt containing samples are ordered. At low salt concentration, $r = 0.02$, a coexisting well-ordered lamellar phase with a weakly ordered lamellar phase is obtained. Increasing the salt concentration to $r = 0.08$ results in the emergence of an additional scattering peak at $q = \sqrt{3}q^*$ that is superimposed on the scattering profile of the lamellar phase. This peak is a signature of a hexagonally packed cylinders morphology. Increasing salt concentration further to $r = 0.30$ results again in two coexisting lamellar phases. The dependence of domain spacing on salt concentration and temperature is shown in the Supporting Information at the end of this chapter.

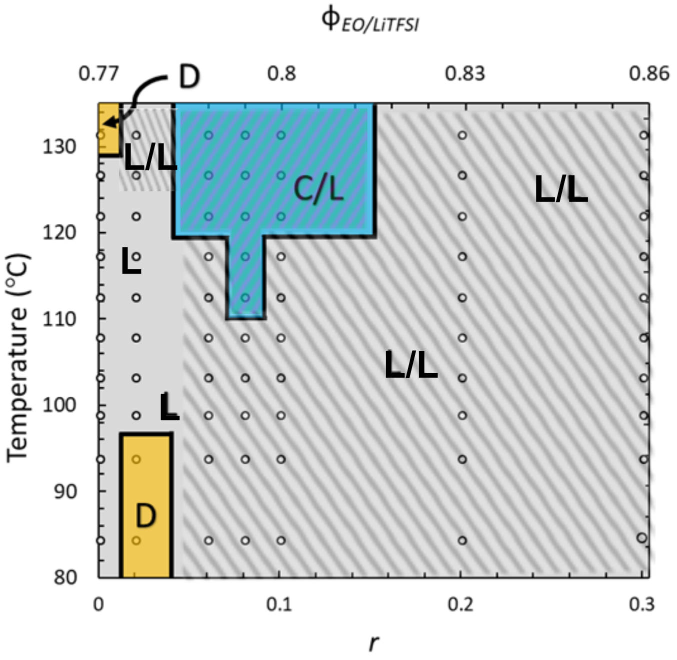

Figure 2.7. Morphology of phases on a temperature versus salt concentration (r) plot: lamellae(L), coexisting lamellae (L/L), disorder (D), and hexagonally packed cylinders which always coexist with lamellae (C/L). The top axis is volume fraction of the EO/LiTFSI-rich phase.

Figure 2.7 summarizes the results of the SAXS experiments, where the morphologies of PEO-POSS/LiTFSI mixtures are shown as a function of temperature and salt concentration. The coexisting lamellar/lamellar (L/L) phase dominates the phase diagram which contains isolated pockets of disordered (D) and coexisting cylinders/lamellae (C/L). This is surprising given ϕ_{EO} is 0.77. Determining the distribution of salt in two coexisting microphases is beyond the scope of this study. Using the assumption that is standard in the field of block copolymer electrolytes that LiTFSI resides exclusively in the PEO domains[30, 59,78], the estimated volume fraction of the PEO-rich phase increases with salt addition to $\phi_{EO} = 0.86$ at $r = 0.30$. This estimated volume fraction is shown as the secondary (top) x-axis in Figure 3. The geometry of ordered phases in conventional block copolymers depends mainly on the volume fraction of one of the blocks[82,83]. Increasing the volume fraction of the major component is expected to stabilize either cylinders or spheres, not lamellae[69,84]. If this were true in PEO-POSS, cylinders would emerge at high salt concentration. Clearly, this is not the case. The sample with $\phi_{EO} = 0.86$ exhibits lamellar morphologies over the entire accessible temperature window. Cylinders are only seen at high temperatures in a limited window ($0.06 \leq r \leq 0.1$). We posit that the specific interactions between salt, PEO, and POSS that stabilize the disordered phase in the dilute electrolyte are also responsible for the unexpected stabilization of the lamellar phases. At high temperatures, the importance of these interactions diminishes, leading to the formation of the expected cylinder phase. We note that the Gibbs phase rule requires coexistence at all phase boundaries in Figure 2.7. This suggests the presence of a pure cylinder phase and pure lamellar phase at temperatures above 132 °C

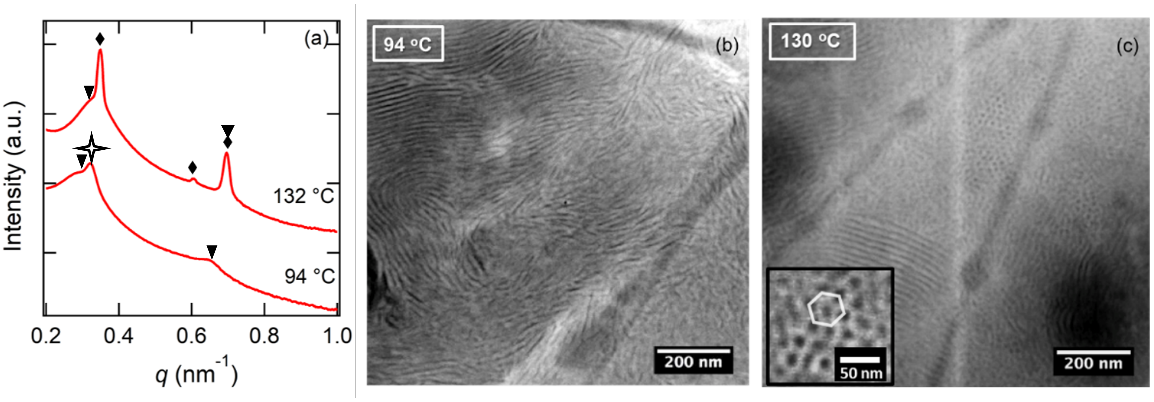

Figure 2.8. SAXS and TEM. (a) SAXS scattering profiles are taken at 94 °C, with scattering peaks indicative of a coexisting lamellar morphology indicated by triangles and star markers, and 132 °C with scattering peaks denoted by diamond and triangle markers indicating coexisting cylinders and lamellae, respectively. (b) and (c) HAADF-STEM micrographs of RuO_4-stained PEO-POSS electrolytes with $r = 0.08$. The bright phase represents the RuO_4-stained PEO-rich phase. Separate samples were annealed at selected temperatures and quenched using liquid nitrogen. (b) Sample annealed at 94 °C showing lamellar morphology. (c) Sample annealed at 130 °C showing coexisting hexagonally packed cylinders and lamellae. SAXS and TEM data are consistent with each other.

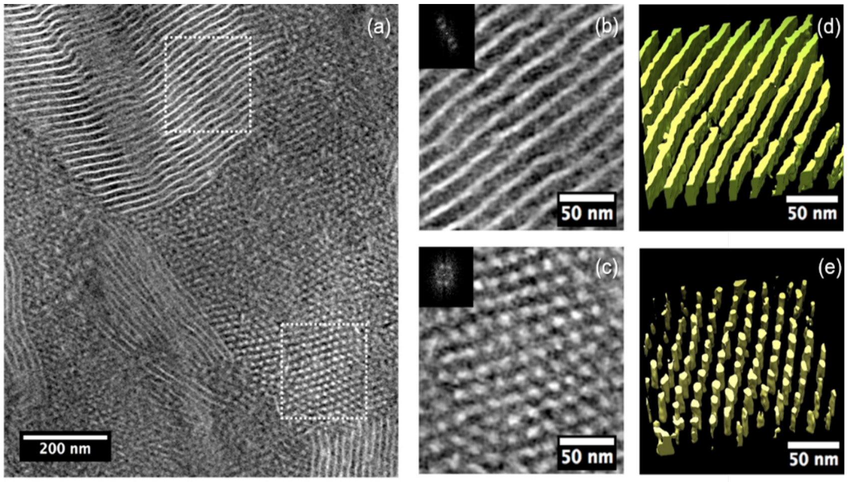

Figure 2.9. Electron Tomography of PEO-POSS $r = 0.08$ showing coexisting lamellae and cylinders. Sample was quenched in liquid nitrogen after annealing at 130 °C and the scans were taken at room temperature. (a) Bright field tomogram where the dark phase represents the stained EO-rich microphase. (b) and (c) Boxed regions shown on an expanded scale. Insets show Fourier transforms of the images. (d) 3-D tomogram of (b) showing a lamellar phase. (e) 3-D tomogram of (c) showing hexagonally packed cylinders.

Electron microscopy was used to elucidate the nature of the ordered phases reported in Figure 2.8. Two samples of the $r = 0.08$ electrolyte were annealed at 94 °C and 130 °C and quenched in liquid nitrogen to “freeze” the morphology at these temperatures. The resulting micrographs, obtained by high-angle annular dark-field scanning transmission electron microscopy (HAADF-STEM) are shown in Figure 2.10b and Figure 2.10c where the bright phase represents the RuO_4 stained PEO-rich microphases. The micrograph obtained from the 94 °C sample shows alternating dark and bright stripes representing the lamellar phase. The micrograph obtained from the 130 °C sample shows both dark spots arranged on a hexagonal lattice (Figure 4c inset), confirming the presence of POSS-rich cylinders in a PEO-rich matrix, and alternating POSS-rich and PEO-rich stripes.

To confirm that the stripes seen in Figure 2.8c correspond to a lamellar phase as opposed to cylinders lying in the sample plane, electron tomography of the $r = 0.08$ electrolyte annealed at 130 °C was utilized, and the results are shown in Figure 2.9. Figure 2.9a shows a slice of the tomogram where POSS is the bright phase and PEO is the dark phase. Bright spots arranged in a hexagonal lattice imply POSS rich-cylinders and alternating bright and dark stripes indicate lamellae. Figures 2.9b and 2.9c are magnifications of the outlined boxes in Figure 2.8a that depict the lamellar and cylindrical morphology, respectively. Fourier transforms of the real-space images are also provided to confirm these lattice arrangements. Figure 2.9d is a 3D representation of the POSS-rich phase of the tomogram shown in Figure 2.9b. It indicates the presence of lamellae. Similarly, Figure 2.9e, which is a 3D representation of Figure 2.9c, shows the presence of

POSS-rich cylinders. Thus, the coexistence of lamellae and cylinders is confirmed by both SAXS and electron tomography.

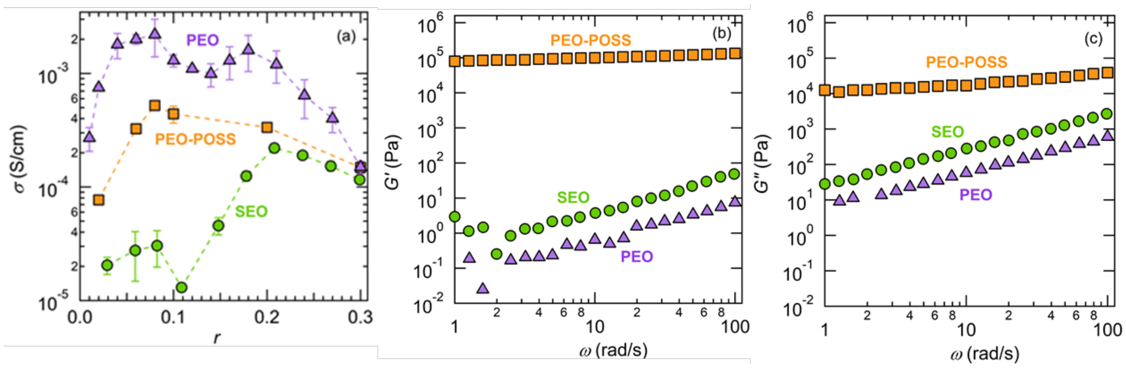

Figure 2.10. Dependence of ionic conductivity on salt concentration and rheological properties of neat polymers at 90 °C. (a) Ionic conductivity, σ, is plotted against salt concentration, *r*, for the block copolymers PEO-POSS, SEO[44], and homopolymer PEO[45]. (b) and (c) Storage and loss shear moduli, *G′* and *G″*, plotted against frequency, *ω,* for PEO-POSS, SEO[46], and homopolymer PEO[46].

The transport of lithium ions in polymers is facilitated by the segmental motion which is rapid in soft polymers such as amorphous PEO[85]. The goal of creating block copolymer electrolytes is to increase the modulus of the electrolyte while minimizing the decrease in ionic conductivity due to the presence of non-conducting domains. The ionic conductivity of PEO-POSS electrolytes is plotted as a function of salt concentration at 90 °C in Figure 2.10a. The electrolytes have a lamellar morphology at all values of *r* except *r* = 0.02, where it forms a disordered phase. Also shown in Figure 2.10a is the conductivity of homopolymer PEO electrolyte with a molecular weight of 5 kg mol^{-1} and that of a conventional polystyrene-*b*-poly(ethylene oxide) (SEO) electrolyte with molecular weights of 5 kg mol^{-1} of both blocks ($\phi_{EO} = 0.52$)[75]. We chose this SEO copolymer because it has the same molecular weight for the conducting block and exhibits a lamellar morphology[86]. Both SEO and PEO-POSS electrolytes exhibit lower conductivities than PEO electrolyte, as expected. However, in the dilute limit, the conductivity of PEO-POSS electrolytes are much higher than that of SEO, by factors ranging from 2 to 10.

The rheological properties of PEO-POSS, PEO (20 kg mol^{-1}), and SEO are shown in Figure 2.10b and 2.10c at 90 °C. (The modulus of PEO (5 kg mol^{-1}) was below the dynamic range of our rheological instrument.) We only present data obtained from the neat polymers due to the hygroscopic nature of the salt-containing electrolytes. The low frequency storage modulus (*G′*) of SEO is about a factor of 10 higher than PEO, while the loss modulus (*G*") is about a factor of 5 higher. Both *G′* and *G″* of SEO and PEO decrease rapidly with decreasing frequency. In contrast, *G′* of PEO-POSS is nearly independent of frequency while *G″* decreases slightly in the frequency range studied. The *G′* of PEO-POSS at low frequency ($\omega = 1$ rad/s) is a factor of 10^5 higher than SEO, while G'' is over a factor of 10^2 higher than SEO.

2.4 Conclusion.

In summary, PEO-POSS represents a new platform for creating self-assembled hybrid electrolytes for lithium batteries. In the absence of salt, PEO-POSS presents a classical order-to-disorder transition upon heating. The addition of salt at low concentration results in a disorder-to-order transition upon heating. Further increase in salt concentration results in the stabilization of ordered phases. In conventional block copolymers, spherical or cylindrical morphologies are expected when the volume fraction of the major phase is between 0.77 and 0.86. In PEO-POSS, we primarily obtain lamellar phases. The cylindrical morphology is only stable at high temperatures and intermediate salt concentrations. The ionic conductivity of lamellar PEO-POSS electrolytes is higher than that of SEO at all salt concentrations at 90 °C; at $r = 0.10$ the conductivity of PEO-POSS is 50 times higher than that of SEO. The low frequency G' of PEO-POSS is five orders of magnitude higher than that of SEO. Further work on optimizing the properties of organic-inorganic hybrid block copolymers for use in all-solid lithium batteries seems warranted.

LIST OF SYMBOLS

C	hexagonally packed cylinders phase
d	domain spacing (nm)
D	disordered phase
f_i	volume fraction of the species i
G'	storage Modulus (Pa)
$\underline{G}''$	loss Modulus (Pa)
I	scattering intensity
L	lamellar phase
M_{PEO}	molecular weight of the poly(ethylene oxide) block (kg mol^{-1})
M_{PPOSS}	molecular weight of the polyhedral oligomeric silsesquioxane block (kg mol^{-1})
M_i	molecular weight of species i (g mol^{-1})
N	degree of polymerization
q	scattering vector (nm^{-1})
$q*$	scattering vector at the primary scattering peak (nm^{-1})

r	salt concentration ([Li] [EO] $^{-1}$)
T	Temperature (°C)

GREEK

v_i	molar volume of species i (cm^3 mol^{-1})
v_{ref}	reference volume of species i (cm^3 mol^{-1})
$\phi_{EO/LiTFSI}$	volume fraction of PEO/LiTFSI microphase
ρ_i	density of species i (g cm^{-1})
σ	ionic conductivity (S cm^{-1})
θ	X-ray scattering angle
λ	X-ray wavelength
χ	Flory-Huggins interaction parameter

2.5. Supporting Information

2.5.1. Temperature Dependent Data Ionic Conductivity.

The ionic conductivity is measured as described in the "Experimental Methods" section. The data for electrolytes with salt concentration [Li]/[EO] = r ranging from 0.02 to 0.30 is shown. Error bars indicate the standard deviation from three measurements. The sharp drop-off in the conductivity of electrolytes with salt concentration of r = 0.02 and 0.06 and the low room temperature conductivity is due to crystallization of the PEO block.

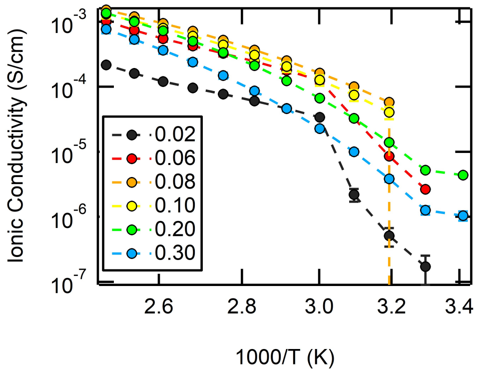

Figure 2.11. Ionic conductivity of electrolytes versus inverse temperature. Salt concentration is indicated as r = [Li]/[EO].

2.5.2 Rheological Data.

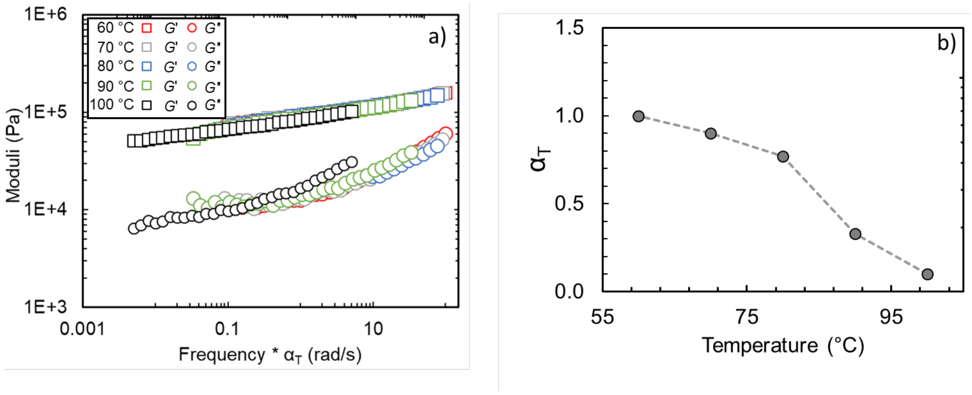

Figure 2.12. a) Master curves of storage and loss moduli (*G*') and (*G*") of the PEO-POSS diblock copolymer at a reference temperature 60 ˚C. b) Shift factors as a function of temperature used to shift data a).

2.5.3. Data Analysis Methods.

Volume Fraction. The volume fraction of the EO/LiTFSI-rich phase in the diblock copolymer was computed using the following equation.

$$\phi_{EO/LiTFSI}(r) = \frac{v_{EO} + r v_{LiTFSI}}{v_{EO} + r v_{LiTFSI} + \frac{M_{PPOSS} M_{EO}}{M_{POSS} M_{PEO}} v_{POSS}}$$

Where,

v_{EO} = molar volumes of ethylene oxide monomer units
v_{POSS} = molar volumes of POSS monomer units
v_{LiTFSI} = molar volumes of LiTFSI
r = [Li]/[EO]
M_{PPOSS} = Molar mass of polymerized POSS = 1.9 kg mol^{-1}
M_{POSS} = Molar mass of POSS monomer = 929.61 g mol^{-1}
M_{EO} = Molar mass of EO monomer = 44.05 g mol^{-1}
M_{PEO} = Molar mass of PEO = 5.0 kg mol^{-1}
Molar volumes are calculated using the following equation:

$$v_i = M_i/\rho_i$$

Where M_i and ρ_i are the molar masses of unit *i* and density of unit *i* respectively.

The temperature was fixed at 120 °C.
The temperature dependence of PEO density is given[39]

$$\rho_{PEO} = 1.139 - 7.31 \times 10^{-4} \times T(120\ °C) = 1.05\ g\ mL^{-1}$$

The density of the diblock copolymer, $\rho_{PEOPOSS}$ is 1.12 g mL^{-1}. The density of the POSS-rich phase was determined under the assumption that the volumes of the EO-rich and POSS-rich phases are additive. ρ_{POSS} was determined to be 1.30 g mL^{-1} using the following equation:

$$\rho_{POSS} = [\rho_{PEOPOSS} - \frac{M_{PEO}}{M_{PEO}+M_{PPOSS}}\rho_{PEO}]\frac{M_{PEO}+M_{PPOSS}}{M_{PPOSS}}$$

Flory Huggins Interaction Parameter. $\phi_{EO/LiTFSI}$ was determined to be 0.77 for the neat polymer. *N* was found to be 103, calculated using the method described in ref [22] based on a reference volume of 0.1 nm^3. The order-to-disorder transition (ODT) for a neat diblock copolymer based on self-consistent field theory occurs at χN = 18.5 (see Figure S3). Therefore, at 97 °C where we observe an ODT, χ = 0.18.

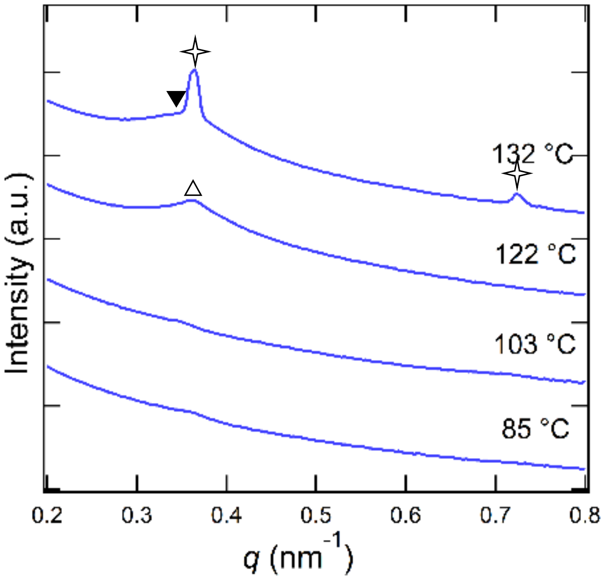

Figure 2.13. Small angle x-ray scattering profile of PEO-POSS *r* = 0.02 upon heating from 85 °C to 132 °C indicating the same phase transition as cooling. Temperatures are given on the right. ▼, ✧, and △ indicate peaks characteristic of lamellae (*q* = *q**, *2q*, 3q**), coexisting lamellae, and disorder (*q* = *q**)

2.5.4 Domain Spacing.

The domain spacing ($d = 2\pi/q^*$) of PEO-POSS/LiTFSI mixtures is nearly independent of salt concentration. In SEO/LiTFSI systems, domain spacing increases by about 17% over the same concentration range[86]. We attribute this to differences in the thermodynamic interactions with the salt in the two systems.

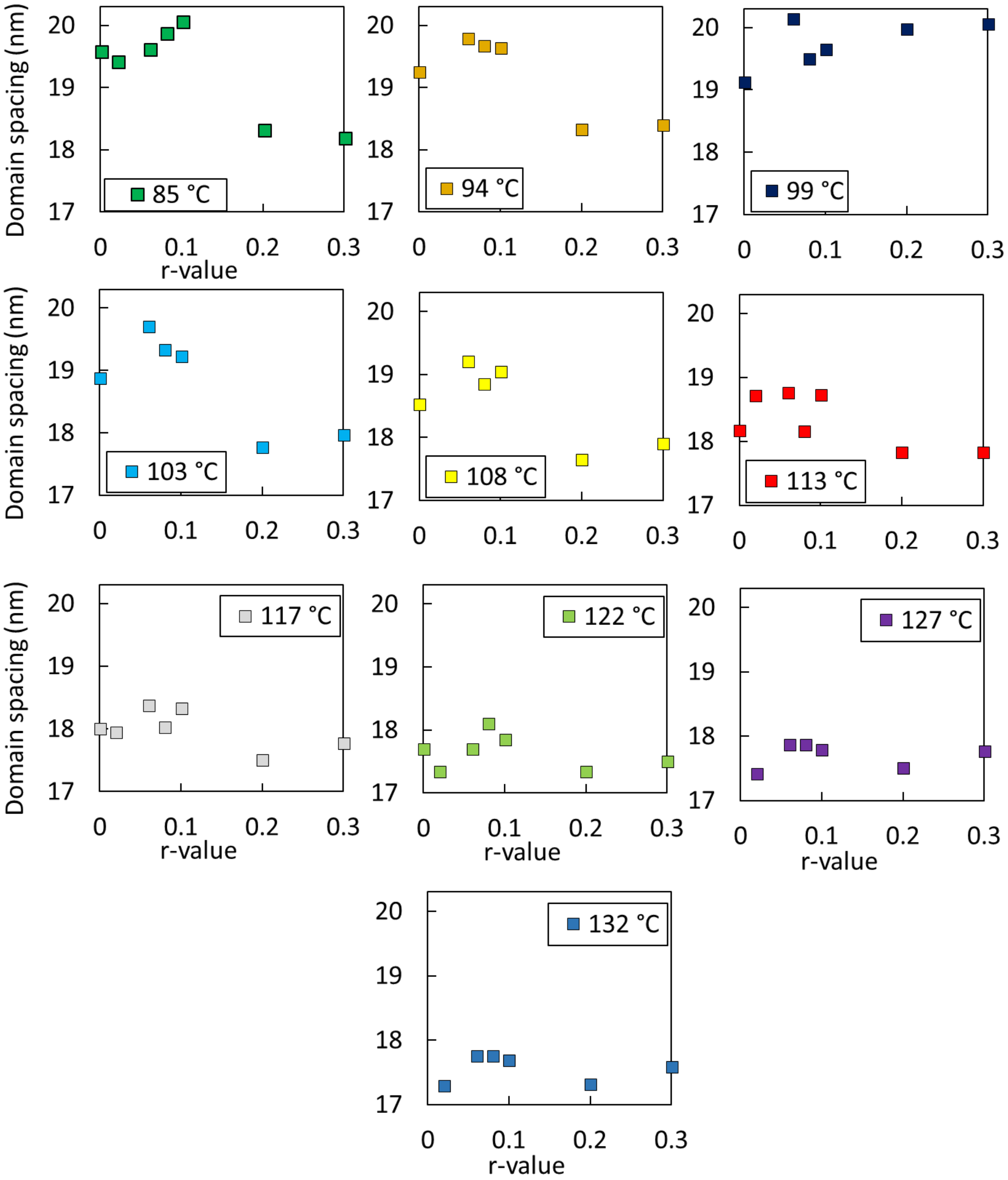

Figure 2.12. The domain spacing versus *r* at 85 °C to 132 °C

3. Structure and Thermodynamics of Hybrid Organic-Inorganic Diblock Copolymers with Salt[†]

ABSTRACT

We examine the phase behavior of a hybrid organic-inorganic diblock copolymer/salt mixtures. The experimental system comprises poly(ethylene oxide)-*block*-polyhedral oligomeric silsesquioxane (PEO-POSS) mixed with a lithium bis(trifluoromethanesulfonyl) imide (LiTFSI) salt. While the diblock copolymers without salt exhibit classical order-to-disorder transition behavior with increasing temperature, the PEO-POSS/salt mixtures exhibit disorder-to-order transitions with increasing temperature. Analysis of small angle X-ray scattering data from the disordered state using Leibler's Random Phase Approximation enables the determination of an effective Flory-Huggins interaction parameter, χ_{eff}, for the electrolytes. Unlike conventional systems, χ_{eff} increases with increasing temperature. A simple expression is proposed to describe the dependence of χ_{eff} on temperature and salt concentration. This enables calculation of the segregation strength, $\chi_{eff}N$, for both ordered and disordered electrolytes. The composition of the electrolytes is quantified by $f_{EO/LiTFSI}$, the volume fraction of the salt-containing poly(ethylene oxide)-rich phase. The morphology of electrolytes is presented on a $\chi_{eff}N$ versus $f_{EO/LiTFSI}$ phase diagram. Over the values of $f_{EO/LiTFSI}$ studied (0.61-0.91) the following ordered phases were found: lamellae, two coexisting lamellae phases, and coexisting lamellae/hexagonally packed cylinders.

3.1. Introduction

Solid polymer electrolytes are more electrochemically and thermally stable in comparison to conventional liquid electrolytes for lithium batteries.[57] Linear block copolymers, wherein two chemically distinct polymer chains are chemically bonded together, can provide separate ion-conduction channels as well as mechanically rigid, non-conducting channels. The classic balance between entropy and enthalpy in addition to covalent bonds between the two blocks causes these materials to self-assemble into nanostructured morphologies with length scales on the order of tens of nanometers. The thermodynamics of all organic electrolytes with salt has been extensively studied in experimental[2-12] and theoretical systems.[13-15] Though there have been studies conducted on the electrochemical properties,[87–91] mechanical properties,[21,22] and ordered phases of hybrid inorganic-organic copolymers,[23-34] the thermodynamic behavior of inorganic-organic copolymers containing salt has yet to be systematically studied. Here, we present the morphology using small angle X-ray scattering and TEM of poly(ethylene oxide)-*block*-polyhedral oligomeric silsesquioxane (PEO-POSS) mixed with a lithium bis(trifluoromethanesulfonyl) imide (LiTFSI) salt.

[†] This chapter is reported in Sethi, G. K., Jung, H. Y., Loo, W. S., Sawhney, S., Park, M. J., Balsara, N. P. & Villaluenga, I. Structure and Thermodynamics of Hybrid Organic-Inorganic Diblock Copolymers with Salt. *Macromolecules* **52,** 3165–3175 (2019).

Each POSS moiety is an inorganic silica-like core surrounded by a shell of organic butyl groups and is about 10 times larger than most typical monomers with molecular weight close to 1000 g mol^{-1}.[35]This bulkiness of POSS gives rise to unusual physical properties due to a high degree of conformational asymmetry and relative stiffness in comparison to PEO. PEO-POSS is considered a rod-coil type diblock copolymer: the chain behaves as a rigid rod for length corresponding to number of POSS monomers whereas the longer chain portions follow ideal gaussian statistics.[36-44]

The thermodynamic data from 24 PEO-POSS/LiTFSI mixtures are presented on a universal phase diagram. We use a simple equation to quantify the temperature dependence of the interaction parameter for copolymers with salt concentration ranging from $0.02 \leq [Li]/[EO] \leq 0.30$ and volume fraction of the PEO/LiTFSI rich phase, $f_{EO/LiTFSI}$, between 0.61 to 0.91. This chapter builds upon Chapter 2 wherein the morphology of electrolytes obtained from one PEO-POSS copolymer was described.[45]

3.2. Experimental

3.2.1. Materials.

PEO-acrylate (M_w = 5 kg/mol), anhydrous ethanol, anhydrous xylene, diethyl ether and tetrahydrofuran (THF) were purchased from Sigma-Aldrich, acryloisobutyl polyhedral oligomeric silsesquioxane (POSS) was purchased from Hybrid Plastic, BlocBuilder MA was kindly provided by Arkema, and lithium bis(trifluoromethanesulfonyl)-imide, $Li[N(SO_2CF_3)_2]$ (LiTFSI), was purchased from Novolyte. All chemicals were used as received.

3.2.2. Synthesis.

PEO-POSS block copolymer was synthesized by nitroxide-mediated radical polymerization (NMP). First, PEO-acrylate was reacted with BlocBuilder MA in anhydrous ethanol at 100 ºC under argon for 4h. PEO-based macroalkoxyamine was collected by precipitation in cold diethylether. Then, the POSS-acryloisobutyl monomer was polymerized using the PEO-based macroalkoxyamine as initiator in anhydrous xylene at 115 °C for 24h. The product was isolated by precipitation in cold diethyl ether, and then, centrifugation at 6500 rpm for 15 min. This step was repeated three times to obtain a white solid powder. Molecular weight was determined using H-NMR spectroscopy. The polymers used in this study are called PEO-POSS(x-y) where x and y are the molecular weights of the PEO, M_{PEO}, and POSS, M_{PPOSS}, blocks in kg mol^{-1} respectively. PEO-POSS structure is shown in Scheme 1. The overall degree of polymerization of each block was calculated by

$$N_i = \frac{M_i}{\rho_i v_{ref}} \quad [1]$$

where v_{ref} is fixed at 0.1 nm^3. The overall degree of polymerization was calculated by

$$N = N_{PEO} + N_{POSS}. [2]$$

A list of the polymer characteristics including the polydispersity index of the block copolymer, Đ, can be found in Table 1.

3.2.3. ^{1}H-NMR.

The composition of the organic-inorganic copolymers was determined using ^{1}H NMR ($CDCl_3$, Bruker AV400) measurements by integrating the characteristic peaks of the ethylene protons of PEO block (a) at 3.7 ppm versus the isobutyl end protons (b,c) at 0.63-0.65 of the POSS block. ^{1}H NMR profiles are shown in the Supporting Information (Figure S1).

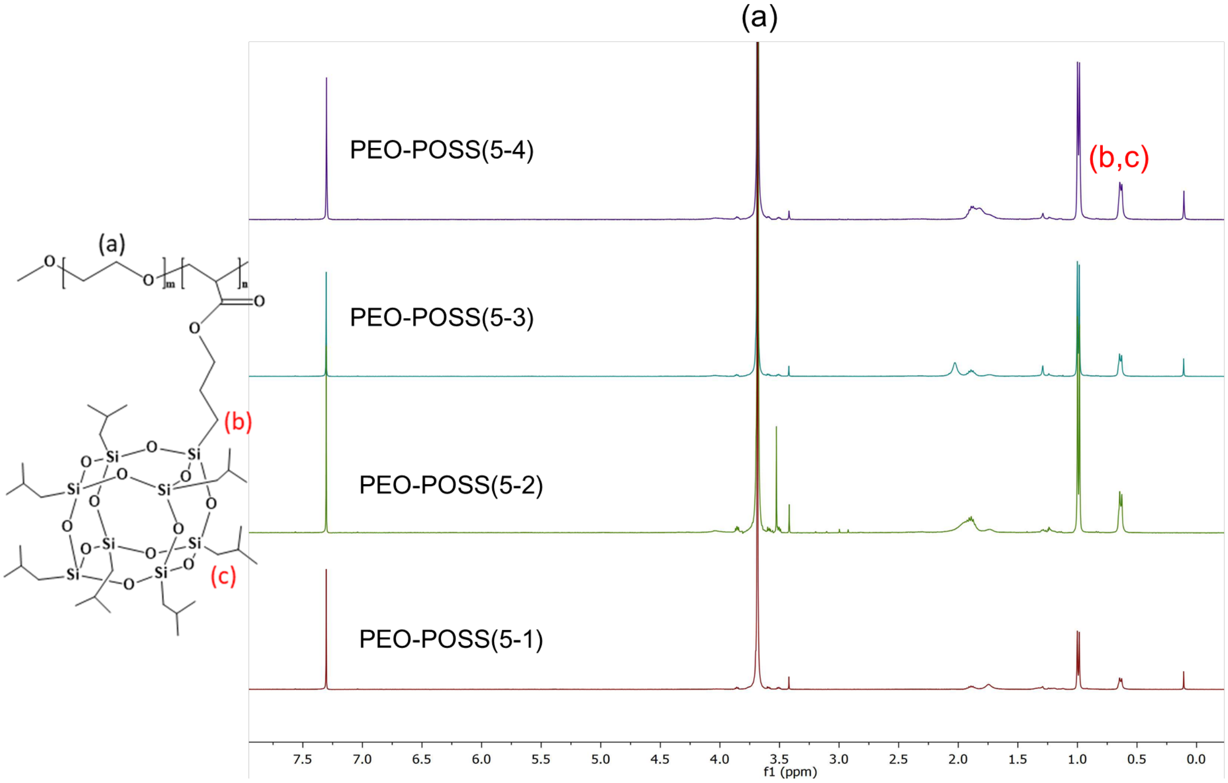

Figure 3.1. ^{1}H-NMR spectra of PEO-POSS(5-x) copolymers.

3.2.4. Electrolyte Preparation.

Electrolytes were prepared by mixing each polymer with LiTFSI. Due to the hygroscopic nature of LiTFSI, all sample preparation was carried out in an argon glovebox (MBraun) where H_2O and O_2 levels were maintained below 0.6 ppm and 1 ppm respectively. PEO-POSS polymer was dried at 90 °C under vacuum in the glovebox antechamber for 48 h, and then transferred into the glovebox. Dry polymer and LiTFSI salt were dissolved into anhydrous THF and the solutions were mixed at 60 °C for a minimum of 12 h. Once the solutes were fully dissolved, the caps were removed from the vials allowing THF to evaporate and leave behind a homogeneous polymer/salt mixture. After drying on a hotplate at 90 °C for 48 h, the electrolytes were transferred to the glovebox antechamber and dried under vacuum for 48 h at 90 °C to remove all of the THF. The dry electrolytes color ranged from clear to pale yellow and had a waxy consistency at room temperature.

The salt concentration in the copolymer was quantified by *r*, the molar ratio of lithium ions to ethylene oxide (EO) moieties. We assume that the salt resides exclusively in the PEO domain and determine the volume fraction of the PEO/LiTFSI microphase, $f_{EO/LiTFSI}$, and the volume fraction of the POSS microphase, f_{POSS}, by

$$f_{EO/LiTFSI}(r) = \frac{v_{EO} + r v_{LiTFSI}}{v_{EO} + r v_{LiTFSI} + \frac{M_{PPOSS} M_{EO}}{M_{POSS} M_{PEO}} v_{POSS}} \quad [3]$$

$$f_{POSS}(r) = 1 - f_{EO/LiTFSI}(r). \quad [4]$$

M_{POSS} and M_{EO} are the molar mass of POSS (929.61 g $\mathrm{mol^{-1}}$) and EO monomer units (44.05 g $\mathrm{mol^{-1}}$) respectively; v_{EO}, v_{POSS}, and v_{LiTFSI} are the molar volumes of ethylene oxide monomer units, POSS monomer units and LiTFSI respectively calculated using the following equation

$$v_i = \frac{M_i}{\rho_i} \quad [5]$$

where M_i and ρ_i are the molar masses of unit *i* and density of unit *i*, respectively. $\rho_{LiTFSI} = 2.392$ g $\mathrm{cm^{-3}}$; $M_{LiTFSI} = 287.09$ g $\mathrm{mol^{-1}}$;[46] $\rho_{PEO} = 1.128$ g $\mathrm{cm^{-3}}$ and $\rho_{POSS} = 1.30$ g $\mathrm{cm^{-3}}$ at 90 °C determined by the procedure outlined in ref [45] measuring the weight of a known volume of diblock copolymer. We note that the value of $\rho_{POSS} = 1.30$ g $\mathrm{cm^{-3}}$ holds for polymerized POSS, as in the three diblock copolymers PEO-POSS(5-2), (5-3) and (5-4).

PEO-POSS(5-1) which contains one POSS monomer unit, density was determined through the following experimental method. Samples were heated to 90 °C, weighed, and filled into pre-weighed aluminum pans with a known volume of 0.04 mL. Pans were hermetically sealed in an argon glovebox and excess POSS was carefully cleaned from the pan. The final weight was recorded. Density of the POSS diblock copolymer was determined by dividing the mass by the known volume of sample pans. Measurements were repeated three times to obtain a standard deviation. Density obtained was 1.11 ± 0.08 g mL^{-1}. The range of volume fractions used in this study can be found in Table 3.1.

Table 3.1. Characteristics of PEO-POSS(5-x) copolymers

PEO-POSS	POSS units	M_{PEO} (kg mol^{-1})	M_{POSS} (kg mol^{-1})	f_{EO} 90 °C	$f_{EO/LiTFSI}$ $r = 0.30$	N	$Đ$
(5-1)	1	5	0.9	0.84	0.91	88	1.17
(5-2)	2	5	1.9	0.76	0.86	97	1.06
(5-3)	3	5	2.8	0.67	0.80	109	1.04
(5-4)	4	5	3.7	0.61	0.75	121	1.04

M_{PEO} = molecular weight of the PEO block; M_{POSS} = molecular weight of the POSS block determined by H-NMR; Đ = dispersity; f_{EO} = volume fraction of PEO block at 90 °C; $f_{EO/LiTFSI}$ = EO/LiTFSI volume fraction at 90 °C at $r = 0.30$; N = chain length calculated at 90 °C and monomer reference volume of 0.1 nm^3

3.2.5. Gel Permeation Chromatography.

PEO-POSS was characterized by a Malvern Viscotek TDAmax system gel permeation chromatography (GPC) system with a mobile phase of chloroform using an injection volume of 100 µL and polymer concentration 2.0 g L^{-1}. GPC traces of PEO-POSS in relation to PEO-acrylate confirm the polymerization of the POSS block. GPC curves are shown in Figure 3.2.

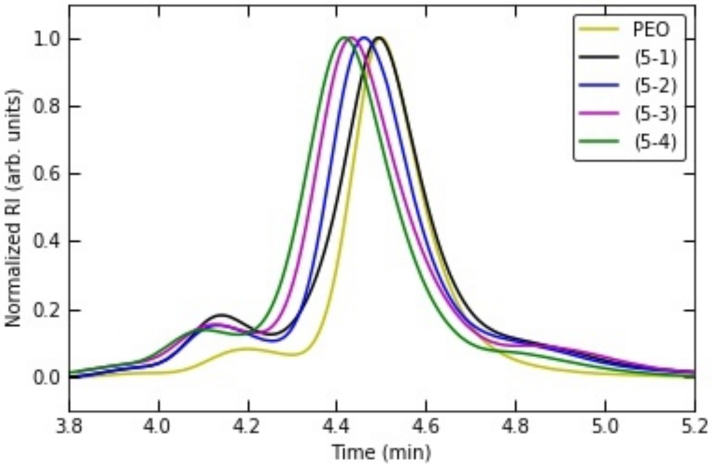

Figure 3.2. GPC Traces of PEO-POSS(5-x) copolymer

3.2.6. Thermogravimetric Analysis.

The polymer thermal degradation temperature was determined via thermogravimetric analysis (TGA) using TA Instruments Q5500 TGA-MS at the Molecular Foundry, LBNL. The sample was heated at 10 °C min^{-1} to 300-500 °C under argon. The thermal degradation temperature was recorded at 5 percent reduction in weight of the polymer sample. TGA curves and analysis are shown in Figure 3.3.

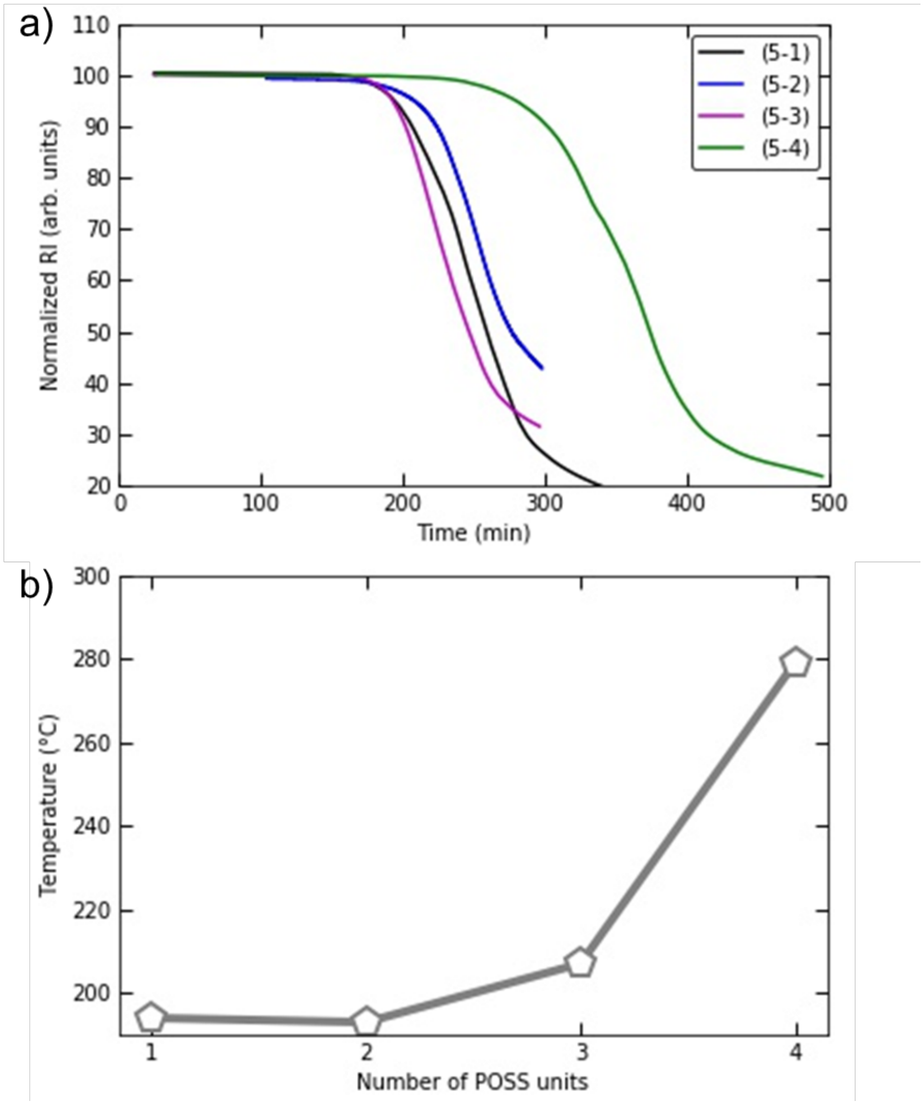

Figure 3.3. TGA data. a) TGA curves of PEO-POSS(5-x) copolymers b) Degradation temperature at 5% weight loss versus number of POSS units

3.2.7. Small Angle X-ray Scattering.

The morphologies of the electrolytes were determined by small-angle X-ray scattering (SAXS). Samples were prepared by pressing the polymer at 90 °C into 1 mm thick rubber spacers with a 1/8 in. inner-diameter and sealed with Kapton windows in custom-designed airtight holders inside of an argon glovebox. The samples were annealed at 110 °C under vacuum for at least 48 h. Measurements were performed at beamline 7.3.3. at the Advanced Light Source (ALS) at Lawrence Berkeley National Laboratory and beamline 1–5 at the Stanford Synchrotron Radiation Lightsource (SSRL) at SLAC National Accelerator Laboratory. Samples were mounted in a custom-built heating stage and held at each temperature for at least 30 min before taking measurements. Silver behenate was used to determine the beam center and sample-to-detector distance. The scattered intensity was corrected for beam transmission. Two-dimensional scattering patterns were integrated azimuthally using the Nika program for IGOR Pro[47] to produce one-dimensional scattering profiles and are reported as scattering intensity, I, as a function of the magnitude of the scattering vector, q; $q = 4\pi sin(\theta/2)/\lambda$ where θ is the scattering angle, and λ is the wavelength of the X-rays equal to 1.2398 Å. The samples were studied as a function of both increasing and decreasing temperature to ensure thermo-reversibility of all phase transitions. Samples were first heated from room temperature to the highest temperature in 20 °C increments followed by cooling in 5-10 °C increments.

3.2.8. Transmission Electron Microscopy.

PEO-POSS electrolytes were hermetically sealed within Showa-Denko pouch material in an argon glovebox to remain air and moisture free and heated to the desired temperature for 30 minutes in an oil bath. Samples were then quenched in liquid nitrogen for 5 min before allowing to return to room temperature. The electrolytes were sectioned at -120 °C using RMC Boeckeler PT XL Cryo-Ultramicrotome to obtained an ultrathin film (100 nm). The ultrathin film was transferred to a copper grid with formvar/carbon supporting film and stored in an argon glovebox immediately after cryo microtoming to minimize the effect of humidity. TEM was performed using a Philips CM 200 transmission electron microscope operating at 200 kV.

3.2.9. Differential Scanning Calorimetry.

Samples were hermetically sealed in aluminum pans in an argon glovebox. Differential scanning calorimetry (DSC) experiments were run with two heating and cooling cycles with 10 °C min^{-1} heating rates and 2 °C min^{-1} cooling rates using a Thermal Advantage Q200 calorimeter at the Molecular Foundry, LBNL. The temperature ranged from −90 to 160 °C. Melting and glass transition temperatures were obtained from analysis of the second heating stage.

3.3. Results and Discussion.

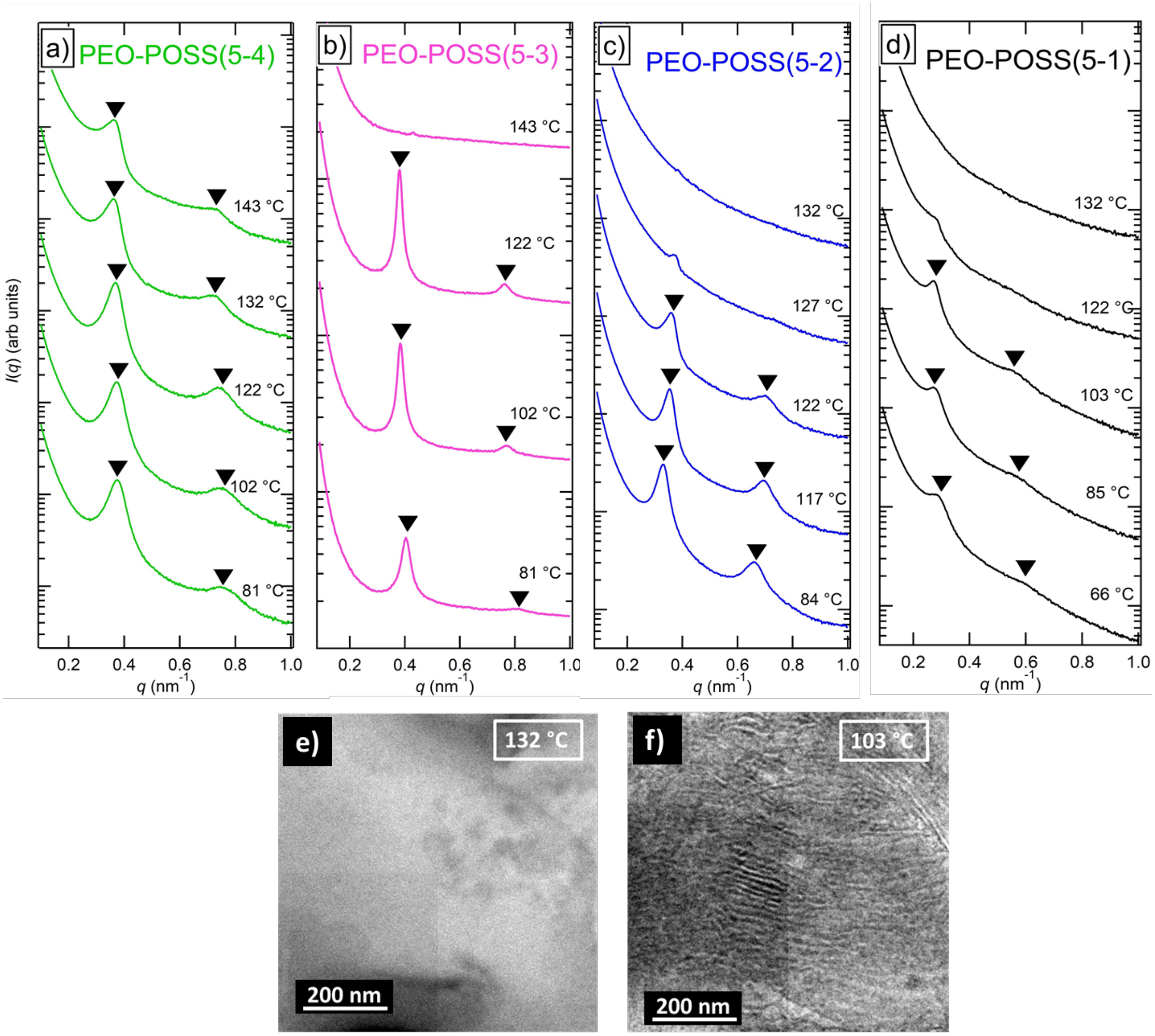

Figure 3.4. Neat SAXS profiles. SAXS intensity is plotted as a function of the magnitude of the scattering vector, *q,* for neat PEO-POSS copolymers a) PEO-POSS(5-4) b) PEO-POSS(5-3) c) PEO-POSS(5-2) d) PEO-POSS(5-1). Profiles are shifted vertically. Scans are performed upon cooling from 132 °C to 66 ° C in ~20 °C increments with temperatures indicated on the right. Triangles indicate peaks characteristic of lamellar order (q^*, $2q^*$). e-f) TEM micrographs of RuO_4 stained PEO-POSS(5-1). Separate samples were heated at 132 ° C e) and 103 ° C f) then quenched using liquid nitrogen. SAXS and TEM are consistent with each other.

Small angle X-ray scattering (SAXS) profiles of neat PEO−POSS at selected temperatures between 66 °C and 143 °C (both blocks are amorphous in this temperature range) are shown in Figure 3.4a-c where scattering intensity, $I(q)$, is plotted as a function of the magnitude of the scattering vector, q. In Figure 3.4a, we show data obtained from neat PEO-POSS(5-4). This sample exhibits an ordered lamellar morphology throughout the accessible temperature range indicated by the presence of a primary scattering peak at $q = q^* = 0.37$ nm^{-1} and a higher order peak at $q = 2q^*$ which are standard signatures of a lamellar morphology. The center-to-center distance between adjacent PEO lamellae, or domain spacing, d, of the copolymers is determined by the equation $d = 2\pi/q^* = 17$ nm. In Figure 3.4b, at 81 °C, PEO-POSS(5-3) also exhibits two peaks at $q = q^* = 0.4$ nm^{-1} and at $q = 2q^*$ indicating the presence of a lamellar phase. At 102 °C, the intensity of the primary scattering peak increases and sharpens and the second order peak becomes more prominent, indicating better long-range order. At 122 °C, the primary scattering peak and the second order peak increases and sharpens even further, showing that the long-range order improves at higher temperature. The lamellar morphology persists until 143 °C at which these two peaks disappear and instead, a monotonically decaying scattering profile is seen. Thus, an order-to-disorder transition (ODT) occurs in the neat PEO-POSS(5-3) sample at 133 ± 10 °C.

Similarly, in Figure 3.4c the scattering profiles of PEO-POSS(5-2) indicate a lamellar morphology at 84 °C and 117 °C with peaks at $q^* = 0.37$ and $2q^*$ and domain spacing 17 nm. At 122 °C, the primary scattering peak diminishes in intensity and the second order peak broadens. At 127 °C, the q^* peak decreases in intensity and the $2q^*$ peak disappears completely, indicating an ODT is approaching. This SAXS profiles indicates the presence of disordered concentration fluctuations.[68] At 132 °C, a monotonically decaying scattering profile is seen. It is evident that PEO−POSS(5-2) exhibits an ODT upon heating at 125 ± 3 °C.

In Figure 3.4d, PEO-POSS(5-1) shows a qualitatively similar profile to PEO-POSS(5-2) (Figure 1c). At 66 °C and 85 °C, we obtain a lamellar morphology with primary scattering peak at $q = q^* = 0.35$ nm^{-1} and a second order scattering peak at $2q^*$ and $d = 18$ nm. The second order scattering peak is broader and poorly defined in comparison to PEO-POSS(5-2) (Figure 1c) and PEO-POSS(5-3) (Figure 1b) indicating weaker segregation between the PEO-rich and POSS-rich phases. At 103 °C both the primary and secondary scattering peaks increase in intensity (similar to PEO-POSS(5-3) at 102 °C and 122 °C (Figure 1b)). At 122 °C, the intensity of the primary scattering peak diminishes significantly and the second order peak disappears as in Figure 1c at 127 °C indicating an ODT at 113 ± 10 °C. The monotonically decaying scattering profile at 132 °C indicates disorder.

Electron microscopy was used to confirm the lamellar and disordered morphologies seen in SAXS in Figure 3.4e-f. Two PEO-POSS(5-1) samples were annealed at 132 °C (Figure 1e) and 103 °C (Figure 3.4f), then quenched in liquid nitrogen to "freeze" the morphology at these temperatures. The resulting micrographs obtained by transmission electron microscopy (TEM) bright phase represents the RuO_4 stained PEO-rich microphases. The micrograph obtained from the sample quenched at 103 °C shows alternating dark and bright stripes representing the lamellar phase. The micrograph obtained from the sample quenched at 132 °C shows a uniform image indicating phase mixing of PEO-rich and POSS-rich phases, confirming the disordered SAXS scattering profile in Figure 3.4d at the same temperature. We chose to examine PEO-POSS(5-1) using electron microscopy because it is the most asymmetric block copolymer with $f_{EO} = 0.84$ (see

Table 3.1). In conventional block copolymers, such highly asymmetric systems would exhibit cylindrical or spherical morphologies. The TEM image in Figure 3.4e confirms our conclusion of a lamellar morphology in PEO-POSS(5-1) based on SAXS (Figure 3.4d).

The ODTs exhibited by PEO-POSS without salt is qualitatively similar to that of most all-organic diblock copolymers.[49] This suggests that the PEO and POSS chains exhibit repulsive interactions.[50-52] At low temperatures, these interactions dominate, leading to an ordered phase. At sufficiently high temperatures entropic effects dominate, leading to mixing of PEO and POSS segments.

The sharpness of the lamellar peaks decreases with increasing f_{EO}. This can be seen by comparing the low temperature data in Figures 3.4a-e. In fact, the higher order peak in PEO-POSS(5-1) is barely visible. It is evident that long-range order decreases as f_{EO} increases from 0.61 to 0.84. This is expected because the lamellae are most often found in symmetric systems. The domain spacing of PEO-POSS block copolymers are weakly dependent on the length of the POSS block, decreasing from 18 to 17 nm as N_{POSS} increases from 1 to 4.

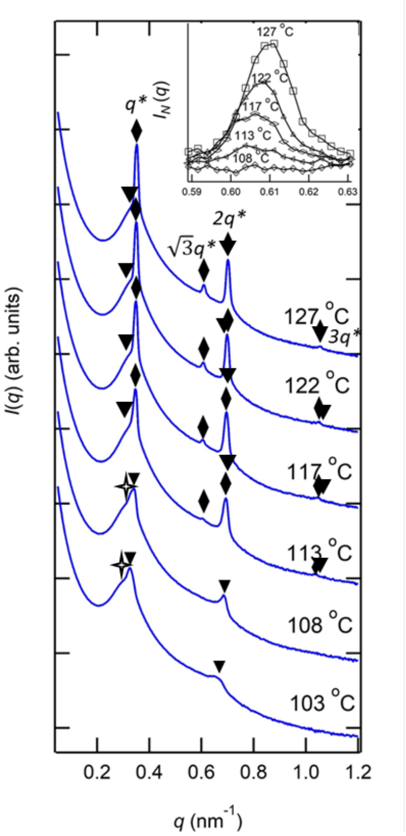

Figure 3.5. SAXS scattering profiles of PEO-POSS(5-2) $r = 0.08$. Scattering intensity is plotted as a function of the magnitude of the scattering vector, q. Profiles are shifted vertically. Scans are performed upon cooling from 127 °C to 103 ° C in ~5 °C increments with temperatures indicated on the right. The inset on the top right is the normalized scattering profile of the $\sqrt{3}q*$ peak.

The SAXS profiles obtained from a PEO−POSS(5-2)/LiTFSI mixture with $r = 0.08$ are shown in Figure 3.5. At 103 °C and 108 °C, the scattering profile exhibits two peaks at $q = q^* = 0.35$ nm^{-1} and at $q = 2q^*$ denoted with triangles indicating lamellar morphology. A second, broad scattering peak at $q = q^* = 0.35$ nm^{-1} indicates the presence of a coexisting lamellar phase, denoted by a star. The electron tomography results given in chapter 2 rule out the possibility of coexisting disordered and ordered phases. Increasing the temperature to 113 °C results in the emergence of an additional scattering peak at $q = \sqrt{3}q^*$ denoted with a diamond that is superimposed on the scattering profile of a lamellar phase, denoted by triangles. A peak at $q = \sqrt{3}q^*$ is a standard signature of a hexagonally packed cylinders morphology. It is difficult to see this peak in the intensity versus q data shown in Figure 3.5. In order to clarify the presence of the $\sqrt{3}q^*$ peak, a normalized scattering intensity is defined in equation 5

$$I_N(q) = \frac{I(q)}{I(q)\ at\ T = 84\ °C}. [5]$$

The normalized scattering profile in the vicinity of the $\sqrt{3}q^*$ peak is shown in the inset at the top right of Figure 2 at temperatures between 108 °C and 127 °C. The normalized scattering peak at 108 °C is featureless. However, a clear signature of the $\sqrt{3}q^*$ peak is seen to grow in at higher temperatures (≥ 113 °C). In chapter 2, electron tomography indicates SAXS profiles with the $\sqrt{3}$ peak indicate the presence of coexisting lamellae and hexagonally packed cylinders. In PEO-POSS(5-2) $r = 0.08$ the transition occurs at 108 ± 3 °C.

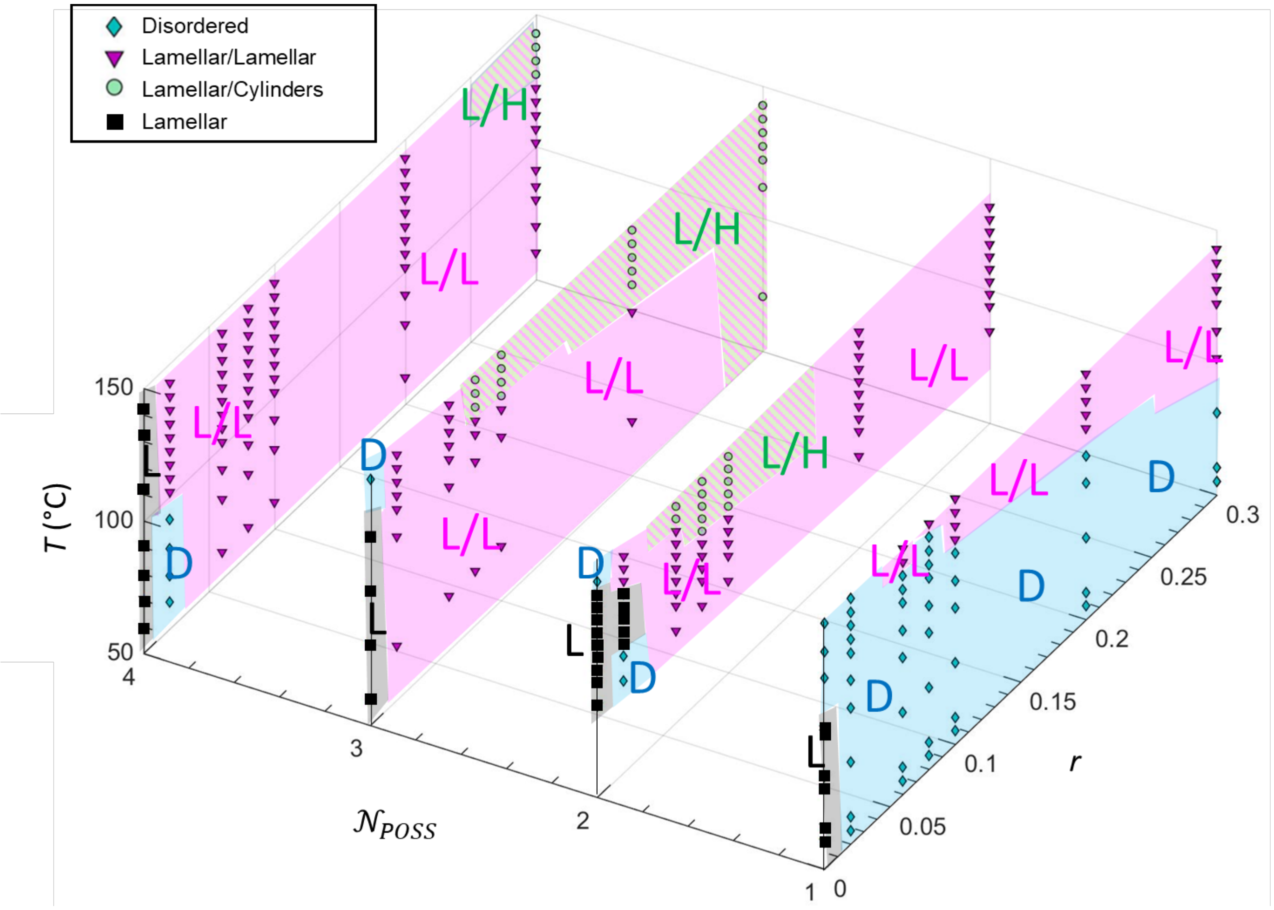

Figure 3.6. Phase diagram of PEO-POSS electrolytes summarizing morphology data determined by SAXS shown as a function salt concentration, r, number of POSS units $\mathcal{N}_{POSS}$, and temperature, T. The blue diamonds, purple triangles, and green circles and black squares represent morphological data from SAXS. The shaded regions represent the disordered (D), lamellae(L), two coexisting lamellae(L/L) and coexisting lamellae and hexagonally packed cylinder (L/H) phases respectively.

The SAXS profiles shown in Figures 3.3 and 3.4 are representative of data obtained from all of PEO-POSS without salt and PEO-POSS/LiTFSI mixtures. Depending on salt concentration, temperature, and block copolymer composition, we obtain 4 phases: disorder (D), lamellar (L), coexisting lamellae (L/L), and coexisting lamellar/hexagonally packed cylinders (L/H). Figure 3 summarizes the results of the SAXS experiments, where the morphologies of PEO−POSS/LiTFSI mixtures are shown as a function of salt concentration, number of POSS units ($\mathcal{N}_{POSS}$), and temperature. The data from each copolymer is separately shown on individual panels in Figure 3. We discuss each panel separately:

1) At $\mathcal{N}_{POSS}$ = 1, a lamellar to disorder transition upon heating is seen in the neat block copolymer. The addition of salt leads to the emergence of a wide disordered window and two coexisting lamellar phases are seen at high salt concentrations and high temperatures.

2) At $\mathcal{N}_{POSS}$ = 2, a disorder to lamellar transition upon heating is seen in the neat copolymer. A small disordered pocket is seen at r = 0.02 that gives way to a lamellar phase upon heating. At even higher temperatures, two coexisting lamellar phases are obtained. The two coexisting lamellar phases are seen over a wide window with L/H coexistence at intermediate salt concentrations and high temperatures.

3) The data at $\mathcal{N}_{POSS}$ = 3 is similar to $\mathcal{N}_{POSS}$ = 2 except for the absence of a disordered pocket at r = 0.02. A wide lamellar/lamellar window is seen with L/H coexistence at high temperatures. At r = 0.30, L/H is seen at all temperatures.

4) At $\mathcal{N}_{POSS}$ = 4, the neat polymer is ordered over the entire temperature window, a small disordered pocket is seen at r = 0.02 (similar to $\mathcal{N}_{POSS}$ = 2 but different from $\mathcal{N}_{POSS}$ = 3). The two coexisting lamellar phases occupy most of the temperatures and salt concentration window. L/H is only seen at the highest salt concentrations at temperatures above 122 °C.

The phase behavior seen in Figure 3 is extremely complex and very different from conventional block copolymers.[54] Developing a coherent framework for presenting all of these data on a single, unified plot is challenging. In this paper, attention is restricted to the electrolytes in Figure 3 ($r \geq 0.02$). A framework that includes the neat block copolymers is outside the scope of this paper. The framework is built upon an expression for the effective Flory Huggins interaction parameter, χ_{eff}, that depends on temperature and salt concentration.

A standard approach for determining χ in neat block copolymer melts is through the use of the Leibler's Random Phase Approximation (RPA) which describes scattering from concentration fluctuations in disordered systems. [48,54,55] This approach is adopted to determine χ_{eff} for salt-containing PEO-POSS. The scattering function $I_{dis}(q)$ proposed by Leibler[48] for a monodisperse AB diblock copolymer can be written as follows

$$I_{dis}(q) = C_{el}\left[\frac{S(q)}{W(q)} - 2\chi_{eff}\right]^{-1} . [6]$$

The only difference between equation 6 and that given by Leibler is the introduction of χ_{eff} instead of χ. $W(q)$ and $S(q)$ are the determinant and sum of the elements, respectively, of the structure factor matrix $\|S_{ij}\|$. The expressions $W(q)$ and $S(q)$ are given by

$$W(q) = S_{AA}(q)S_{BB}(q) - S_{AB}{}^2(q) \; [7]$$

$$S(q) = S_{AA}(q) + S_{BB}(q) + 2S_{AB}(q) \; [8]$$

where S_{AA}, S_{AB}, and S_{BB} are the pairwise elements of the structure factor matrix

$$S_{AA}(q) = NP_{EO(q)} \text{ [9]}$$

$$S_{BB}(q) = NP_{POSS(q)} \text{[10]}$$

$$S_{AB}(q) = \frac{N}{2}[\,P_{Total} - \, P_{EO} - P_{POSS}]. \text{[11]}$$

$P_{EO}(q)$ is the form factor of the PEO block modeled as a Gaussian chain [49]

$$P_{EO} = \frac{2}{x^2}\left[f_{EO/LiTFSI}x + e^{-f_{EO/LiTFSI}x} - 1\right] \text{ [12]}$$

$$x = \, q^2R_g^2 \text{ [13]}$$

$$R_g^2 = \frac{Na^2}{6} \text{ [14]}$$

where R_g is the radius of gyration of the copolymer. The PEO block and LiTFSI are considered to be one component and POSS is the other component. $P_{POSS}(q)$ is the form factor of the POSS block modeled as a rodlike chain[56]

$$P_{POSS}(q) = \frac{2}{x^2}[f_{POSS}x + e^{-f_{POSS}x} - 1] + \frac{1}{15xf_{POSS}N}[-11xf_{POSS}e^{-f_{POSS}x} + 4f_{POSS}x \\ + 7(1 - e^{-f_{POSS}x}). \text{[15]}$$

$P_{total}(q)$ is the form factor of the entire chain modeled as a Gaussian chain.

$$P_{total}(q) = \frac{2}{x^2}[x + e^{-x} - 1]. \text{[16]}$$

This is clearly an approximation. Results obtained with $P_{total}(q)$ given by the rodlike chain (equation 15 with $f_{POSS} = 1$) is shown in the Supporting Information. The final results are virtually indistinguishable. Thus equation 16 is used in the analysis below. C_{el} in equation 6 is the electron density contrast between the PEO/LiTFSI and POSS given by

$$C_{el} = v_{ref}\,\left[B_{EO/LiTFSI} - B_{POSS}\,\right]^2 \text{ [17]}$$

where v_{ref} is the same reference volume of 0.1 nm^3 used to define N, N_{POSS}, N_{PEO}, and χ_{eff}; $B_{EO/LiTFSI}$ and B_{POSS} are the scattering length density of EO/LiTFSI and POSS, respectively. $B_{EO/LiTFSI}$ scattering length density is calculated as follows

$$B_{EO/LiTFSI} = Y_{LiTFSI}B_{LiTFSI} + (1 - Y_{LiTFSI})B_{EO} \; [18]$$

where B_i is given by

$$B_i = \frac{r_e \, n_i \, N_{AVG} \, \rho_i}{M_i} \; [19]$$

and Y_{LiTFSI} is the volume fraction of LiTFSI in the PEO/LiTFSI microphase calculated by

$$Y_{LiTFSI} = \frac{r \, M_{LiTFSI} \, \rho_{EO}}{r \, M_{EO} \, \rho_{LiTFSI} + r \, M_{LiTFSI} \, \rho_{EO}}. [20]$$

In equation 19, r_e is the cross-sectional scattering radius of a free electron; n_i is the number of electrons per i; N_{AVG} is Avogadro's number; ρ_i is the density of i; and M_i is the molar mass of i. The density of the EO/LiTFSI calculation is shown in ref [46].

In principle, equations 6-20 can be used to predict the scattering from a PEO-POSS/LiTFSI mixture with χ_{eff} and R_g as fitting parameters. When this was done, we found systematic disagreement between theory and experiment. The agreement between theory and experiment improved considerably if the contrast term is used as an additional fitting parameter. All analysis thus is based on three parameter fits: χ_{eff}, R_g, and C_{fit}. The average deviation between C_{el} and C_{fit} is 8% as shown in the Supporting Information (Figure S5). This suggests that the simplification of combining EO and LiTFSI may not be strictly accurate.

It is evident from Figures 1 and 2 that the scattering peaks are superposed on a monotonically decaying background. The following expression is used to estimate this background

$$I_{bkg}(q) = xq^y + z \; [21]$$

where x, y and z are simply fitting parameters. The experimental scattering profiles analyzed below are obtained after background subtraction.

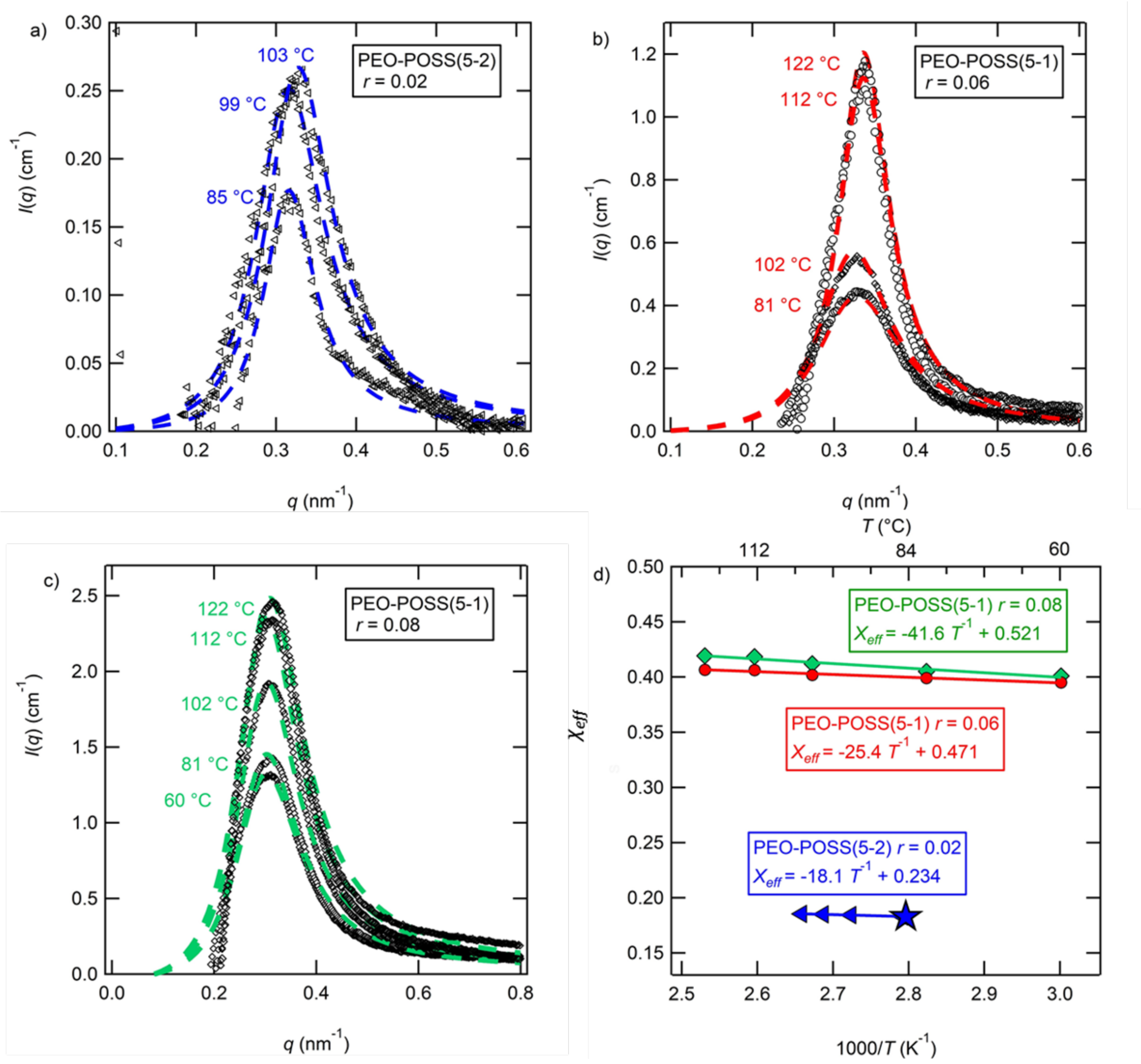

Figure 3.7. RPA fits. a) SAXS intensity profile for PEO-POSS(5-2) with salt concentration at r = 0.02 at various temperatures and the corresponding RPA fits (dashed line). b) PEO-POSS(5-1) r = 0.06 c) PEO-POSS(5-1) r = 0.08 d) χ_{eff} plotted as a function of inverse temperature (a star marker refers to a sample at a temperature below the POSS block crystallization transition temperature).

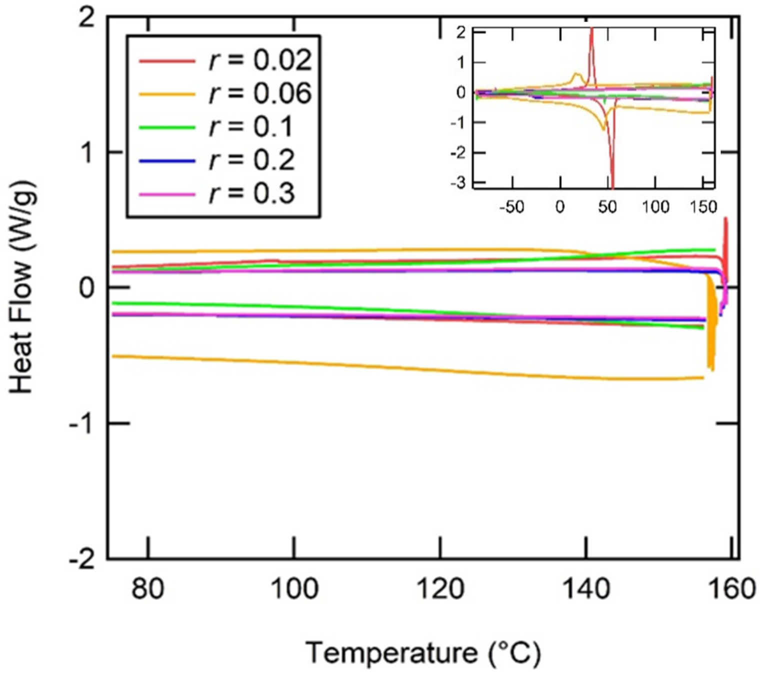

Figure 3.8. DSC thermograms of PEO-POSS(5-1) at all salt concentrations in the vicinity of the POSS crystallization/melting transition. The inset shows the same data on a larger temperature scale. The DSC thermograms do not exhibit POSS crystallization and melting transitions.

Typical background subtracted scattering profiles of disordered PEO-POSS/LiTFSI mixtures are shown in Figures 3.7a-c. The RPA fits are shown by dashed lines in these figures. Figure 3.7a shows disordered SAXS scattering profiles of PEO-POSS(5-2) r = 0.02 between 85 and 103 °C in the vicinity of $q*$. The dashed lines are the RPA fits to the scattering data. Here, the fits conform well to the data. The $q*$ peak at 85 °C exhibits maximum absolute scattering intensity of 0.18 cm^{-1} corresponding to a fitted χ_{eff} = 0.1833. The peak grows with increasing temperature; the $q*$ peak at 103 °C exhibits maximum absolute scattering intensity of 0.22 cm^{-1} which corresponds to a slightly increased value of χ_{eff} = 0.1854. Similar trends are seen in Figure 4b for the case of PEO-POSS(5-1) r = 0.06 and Figure 3.7c for the case of PEO-POSS(5-1) r = 0.08. In Figure 4b, the primary scattering peak grows in intensity between 81 °C to 122 °C. In Figure 3.7c, the primary scattering peak grows in intensity between 60 °C to 122 °C.

The dependence of χ_{eff} on temperature for the three disordered electrolytes discussed in the preceding paragraph is shown in Figure 4d. The standard form for determining the temperature dependence of χ_{eff} is used.

$$\chi_{eff} = A + \frac{B}{T} \; [22]$$

The dashed lines in Figure 3.7d are fits of equation 22 which give parameters A and B, where B is negative for all cases. The temperature dependence of χ_{eff} is weak relative to the dependence of salt concentration. χ_{eff} increases by a factor of 2.4 when r is increased from 0.02 to 0.06 (Figure 4d). In contrast, χ_{eff} only increases by a factor of about 1.004 over the accessible temperature range. Interestingly, increasing r from 0.06 to 0.08 results in a modest increase in χ_{eff}.

Up until this point, we have not discussed the crystallinity of the POSS block in these samples. We have used DSC to determine the state of POSS chains in the disordered samples shown in Figure 3.7a-d. The POSS chains in PEO-POSS(5-1)/salt mixtures are amorphous, *i.e.,* the DSC thermograms do not exhibit POSS crystallization and melting transitions. Figure 3.8 shows the DSC thermograms in the vicinity of the POSS crystallization and melting transition temperature. We determine that, with the exception of 1 sample, the POSS block is amorphous in all of the samples used in this analysis (PEO-POSS(5-2) $r = 0.02$ is semicrystalline below 95 °C). The semicrystalline sample is identified by a star marker. It is evident that the none of the analysis is affected by the crystallinity of the POSS block. The semicrystalline nature of the POSS block in PEO-POSS(5-2) $r = 0.02$ is discussed in greater detail in Chapter 4.

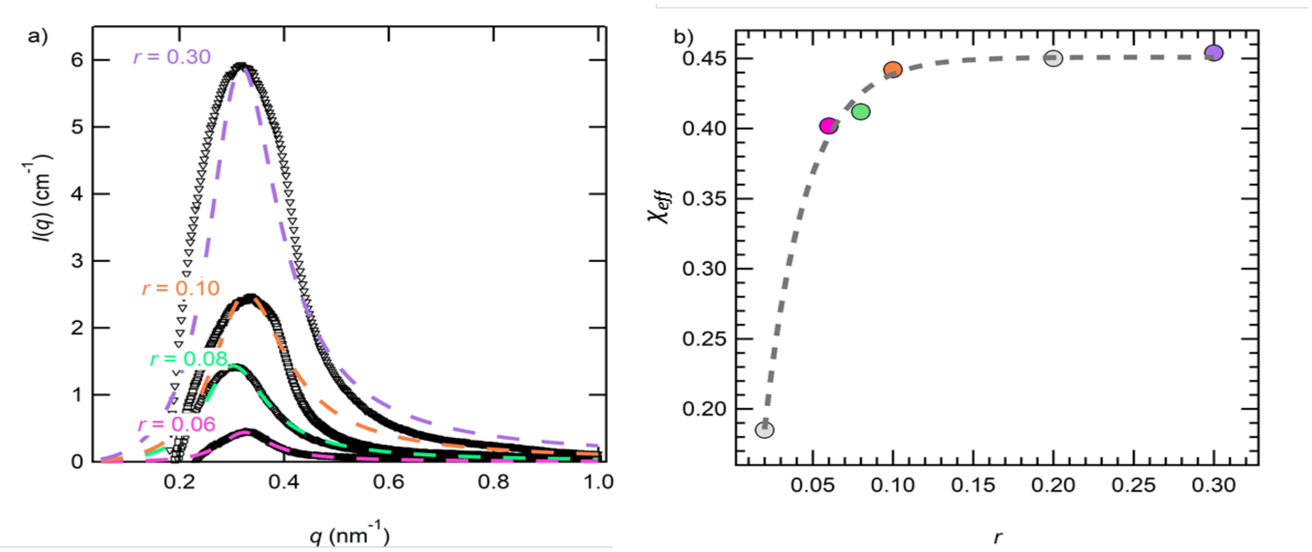

Figure 3.9. RPA fits at different salt concentrations. a) SAXS intensity is plotted as a function of the magnitude of the scattering vector, q, in PEO-POSS(5-1) with salt concentration at $r = 0.06$ to $r = 0.30$ and the corresponding RPA fits (dashed line) at 60 °C. b) χ_{eff} versus salt concentration at 60 °C. The colored markers correspond to values obtained by RPA fits in a). The dashed line is the fit to equation 23.

The analysis described in the preceding paragraph was applied to all disordered PEO-POSS/LiTFSI mixtures with $r \geq 0.02$. In most cases, the agreement between theory and experiment was similar to that shown in Figure 3.7. The largest disagreements occur in PEO-POSS(5-1). The RPA equations were not developed for complex molecular architectures such as PEO-POSS block copolymers, thus one expects deviation between experiment and theory. Figure 3.9a demonstrates disordered state scattering profiles from this electrolyte at selected values of r and at a fixed temperature at 60 °C. The values of χ_{eff} obtained from this analysis is shown in Figure 3.9b. It is evident that χ_{eff} increases rapidly with increasing r at low values of r ($r < 0.08$). The increase in χ_{eff} from $r = 0.1$ to $r = 0.3$ is less dramatic.

The data in Figure 3.9b is fit to an exponential equation plotted as a dashed line through the points.

$$\chi_{eff} = C - De^{-Er} \quad [23]$$

where C, D, and E are empirically determined fitting parameters described in Table 3.2.

Table 3.2. The best-fit exponential equation parameters of all χ_{eff} in PEO-POSS electrolytes

C	$4.5084 \times 10^{-1} \pm 0.0059$
D	$5.7524 \times 10^{-1} \pm 0.0496$
E	$3.8687 \times 10^{1} \pm 4.30$

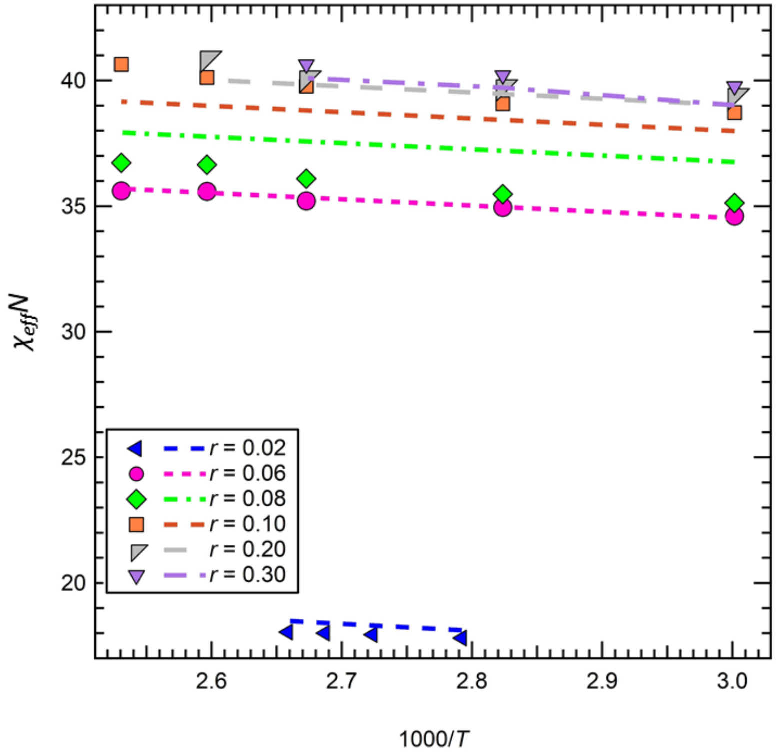

Figure 3.10. Effective segregation strength $\chi_{eff}N$ plotted as a function of inverse temperature for a range of salt concentrations $0.02 \leq r \leq 0.30$. Dashed lines indicate predictions based on equation 24. For the given value of r the colors of the dashed lines correspond to the markers of the same color.

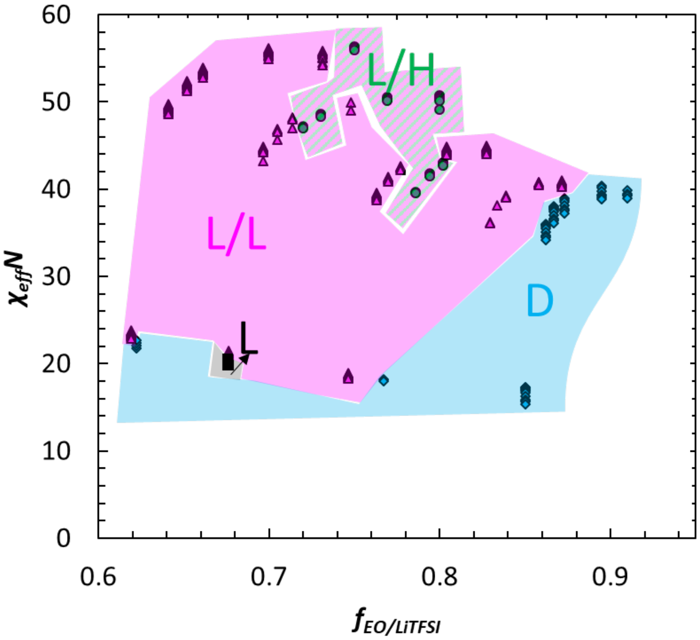

Figure 3.11. Morphology data for PEO-POSS block copolymer electrolytes plotted as a function of $\chi_{eff}N$ versus volume fraction of the salt containing phase, $f_{EO/LiTFSI}$. Coexisting lamellar (L/L), lamellae (L) and disordered (D) regions and coexistence of lamellae and hexagonally packed cylinders (L/H) is denoted by pink, gray, blue and hatched colored regions, respectively.

Combining equations 22 and 23 the following expression is obtained for the dependence of χ_{eff} on T and r where A' combines A from equation 22 and C from equation 23

$$\chi_{eff}(T,\, r) = A' + \frac{B}{T(K)} - De^{-Er}\,.[24]$$

The empirically determined constants A'-E are given in Table 3.3.

Table 3.3 The best-fit equation parameters of all χ_{eff} in PEO-POSS electrolytes

A’	$4.5884 \times 10^{-1} \pm 0.00591$
B (K)	$-2.8021 \times 10^{-2} \pm 0.00982$
D	$5.7524 \times 10^{-1} \pm 0.0496$
E	$3.8687 \times 10^{1} \pm 4.30$

In Figure 3.10 experimentally determined dependence of segregation strength ($\chi_{eff}N$) on temperature and salt concentration is compared with the prediction based on equation 24. The dashed lines in Figure 6 indicate the $\chi_{eff}N$ calculated from equation 24 in the same color as the data points which they represent. It is evident that equation 24 provides a reasonable description of all measured values of $\chi_{eff}N$.

The morphology data determined via SAXS for all PEO-POSS/LiTFSI mixtures, presented in Figure 3.6 on a three-dimensional plot, are recast in Figure 3.11 on a two-dimensional plot of $\chi_{eff}N$ calculated from expression 24 as the y-axis and $f_{EO/LiTFSI}$ as the x-axis. Figures 3.6 and 3.11 use the same color scheme. The phase diagram (Figure 3.11) is dominated by the lamellar/lamellar coexisting phase which is found in the range $0.60 \leq f_{EO/LiTFSI} \leq 0.85$ and $20 \leq \chi_{eff}N \leq 50$. The wide stabilization of the coexisting lamellar phase is perhaps due to the conformational asymmetry in PEO-POSS (i.e. $a_{POSS}/a_{PEO} > 1$).[38,57] A pocket of coexisting hexagonally packed cylinders/lamellae is found in the range $0.72 \leq f_{EO/LiTFSI} \leq 0.81$ and $37 \leq \chi_{eff}N \leq 58$. The lower portion of the phase diagram ($0 \leq \chi_{eff}N \leq 20$) is largely disordered. This disordered phase exists up to $\chi_{eff}N$ up to 40. We note that all of the complexity seen in the three-dimensional phase diagram in Figure 3.6 maps onto contiguous regions on the $\chi_{eff}N$ versus $f_{EO/LiTFSI}$ plot. This was made possible by our analysis of scattering in the disordered state which led to equation 24.

3.4. Conclusion

The effect of salt addition on the self-assembly behavior is studied in organic-inorganic PEO-POSS block copolymer electrolytes. The phase behavior of PEO-POSS/LiTFSI is reported in mixtures with volume fraction, $f_{EO/LiTFSI}$ ranging from 0.61 to 0.91, chain length, N, from 88 to 121, temperatures from 60 to 143 °C, and salt concentration from $r = 0.02$ to 0.30. Without salt, PEO−POSS presents a classical order-to-disorder transition upon heating. The addition of salt at low concentration ($r \leq 0.02$) results in the stabilization of the disordered phase. However, further increase in salt concentration results in the stabilization of ordered phases. The segregation strength of the polymer electrolytes ($\chi_{eff}N$) is determined by analyzing disordered scattering profiles using Leibler's Random Phase Approximation.[48] The PEO block was modeled as a flexible Gaussian chain while the POSS block was modeled as a rodlike chain. The results obtained from electrolytes with $r \geq 0.02$ are summarized on a phase diagram that shows the dependence of the ordered morphology on $\chi_{eff}N$ and $f_{EO/LiTFSI}$. Only three ordered phases were found: lamellae, 2 coexisting lamellae phases, and coexisting lamellae/hexagonally packed cylinders. Further work on understanding the molecular origins of the observed phase behavior of PEO-POSS/LiTFSI is warranted.

LIST OF SYMBOLS

a	statistical segment length (nm)
B_i	scattering length density of species i
C_{el}	calculated electron density contrast term

C_{fit}	fitted electron density contrast term
d	domain spacing (nm)
Đ	dispersity
f_i	volume fraction of the species *i*
$f_{EO/LiTFSI}$	volume fraction of PEO/LiTFSI microphase
I	scattering intensity
I_{dis}	disordered scattering intensity (cm^{-1})
I_{bkg}	background scattering intensity (cm^{-1})
I_N	normalized scattering intensity
M_{PEO}	molecular weight of the poly(ethylene oxide) block (kg mol^{-1})
M_{PPOSS}	molecular weight of the polyhedral oligomeric silsesquioxane block (kg mol^{-1})
M_i	molecular weight of species *i* (g mol^{-1})
N	degree of polymerization
N_i	degree of polymerization of species *i*
$\boldsymbol{\mathcal{N}}_{\mathrm{POSS}}$	number of POSS units
q	scattering vector (nm^{-1})
$q*$	scattering vector at the primary scattering peak (nm^{-1})
r	salt concentration ([Li] [EO]$^{-1}$)
R_g	radius of gyration (nm)
T	Temperature (°C)
Y	volume fraction salt in PEO/LiTFSI microphase (LiTFSI cm^3 PEO/LiTFSI cm^{-3})

GREEK

v_i	molar volume of species *i* (cm^3 mol^{-1})
v_{ref}	reference volume of species *i* (cm^3 mol^{-1})
ρ_i	density of species *i* (g cm^{-1})
θ	X-ray scattering angle
λ	X-ray wavelength

χ Flory-Huggins interaction parameter

χ_{eff} Flory-Huggins interaction parameter of PEO-POSS/LiTFSI

3.5. Supporting Information

Table 3.4. Summary of DSC data for PEO block transitions in PEO-POSS(5-x)/LiTFSI mixtures

PEO-POSS	r	T_g (°C)	T_m (°C)
(5-1)	0	-	58.81
(5-1)	0.02	-66.22	50
(5-1)	0.06	-45.7	41.82
(5-1)	0.08	-45.01	-
(5-1)	0.1	-31.1	-
(5-1)	0.2	-25.74	46.75
(5-1)	0.3	-16.85	-
(5-2)	0	-	56.93
(5-2)	0.02	-	56.13
(5-2)	0.06	-	52.25
(5-2)	0.08	-44.87	34.73
(5-2)	0.1	-42.51	-
(5-2)	0.2	-24.36	44.25
(5-2)	0.3	-11.24	80.82
(5-3)	0	-	56.78
(5-3)	0.02	-	-
(5-3)	0.06	-65.85	39.79
(5-3)	0.08	-39.475	40.16
(5-3)	0.1	-42.96	-
(5-3)	0.2	-24.87	-
(5-3)	0.3	-10.02	76.38
(5-4)	0	-	53.71
(5-4)	0.02	-	52.24
(5-4)	0.06	-	41.52
(5-4)	0.08	-45.75	-
(5-4)	0.1	-40.21	-
(5-4)	0.2	-22.17	-
(5-4)	0.3	-9.29	-

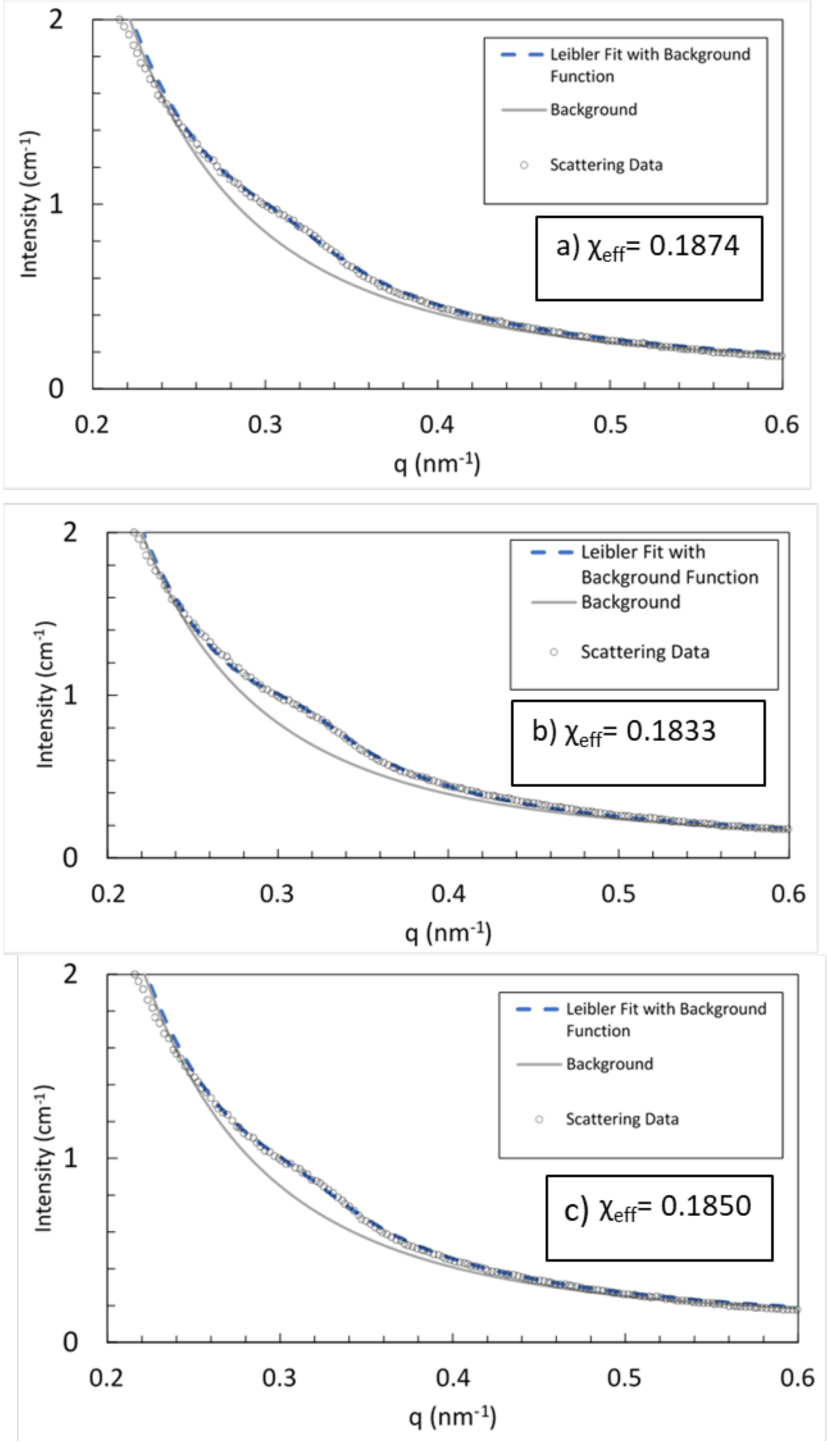

Figure 3.12. Variation of RPA fits. RPA fit modeled $P_{total}(q)$ as a a) rod-like chain b) coil-like chain and c) with P_{EO} and P_{POSS} as both coil-like chains in PEO-POSS(5-2) *r* = 0.02 at 85 °C.

Table 3.5. All RPA results of disordered PEO-POSS(5-2)/LiTFSI mixtures

PEO-POSS	r = [Li]/[EO]	T (°C)	C (cm^{-1})	C_{fit} (cm^{-1})	R_g (nm^{-1})	χ_{eff}
(5-2)	0.02	85	0.003	0.0016	7.10	0.1833
(5-2)	0.02	94	0.003	0.0016	7.03	0.1844
(5-2)	0.02	99	0.003	0.0016	7.12	0.1851
(5-2)	0.02	103	0.003	0.0016	6.97	0.1854
(5-1)	0.06	60	0.012	0.015	8.95	0.395
(5-1)	0.06	81	0.012	0.010	8.60	0.399
(5-1)	0.06	102	0.012	0.01	8.77	0.4019
(5-1)	0.06	112	0.012	0.01	8.42	0.4062
(5-1)	0.06	122	0.012	0.01	8.40	0.4065
(5-1)	0.08	60	0.082	0.10	9.75	0.401
(5-1)	0.08	81	0.082	0.06	9.78	0.419
(5-1)	0.08	102	0.082	0.08	9.71	0.4189
(5-1)	0.08	112	0.082	0.1	9.72	0.4184
(5-1)	0.08	122	0.082	0.11	9.59	0.4175
(5-1)	0.10	60	0.105	0.12	9.38	0.442
(5-1)	0.10	81	0.105	0.12	9.36	0.446
(5-1)	0.10	102	0.105	0.12	9.37	0.454
(5-1)	0.10	112	0.105	0.12	9.87	0.458
(5-1)	0.10	122	0.105	0.12	9.36	0.464
(5-1)	0.20	60	0.229	0.16	9.32	0.45
(5-1)	0.20	81	0.229	0.16	9.00	0.454
(5-1)	0.20	102	0.229	0.16	9.36	0.458
(5-1)	0.20	112	0.229	0.16	9.16	0.467
(5-1)	0.30	60	0.359	0.23	9.73	0.454
(5-1)	0.30	81	0.359	0.25	9.37	0.459
(5-1)	0.30	102	0.359	0.28	9.36	0.464

4. Effect of crystallization of the polyhedral oligomeric silsesquioxane block on self-assembly in hybrid organic-inorganic block copolymers with salt[†]

ABSTRACT

We present a DSC and X-ray scattering study investigating the effect of polyhedral oligomeric silsesquioxane (POSS) block crystallinity on the self-assembly of a poly(acryloisobutyl polyhedral oligomeric silsesquioxane)-*b*-poly(ethylene oxide)-*b*-poly(acryloisobutyl polyhedral oligomeric silsesquioxane) (POSS-PEO-POSS) triblock copolymer and poly(ethylene oxide)-*b*-poly(acryloisobutyl polyhedral oligomeric silsesquioxane) (PEO-POSS) diblock copolymers mixed with lithium bis(trifluoromethanesulfonyl)imide salt. The POSS block in all copolymer/salt mixture organizes into a rhombohedral crystal, similar to that of the POSS homopolymer. Semicrystalline polymer/salt mixtures favor morphologies with flat interfaces (*i.e.*, lamellae) despite the asymmetric nature of the copolymers; POSS volume fractions range from 0.76 - 0.85. Coexisting lamellae and hexagonally packed cylinders as well as coexisting lamellae with different domain spacings are seen in many copolymer/salt mixtures wherein the POSS block is amorphous. Morphological phase transitions in these systems are seen in the vicinity of the POSS crystallization temperature.

4.1. Introduction.

The self-assembly and phase behavior of block copolymers is a subject of continuing interest. It is generally believed that the morphology obtained in these systems is governed by four parameters: copolymer composition, chain length, molecular architecture (diblock versus triblock copolymer), and Flory Huggins interaction parameter, c. Microphase separation is observed when χ exceeds a critical value. [68] This is, however, only true for systems wherein both blocks are amorphous; most of the systematic experimental and theoretical studies in this field have focused on this case. [61, 82,92–94] In a pioneering study, Whitmore and Noolandi predicted the phase behavior of systems wherein one of the blocks was semicrystalline, assuming that only lamellar morphologies would be obtained. [95] This assumption is reasonable as semicrystalline polymer chains fold into lamellar motifs which are commensurate with the self-assembled lamellar morphology. [96–98]

[†] This chapter is reported in Sethi, G. K., Chakraborty, S., Zhu, C., Schaible, E., Villaluenga, I. & Balsara, N. P. Effect of crystallization of the polyhedral oligomeric silsesquioxane block on self-assembly in hybrid organic-inorganic block copolymers with salt. *Giant* **6,** 100055 (2021).

It is important to distinguish between lamellae formed by folded crystalline polymers which are obtained in both homopolymer and block copolymers and lamellae formed by block copolymers due to microphase separation. However, relatively few studies have been conducted on such systems. [99–101] Compared to amorphous systems, our knowledge of the factors that control the morphology of semicrystalline block copolymers is limited. For instance, it is not clear if a semicrystalline block copolymer can be disordered (*i.e.* one of the blocks forms crystals but the block copolymer does not exhibit microphase separation).

There is a growing interest in the morphology of block copolymers with added salt due to their potential applications as solid electrolytes in rechargeable batteries. [28] The ions are segregated in the amorphous block, usually poly(ethylene oxide) above the crystalline melting temperature. The mechanical properties of these electrolytes are controlled mainly by the nonconducting block. While in principle the nonconducting block could be either glassy or semicrystalline, most studies to date have focused on glassy blocks such as poly(styrene). [58,60]

In this chapter, we study the effect of added salt on morphology in three hybrid organic-inorganic block copolymers: two poly(ethylene oxide)-*b*-poly(acryloisobutyl polyhedral oligomeric silsesquioxane) (PEO−POSS(x-y)) diblock copolymers and a poly(acryloisobutyl polyhedral oligomeric silsesquioxane)-*b*- poly(ethylene oxide)-*b*-poly(acryloisobutyl polyhedral oligomeric silsesquioxane) (POSS-PEO-POSS(y-x-y)) triblock copolymer (x and y refer to the molecular weight of the PEO block and the POSS block in kg mol^{-1} rounded to the nearest whole number). The chemical structures of PEO-POSS and POSS-PEO-POSS are shown in Figure 4/1a and b. The first diblock copolymer, PEO-POSS(5-2), contains PEO and POSS blocks with molecular weights of 5 and 1.9 kg mol^{-1}, respectively. The second diblock copolymer, PEO-POSS(10-4) is similar but has double the molecular weight (PEO and POSS blocks with molecular weights of 10 and 3.8 kg mol $^{-1}$, respectively). The triblock copolymer, POSS-PEO-POSS(2-10-2), contains a PEO chain flanked by POSS segments, and the molecular weights of the PEO and POSS blocks are 10 and 1.9 kg mol $^{-1}$, respectively. The volume fraction of the PEO block, f_{EO}, is 0.76 in all three block copolymers. The salt used in this study is lithium bis(trifluoromethanesulfonyl)imide (LiTFSI). It has been noted that the self-assembly of triblock copolymers is similar to that of diblock copolymers obtained by cutting the chains in the middle. [102–106] PEO-POSS(5-2) and POSS-PEO-POSS(2-10-2) allow for the study of this effect. Comparing PEO-POSS(10-4) and POSS-PEO-POSS(2-10-2) enables a study of the effect of molecular architecture (diblock versus triblock copolymers) at fixed volume fraction and chain length. The three polymers are shown in Figure 4.1c.

This chapter is a continuation of the previous chapters investigating morphology and thermodynamic properties of PEO and POSS-containing copolymers. In Chapter 2, we analyzed the phase behavior of a series of PEO-POSS(5-2)/salt mixtures as a function of temperature and salt concentration. In Chapter 3, we determined the morphology of a series of PEO-POSS diblock copolymer/salt mixtures of varied molecular weight, volume fraction, salt concentration, and temperature. The morphology was interpreted using *c* determined by analyzing the scattering from disordered systems. More recently, in ref [107], the effect of POSS-block crystallinity on the reversibility of grain structure changes upon heating and cooling in one POSS-PEO-POSS(2-10-2)/salt mixture is shown.

In the present chapter, we begin with a detailed study of the semicrystalline nature of the POSS block using differential scanning calorimetry and wide-angle X-ray scattering. This is followed by determination of the morphology using small-angle X-ray scattering. I conclude by exposing the effect of crystallization on morphology.

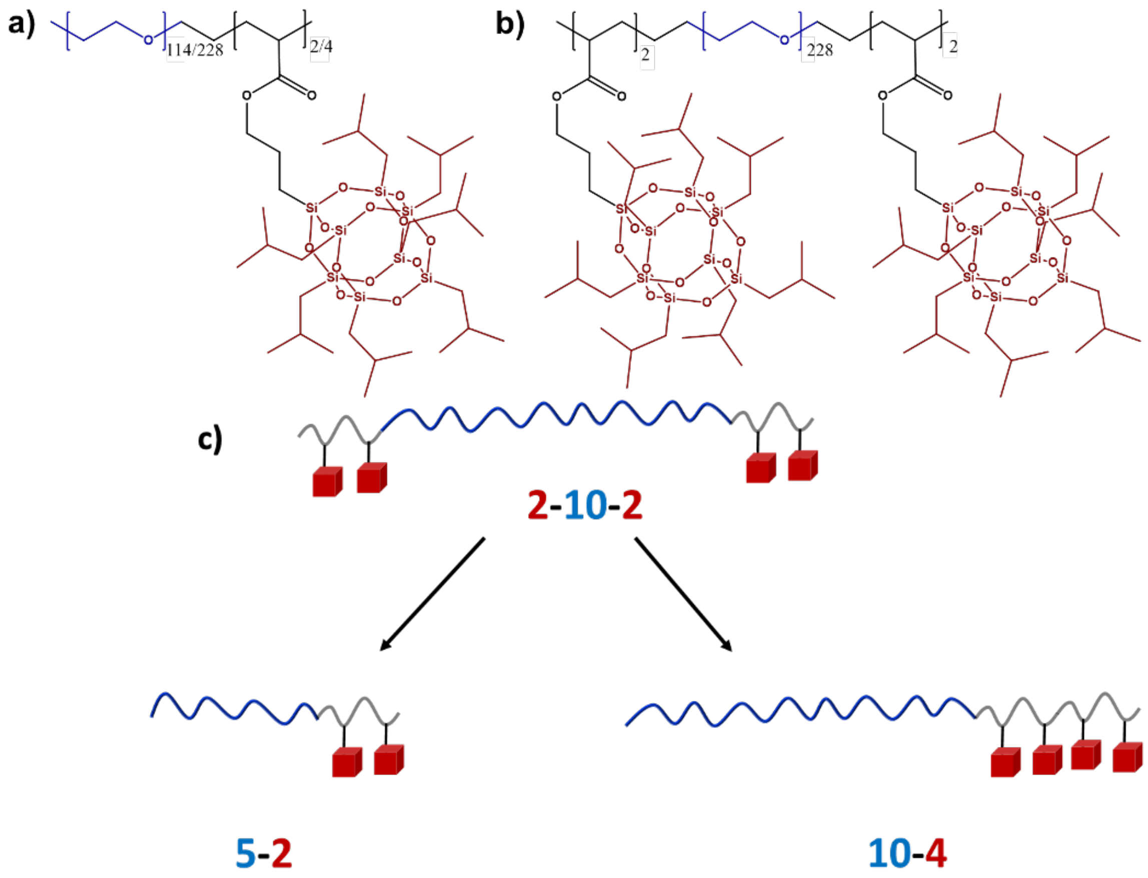

Figure 4.1. Hybrid organic-inorganic copolymer chemical structures. a) PEO-POSS chemical structure where POSS repeat units are 2 in PEO-POSS(5-2) or 4 in PEO-POSS(10-4) and EO repeat units are 114 in PEO-POSS(5-2) and 228 in PEO-POSS(10-4). b) POSS-PEO-POSS(2-10-2) chemical structure where POSS repeat units are 2 at both the chain ends and EO repeat units are 228. c) Hybrid organic-inorganic copolymer chemical structure cartoons. Triblock copolymer, POSS-PEO-POSS(2-10-2) is cut in half to make the smaller diblock copolymer, PEO-POSS(5-2), and is rearranged to form the larger diblock copolymer, PEO-POSS(10-4).

4.2 Experimental

4.2.1 Materials.

PEO-acrylate (M_{PEO} = 10 kg mol^{-1}), lithium bis(trifluoromethanesulfonyl)-imide, Li[N(SO_2CF_3)$_2$] (LiTFSI), tetrahydrofuran, toluene and 1,4-dioxane was purchased from Sigma-Aldrich. Acryloisobutyl POSS was purchased from Hybrid Plastics. BlocBuilder MA was kindly provided by Arkema. All chemicals were used as received.

4.2.2. Synthesis.

PEO-POSS block copolymers were synthesized by nitroxide mediated radical polymerization (NMP). as described in Chapter 2. POSS-PEO-POSS block copolymer was synthesized by atom transfer radical polymerization (ATRP) as described in ref [107]. POSS homopolymer synthesis is performed by combining 5 g acryloisobutyl POSS (5.4 mmol) with 103 mg (0.27 mmol) BlocBuilder MA and 50 mL 1,4-dioxane. The solution was purged with N_2 for 30 minutes. The reaction occurred at 90 °C for 5 hours. The product was cooled, and pure polymer was obtained by reprecipitating 5 times in cold methanol. Molecular weight was determined using ^{1}H NMR spectroscopy. GPC traces the POSS homopolymer confirm the polymerization of the POSS block. Due to the complex molecular structure and potential interactions between the polymer segments and the columns, we only use the GPC data to confirm the POSS polymerization. [107,108]

The polymers used in this study are called POSS-PEO-POSS(*x*-*y*-*x*) and PEO-POSS(*x*-*y*) where *x* and *y* are the molecular weights of the PEO, M_{PEO}, and POSS, M_{POSS}, blocks in kg mol^{-1} respectively. POSS-PEO-POSS and PEO-POSS structures are shown in Scheme 1. The overall degree of polymerization (N_i) of each block was calculated by

$$N_i = \frac{M_i}{\rho_i v_{ref}} \quad [1]$$

where v_{ref} is fixed at 0.1 nm^3, as described in ref [75]. The overall degree of polymerization was calculated by

$$N = N_{PEO} + N_{POSS}. \quad [2]$$

M_P and M_{EO} are the molar mass of POSS (929.61 g mol^{-1}) and EO monomer units (44.05 g mol^{-1}) respectively; v_{EO} and v_{POSS} are the molar volumes of ethylene oxide monomer units and POSS monomer units calculated using the following equation

$$\nu_i = \frac{M_i}{\rho_i} [3]$$

where M_i and ρ_i are the molar masses of unit i and density of unit i, respectively. $\rho_{PEO} = 1.128$ g cm^{-3} [39] and $\rho_{POSS} = 1.30$ g cm^{-3} at 120 °C. Volume fraction is calculated by

$$f_{EO} = \frac{\nu_{EO}}{\nu_{EO} + \frac{M_{POSS} M_{EO}}{M_P M_{PEO}} \nu_{POSS}}. [4]$$

Table 4.1 shows the polymer characteristics of the three polymers used in this study.

Table 4.1. Characteristics of Polymers in this Study

Polymer	M_{PEO} (kg mol^{-1})	M_{POSS} (kg mol^{-1})	N (120 °C)	f_{EO} (120 °C)
POSS(4)	0	3.72	47	0
POSS-PEO-POSS(2-10-2)	10	3.72	194	0.76
PEO-POSS(5-2)	5	1.86	97	0.76
PEO-POSS(10-4)	10	3.72	194	0.76

M_{PEO} = molecular weight of the PEO block; M_{POSS} = molecular weight of the POSS block determined by H-NMR; N = chain length calculated at 120 °C and monomer reference volume of 0.1 nm^{-1}; f_{EO} = volume fraction of PEO block at 120 °C.

4.2.3. Electrolyte Preparation.

Polymer/salt mixtures were prepared by mixing each polymer with LiTFSI. All mixtures were prepared in an argon glovebox (MBraun) where H_2O and O_2 levels were maintained below 0.5 ppm. POSS-PEO-POSS and PEO-POSS polymers were dried at 90 °C in a glovebox antechamber under vacuum for 48 hours. LiTFSI salt was dried at 120 °C for 72 hours under active vacuum. Dry polymer and dry LiTFSI salt were then dissolved into THF and the solutions were well-mixed at 55 °C for 24 hours. Once dissolved, THF was evaporated at 60 °C for 24 hours. The homogenous polymer/salt mixtures were further dried on a hotplate at 90 °C for 48 hours, then transferred to the glovebox antechamber and additionally dried under vacuum for 72 hours at 90 °C to remove residual solvent. The dry electrolytes color ranged from clear to milky white to pale yellow at room temperature with a solid or waxy consistency. Salt concentrations are calculated by the ratio of lithium to ethylene oxide monomer units (r = [Li] $[EO]^{-1}$).

4.2.4. Differential Scanning Calorimetry.

Samples were hermetically sealed using Tzero aluminum pans and lids in an argon glovebox. Differential scanning calorimetry (DSC) thermograms were obtained by 2 heating and cooling cycles with 20 °C min^{-1} heating rates and 2 °C min^{-1} cooling rates using a Thermal Advantage Q200 calorimeter at the Molecular Foundry, Lawrence Berkeley National Laboratory. The temperature ranged from −90 to 160 °C. Melting and glass transition temperatures were ascertained by analyzing the second heating scan and crystallization transition temperatures was ascertained by analyzing the first cooling scan using TA Thermal Advantage software.

4.2.5. Small and Wide Angle X-ray Scattering.

The morphologies and crystallinity of the electrolytes were determined by small-angle X-ray scattering (SAXS) and wide-angle X-ray scattering (WAXS) respectively. Sample preparation took place inside an argon glovebox. Neat polymers and polymer/salt mixtures were heated to 120 °C, then pressed into 1 mm thick rubber spacers with a 1/8 in. inner-diameter to create a uniform film. The spacers were then sealed inside Kapton windows in custom airtight holders. The samples were annealed at 120 °C under vacuum for at least 48 h. Measurements were performed at beamline 7.3.3. at the Advanced Light Source (ALS) at Lawrence Berkeley National Laboratory and beamline 1–5 at the Stanford Synchrotron Radiation Lightsource (SSRL) at SLAC National Accelerator Laboratory. Using a custom-built heat stage, samples were heated in 20 °C to 60 °C increments, from room temperature up to a maximum of 145 °C, holding temperature at each step for at least 30 minutes, and then cooled in increments between 5°C and 20°C. At the end of each temperature step, SAXS/WAXS measurements were made to establish morphology and confirm thermo-reversibility of phase behavior. Silver behenate was used to determine the beam center and sample-to-detector distance. Two-dimensional scattering patterns were integrated azimuthally using the Nika program for IGOR Pro to produce one-dimensional scattering profiles. [109] Here we report the scattering intensity as a function of the magnitude of the scattering vector, q ($q = 4\pi sin(\theta/2)/\lambda$) where θ is the scattering angle, and λ is the wavelength of the X-rays equal to 1.2398 Å at the ALS and 1.03232 Å at SSRL.

4.3. Results and Discussion

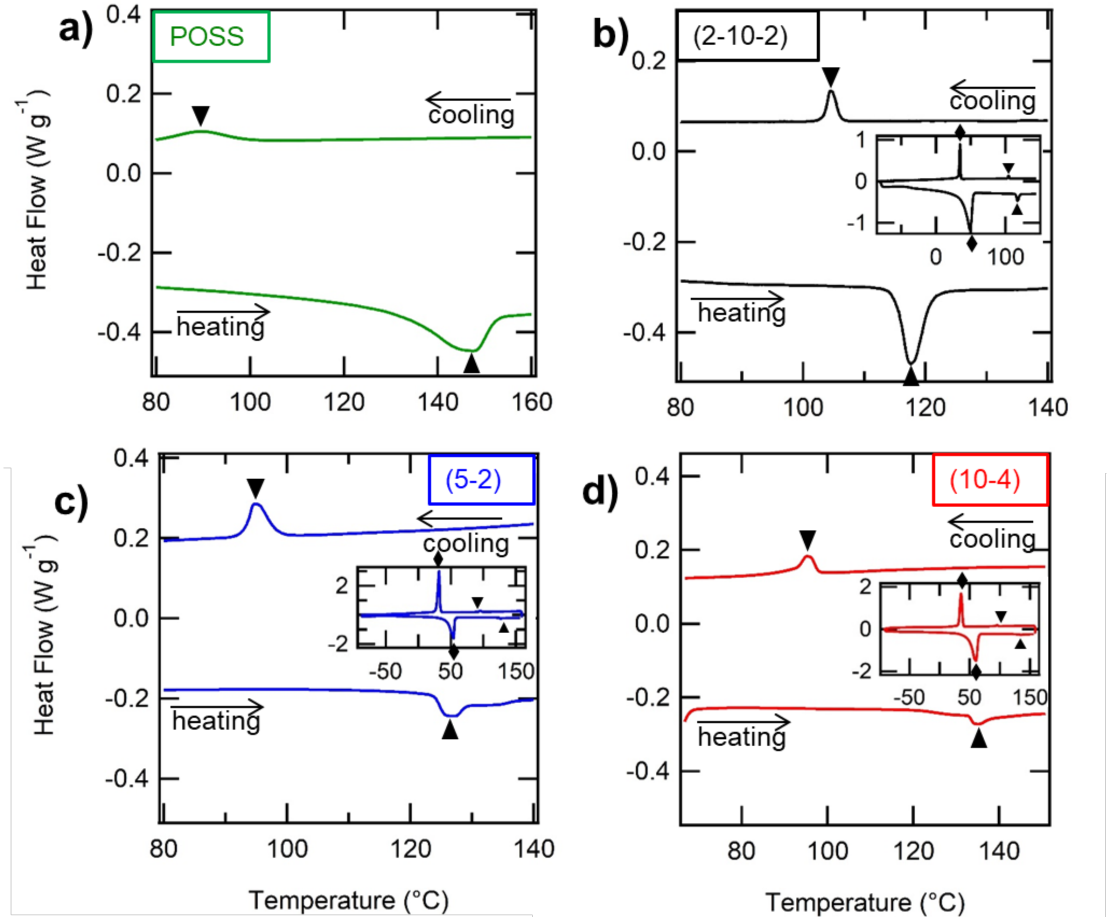

Figure 4.2. DSC thermograms upon cooling and second heating in a) neat POSS homopolymer and copolymers with salt concentration $r = 0.02$ b) POSS-PEO-POSS(2-10-2) c) PEO-POSS(5-2), and d) PEO-POSS(10-4). Insets in b-d show thermograms at larger temperature range.

DSC thermograms of the neat POSS homopolymer is shown in Figure 4.2a. We observe a melting transition at temperature, T_m = 144.4 °C during the heating scan and a crystallization transition at temperature, T_c = 89.5 °C in the cooling scan. In Figures 2b-d, we show typical DSC thermograms of copolymer/salt mixtures in the temperature range $80 \leq T \leq 140$ °C, focusing on the crystallization and melting of the POSS block. Because the POSS blocks are short, we do not expect chain folding of the POSS block in any of the block copolymers. The salt concentration of all three systems is $[Li]\,[EO]^{-1} = r = 0.02$. All three systems exhibit signatures of POSS melting and crystallization. The insets in Figures 2b-d show the thermograms on a wider temperature scale where the closed diamonds reflect the melting and crystallization of PEO domains. In all copolymer/salt mixtures, the DSC peaks associated with the PEO melting and crystallization are much more pronounced than those associated with POSS melting and crystallization.

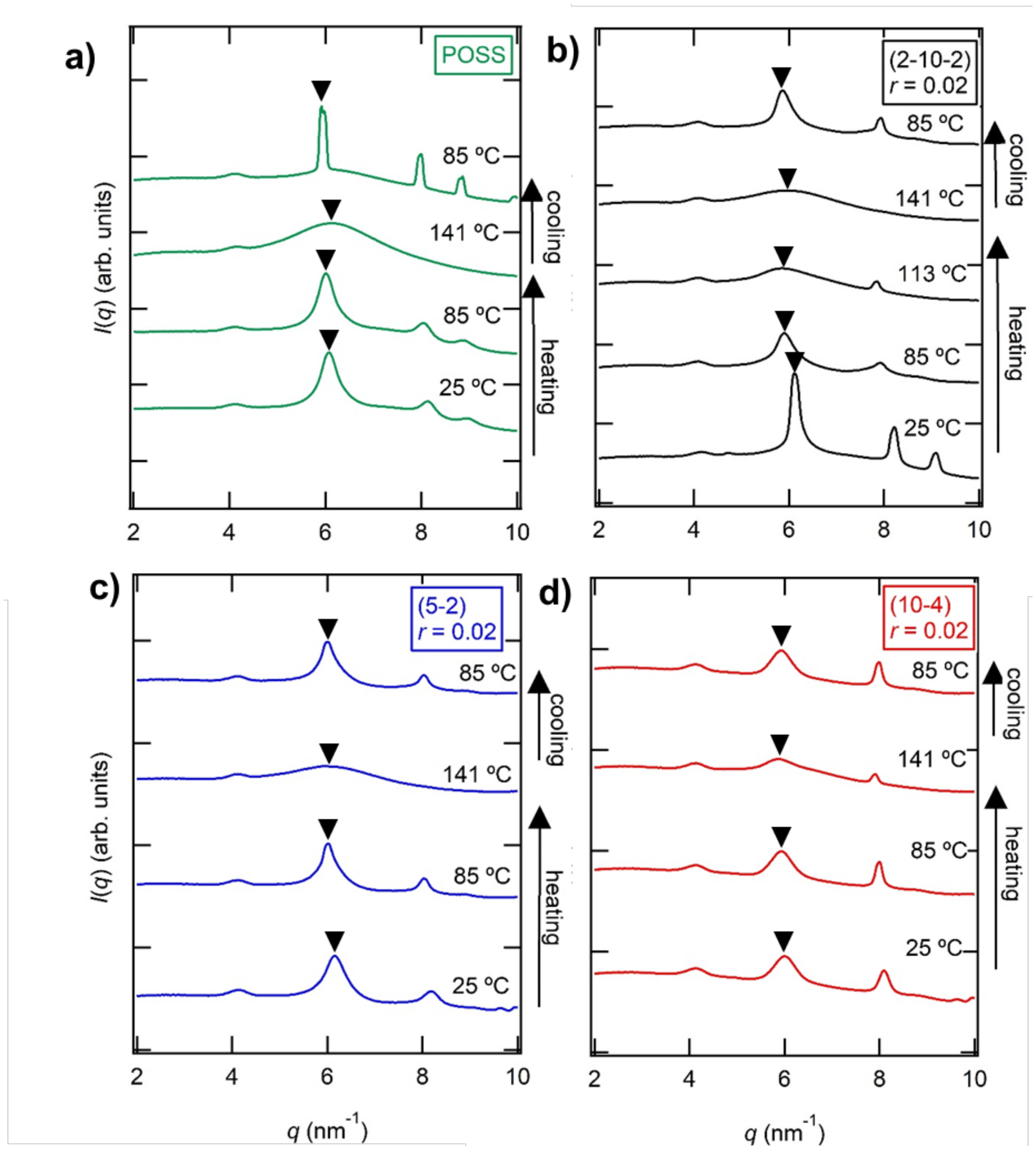

Figure 4.3. WAXS profiles. WAXS intensity is plotted as a function of the magnitude of the scattering vector, q, in a) neat POSS homopolymer as well as copolymer/salt mixtures at $r = 0.02$, b) POSS-PEO-POSS(2-10-2), c) PEO-POSS(5-2), d) PEO-POSS(10-4). Profiles are shifted vertically. Scans are performed upon heating from 25 °C to 141 °C in approximately 60 °C increments, then cooled to 85 ° C, with temperatures indicated on the right. Triangles indicate peaks characteristic of POSS crystallization centered at $q = 5.9 \pm 0.2$ nm^{-1}.

WAXS intensity, $I(q)$, is obtained from POSS homopolymer at selected temperatures, plotted as a function of the magnitude of the scattering vector, q in Figure 4.3a. The sample was heated from room temperature from 25 to 141 °C. The sharp peaks at $q = 5.9$ nm^{-1}, 7.9 nm^{-1}, and 8.9 nm^{-1} observed at 25 °C and 85 °C indicate the presence of the crystalline phase. These peaks give way to an amorphous halo at 141 °C. This scattering pattern indicates the rhombohedral packing of the POSS macromonomer crystal. [110–118] The peak visible at $q = 4.0$ nm^{-1}, is due to the Kapton widows and is apparent in all of the WAXS scans. When the sample is cooled from 141 °C to 85 °C, the crystalline peaks are sharper than those obtained during the heating scan. [115]

WAXS profiles of POSS-PEO-POSS(2-10-2) $r = 0.02$ (Figure 4.3b) at 25 °C reveal three peaks similar to those found in the POSS homopolymer (Figure 4.3a) at $q = 6.1$ nm^{-1}, 8.1 nm^{-1}, and 9.0 nm^{-1}. This indicates that the POSS block packs into a rhombohedral crystal structure as was the case for POSS homopolymer. Heating the sample to 85 °C results in peaks at $q = 5.9$ nm^{-1} and 7.9 nm^{-1}. The relative locations of these peaks are similar to the peaks obtained at 25 °C indicating that the POSS-rich microphase is crystalline at temperatures between 25 and 85 °C. The size of the unit cell at 85 °C is slightly higher than that at 25 °C. Heating the sample further to 113 °C results in significant broadening of the peak at $q = 5.9$ nm^{-1} while the peak at $q = 7.9$ nm^{-1} remains more-or-less unchanged. This suggests that some planes in the POSS crystal structure disorder more readily than others as the melting transition is approached. [98] The scattering profile at 141 °C has one broad scattering peak that we attribute to the molten POSS-rich microphase. When the sample is cooled from 141 °C to 85 °C, the first peak centered at $q = 5.9$ nm^{-1} sharpens, and the second peak at $q = 7.8$ nm^{-1} reappears, signifying POSS recrystallization. The WAXS profile at 85 °C taken upon cooling is qualitatively similar to the profile at 85 °C upon heating, indicating thermoreversibility of the transition.

WAXS profiles of PEO-POSS(5-2) $r = 0.02$ (Figure 4.3c) follow the expected trend: rhombohedral crystals are obtained at 25 °C and 85 °C melt when the sample is heated to 141 °C. WAXS profiles of PEO-POSS(10-4) $r = 0.02$ (Figure 4.3d) also show rhombohedral crystals at 25 °C and 85 °C. However, weak signatures of crystallinity are also obtained at 141 °C.

The scattering patterns in Figure 4.3a-d indicate that the presence of the PEO block does not impede crystallization of the POSS block. [113] Further, the addition of salt does not disrupt the POSS block crystallization.

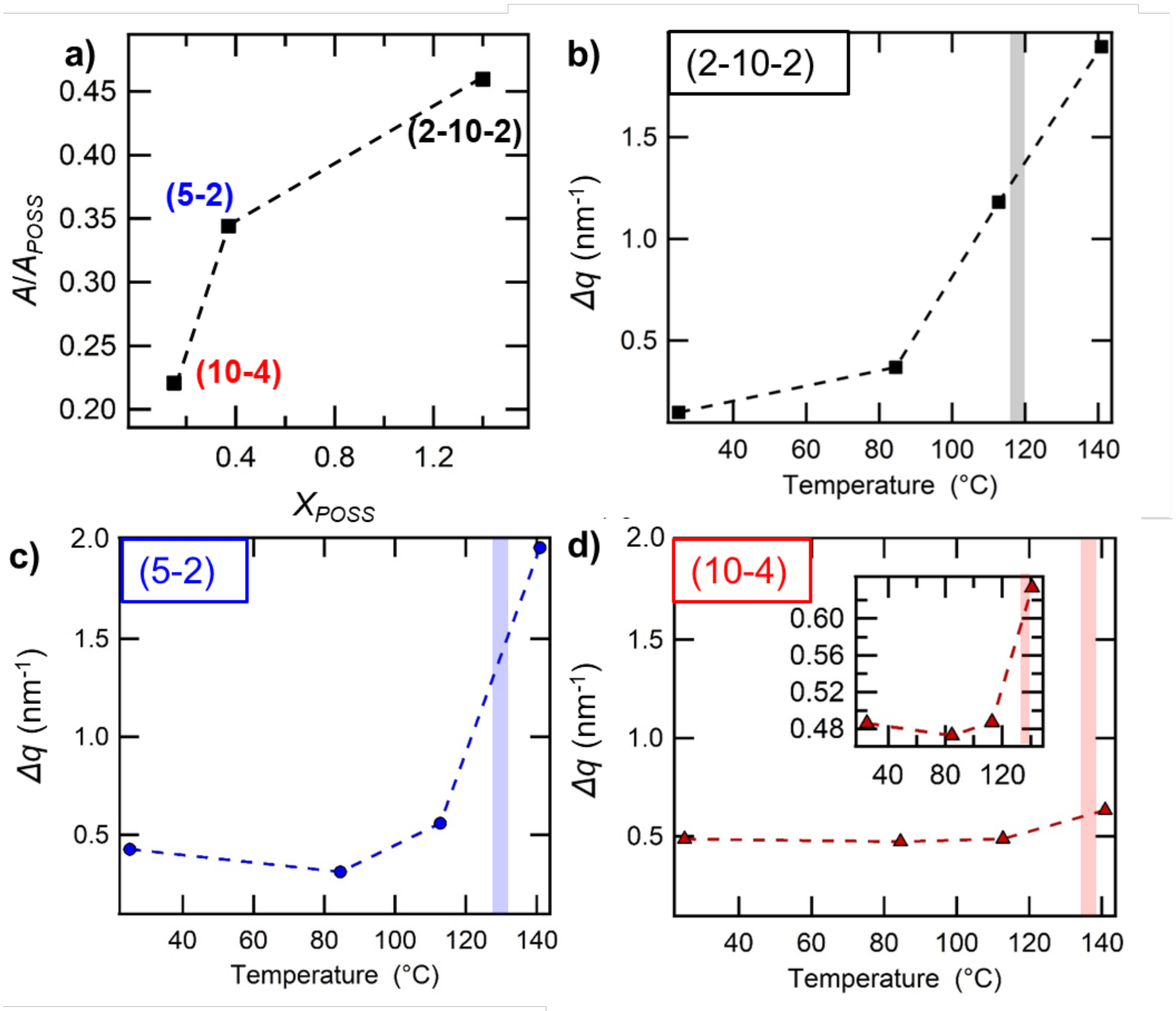

Figure 4.4. Agreement between DSC and WAXS experiments in copolymer/salt mixtures at salt concentration $r = 0.02$. a) WAXS peak area at 85 °C divided by neat POSS homopolymer, A/A_{POSS} centered at $q = 5.9 \pm 0.2$ nm^{-1} versus percent crystallinity of the POSS domain (X_{POSS}). (b-d) Full width at half maximum (Δq) of WAXS peak centered at $q = 5.9 \pm 0.2$ nm^{-1} upon heating from 25 to 141 °C in each copolymer/salt mixture: b) POSS-PEO-POSS(2-10-2), c) PEO-POSS(5-2), and d) PEO-POSS(10-4). The shaded bar represents T_m obtained by DSC experiments.

Figure 4.4a shows the correlation between WAXS and DSC experiments. The x-axis shows the percent crystallinity of the POSS microdomains, X_{POSS}, defined as $X_{POSS} = \Delta H_m w_{POSS}^{-1} \Delta H_{POSS}^{-1}$, where w_{POSS}, the weight fraction of the POSS block, is 0.27 for all copolymers. ΔH_m and ΔH_{POSS} are the POSS domain enthalpy of melting in the copolymer/salt mixture and the POSS homopolymer, respectively. The y-axis is the area under the WAXS peak centered around $q = 5.9 \pm 0.2$ nm^{-1}, A, normalized by the area under the neat POSS homopolymer WAXS peak, A_{POSS}, at 85 °C obtained during the heating scan. Figure 4.4a demonstrates a correlation between A/A_{POSS}

and X_{POSS}. POSS-PEO-POSS(2-10-2) exhibits the highest crystallinity as measured by either the magnitude of A/A_{POSS} or X_{POSS}. Note that X_{POSS} is greater than unity indicating that the POSS-rich microphases in POSS-PEO-POSS(2-10-2) contain less of the amorphous phase than POSS homopolymer.

Figures 4b-d exhibit the full width at half maximum of the WAXS peak at $q = 5.9 \pm 0.2$ nm^{-1}, Δq, versus temperature between $25 < T < 141$ °C in each copolymer/salt mixture shown in Figure 4.3b-d. The broadening of this peak (*i.e.*, increase in Δq) indicates the POSS melting transition. Each figure also shows the POSS block melting transition temperature, T_m, obtained by DSC as a vertical bar. There is good correlation between the WAXS and DSC signatures of melting in Figures 4.4b and c. We note that the peak broadening at the transition is more abrupt in PEO-POSS(5-2) (Figure 4.4c) as compared to POSS-PEO-POSS(2-10-2) (Figure 4.4b).

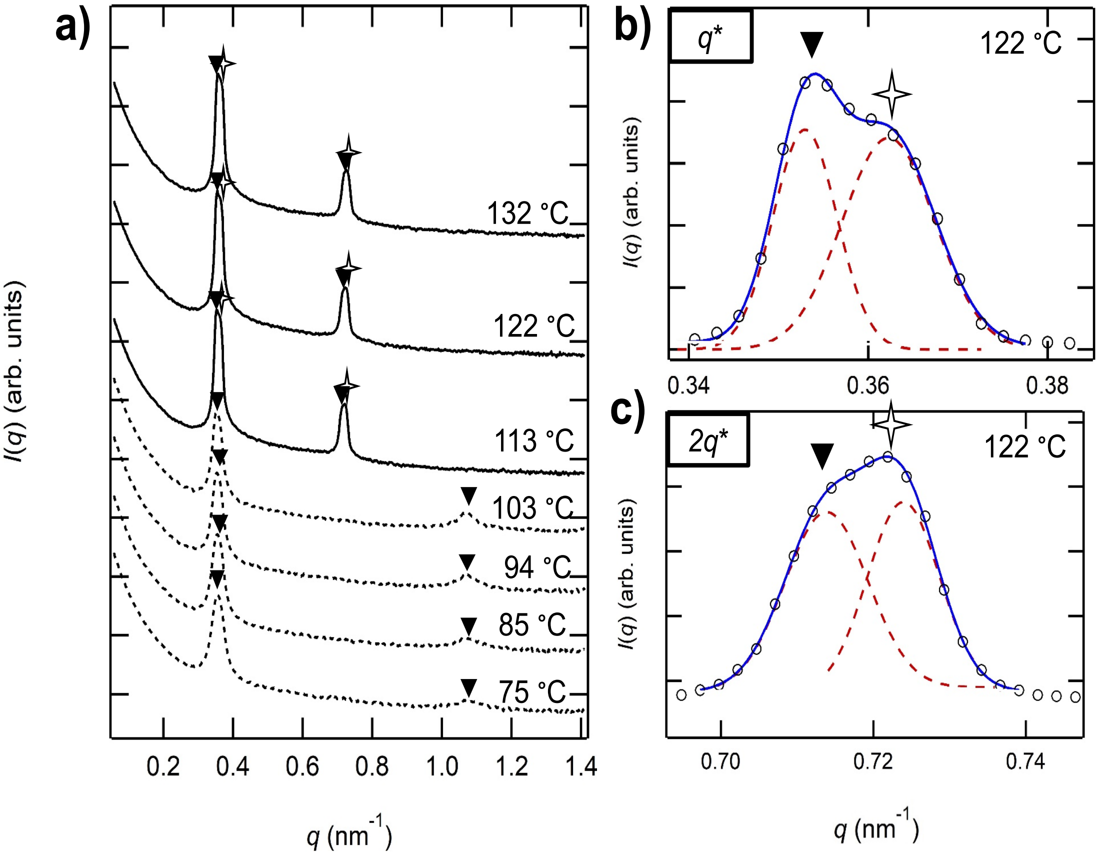

Figure 4.5. SAXS profiles triblock copolymer/salt. a) SAXS intensity is plotted as a function of the magnitude of the scattering vector, q, in POSS-PEO-POSS(2-10-2) at $r = 0.02$. Solid lines indicate amorphous POSS block, dashed lines indicate semicrystalline POSS block. Scans are performed upon cooling from 132 °C to 75 °C in approximately 10 °C increments with temperatures indicated on the right. Expanded peaks at 122 °C are shown in the vicinity of a) $q = q^*$, and b) $q = 2q^*$. ▼and ✧ indicate peaks characteristic of lamellae ($q = q^*$, $2q^*$, $3q^*$) and coexisting lamellae respectively. The data in a) were reported in ref [107].

Figure 4.4d demonstrates that PEO-POSS(10-4) $r = 0.02$ Δq is insensitive to temperature across the temperature range as compared to POSS-PEO-POSS(2-10-2) (Figure 4.4b) and PEO-POSS(5-2) (Figure 4.4c). However, the inset in Figure 4.4d shows that Δq increases slightly from 0.48 nm^{-1} to 0.64 nm^{-1} upon heating from 113 °C to 141 °C. We postulate that the POSS domain is not entirely melted in PEO-POSS(10-4)/salt mixture at 141 °C, though the DSC thermogram indicates $T_m = 134.8$ °C. The disagreement between WAXS and DSC arises because of the lack of a sharp, well-defined melting point for the POSS block. Broad melting transitions are characteristic of semicrystalline block copolymers. [119–121]

In Figure 4.5a, SAXS intensity, $I(q)$, in POSS-PEO-POSS(2-10-2) $r = 0.02$ sample is plotted as a function of q, at selected temperatures upon cooling between 132 °C and 75 °C. The sample shows reversibility of phase transitions upon heating and cooling (heating scans not shown for brevity). Dashed scattering profiles indicate scans taken at $T < T_c$ (*i.e.*, the POSS block is semicrystalline), and solid scattering profiles are scans taken at $T > T_c$ (*i.e.*, the POSS block is amorphous). At 75 °C $\leq T \leq$ 103 °C, the POSS block is semicrystalline and the SAXS pattern reveals two peaks at $q = q^* = 0.35 \pm 0.01$ nm^{-1} and $q = 3q^*$, denoted by triangles, indicating the presence of alternating PEO/salt-rich and POSS-rich lamellae layers (*LAM*). The reason for the suppression of the expected scattering peak at $q = 2q^*$ remains to be established. It is possible that the presence of both amorphous and semicrystalline POSS microdomains are responsible for this observation.

The shapes of the SAXS peaks at temperatures between 113 and 132 °C in Figure 5a are complex. In Figure 4.5b, we show representative background subtracted SAXS profiles in the vicinity of the primary peak on an expanded scale (122 °C). This profile is consistent with the presence of two overlapping peaks. The SAXS data in Figure 4.5b, shown as markers, were fit to a sum of two Lorentzian peaks. The solid curve through the data in Figure 4.5b shows the fit and the two peaks are shown in red underneath the scattering data. We refer to the peak positions as q_1^* and q_2^*. In Figure 4.5c, we show background subtracted 122 °C SAXS profiles in the vicinity of the second order peaks on an expanded scale. This profile also indicates the presence of two overlapping peaks. The triangles and star symbols represent $2q_1^*$ and $2q_2^*$, the expected locations of second order peaks corresponding to the two primary peaks identified in Figure 4.5b. The consistency of the analysis in Figures 4.5b and c indicate the presence of two coexisting lamellar phases (*LAM*/*LAM*) with two different domain spacings: 17.3 nm and 17.8 nm. This coexistence is seen consistently at temperatures above T_c; the peaks obtained at temperatures below T_c are consistent with the presence of a single, conventional lamellar phase. (Some aspects of the morphology of POSS-PEO-POSS(2-10-2) $r = 0.02$ were reported in ref [107]. A detailed analysis of the shapes of the SAXS peaks was not included in ref [107].)

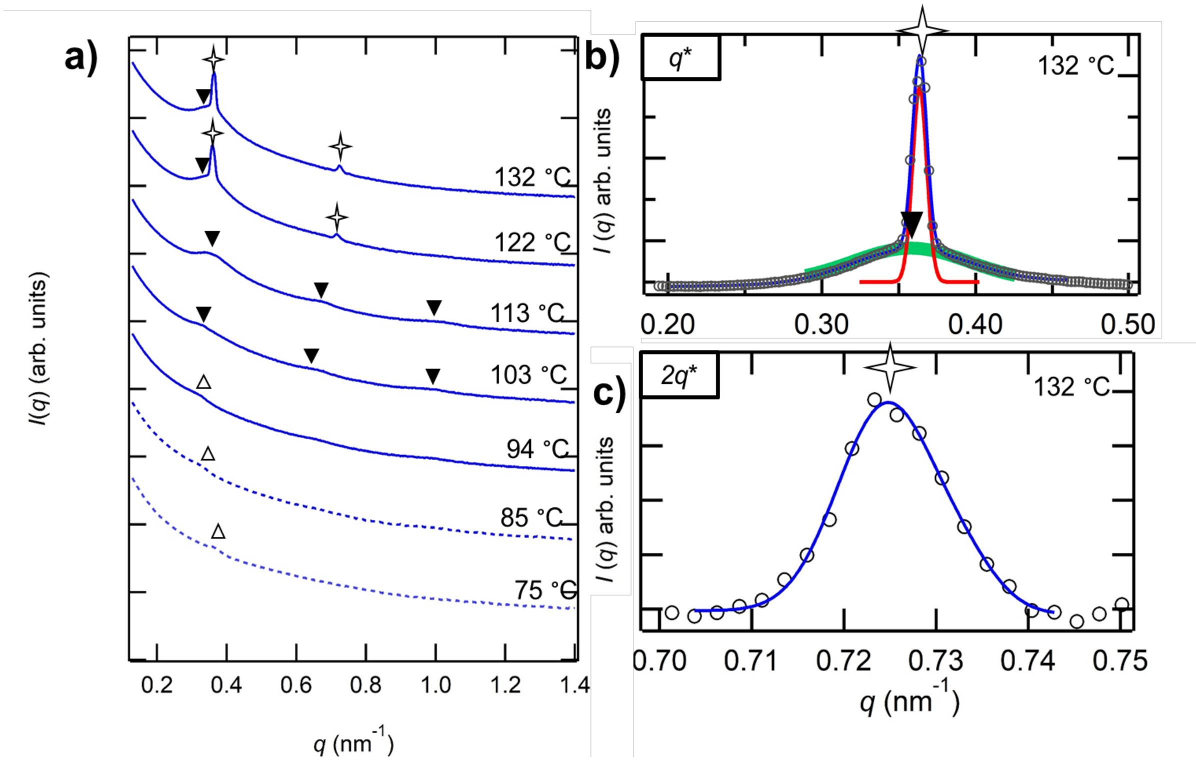

Figure 4.6. SAXS profiles diblock copolymer/salt. a) SAXS intensity is plotted as a function of the magnitude of the scattering vector, *q,* in PEO-POSS(5-2) at *r* = 0.02. Solid lines indicate amorphous POSS block, dashed lines indicate semicrystalline POSS block. Scans are performed upon cooling from 132 °C to 75 °C in approximately 10 °C increments with temperatures indicated on the right. ▼, ✧, and △ indicate peaks characteristic of lamellae ($q = q^*$, $2q^*$, $3q^*$), coexisting lamellae, and disorder ($q = q^*$). Peaks in the vicinity of $q = q^*$ and $2q^*$ are expanded in b) and c) at 132 °C. The data in a) were reported in ref [108].

PEO-POSS(5-2) $r = 0.02$ SAXS scans are shown in Figure 4.6a . Dashed scattering profiles indicate scans taken at $T < T_c$ (*i.e.*, the POSS block is semicrystalline), and solid scattering profiles are scans taken at $T > T_c$ (*i.e.*, the POSS block is amorphous). The scattering profiles below 94 °C exhibit a single, broad peak at $q = q^*$, a standard signature of a disordered phase (*DIS*). [68,122] However, the POSS-rich concentration fluctuations are semicrystalline, and this may complicate interpretation of the scattering profiles. We address this point shortly. The emergence of two higher order peaks at $q = 2q^*$ and $q = 3q^*$ in the SAXS profiles at 103 °C indicate a *DIS* to *LAM* transition at $T = 98.5 \pm 5$ °C. The transition temperature is in good agreement with T_c determined by DSC (95 °C).

The scattering profiles at 122 °C and 132 °C exhibit a sharp peak superposed on the broad lamellar peak at $q = q^*$ seen in the scans taken at temperatures between 103 °C < T < 113 °C. The background subtracted SAXS profiles in the vicinity of the primary peak on an expanded scale at 132 °C are shown in Figure 4.6b. SAXS data in Figure 4.6b, shown as markers, were fit to a sum of 1 Lorentzian peak, indicated in dashed red, and 1 Gaussian peak, indicated in solid green. The solid blue curve through the scattering data in Figure 4.5b shows the fit. The overlapping peaks indicate the presence of one weakly ordered lamellar phase coexisting with a well-ordered lamellar phase, *LAM*/*LAM,* with two different domain spacings: 17.6 nm and 17.3 nm respectively. Figure 6c shows the scattering data in the vicinity of $q = 2q^*$ at 132 °C. The data is fit to one Gaussian peak, shown as a blue curve. We postulate that the well-ordered *LAM* peak suppresses the weak, broad lamellar peak seen between 103 °C < T < 113 °C. Unlike the sample in Figure 4.5a-c, the sample in Figure 4.6a-c undergoes a *LAM* to *LAM*/*LAM* at a temperature 33 °C above T_c.

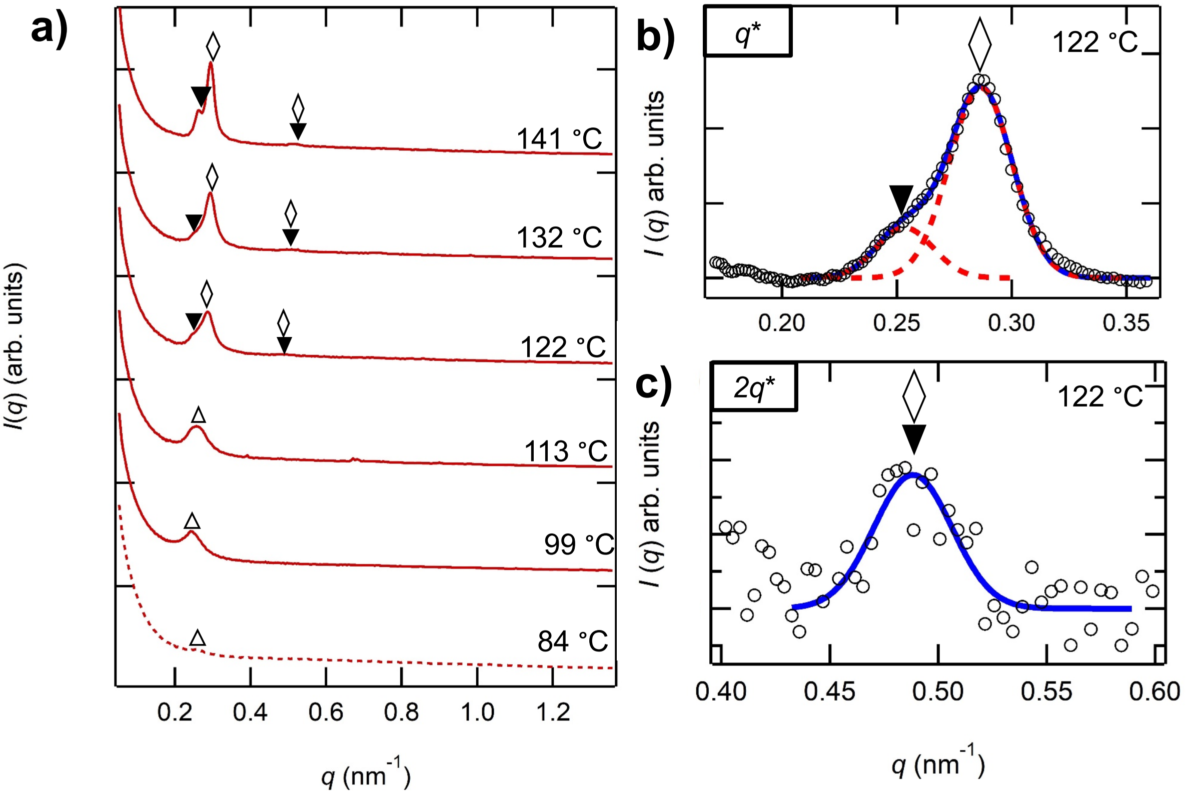

Figure 4.7. SAXS profiles larger diblock copolymer/salt. a) SAXS intensity is plotted as a function of the magnitude of the scattering vector, *q,* in PEO-POSS(10-4) r = 0.02. Solid lines indicate amorphous POSS block, dashed lines indicate semicrystalline POSS block. Scans are performed upon cooling from 141 °C to 84 °C in approximately 10 °C increments with temperatures indicated on the right. ▼, △, and ◊, indicate peaks characteristic of lamellae ($q = q^*$, $2q^*$, $3q^*$), disorder ($q = q^*$), and hexagonally packed cylinders ($q = q^*$, $\sqrt{3}q^*$, $2q^*$). Peaks in the vicinity of $q = q^*$ and $2q^*$ are expanded in b) and c) at 122 °C.

PEO-POSS(10-4) r = 0.02 SAXS profiles in Figure 4.7a indicate a single Gaussian peak at $q = q^*$ at 84 °C ≤ T ≤ 113 °C, a signature of *DIS.* This peak appears more well-defined than the

DIS PEO-POSS(5-2) sample (Figure 4.6a). At 122 °C, we see the emergence of overlapping peaks in the vicinity of $q = q^*$. The first, small peak is apparent at $q = 0.25$ nm^{-1}, and the second, more well-defined peak is centered around $q = 0.28$ nm^{-1}. We call these peaks $q_{,1}^*$ and $q_{,2}^*$, respectively, and are shown in Figure 4.7b. In order to discern the morphology of this sample, the SAXS data between $q = 0.4$ and 0.6 nm^{-1} is shown in Figure 4.7c. A single, Gaussian peak is fit to the data, centered at $q = 0.49$ nm^{-1}. The location of the second peak is $2q_1^*$ and is also equal to $\sqrt{3}q_2^*$. We therefore conclude that the peaks seen at $q = q_{,1}^*$ and $2q_{,1}^*$ is indicative of a *LAM* phase, while the peaks at $q_{,2}^*$ and $\sqrt{3}q_{2*}$ indicate a coexisting hexagonally packed cylinders phase (*CYL*). Thus, this sample transitions from *DIS* to coexisting *LAM*/*CYL* at 117.5 ± 4.5 °C. These coexisting phases are evident in the window 122 °C $\leq T \leq$ 141 °C. In a previous study, we have established *LAM*/*CYL* coexistence in PEO-POSS(5-2) $r = 0.08$ wherein the SAXS data were augmented by electron tomography. [108]

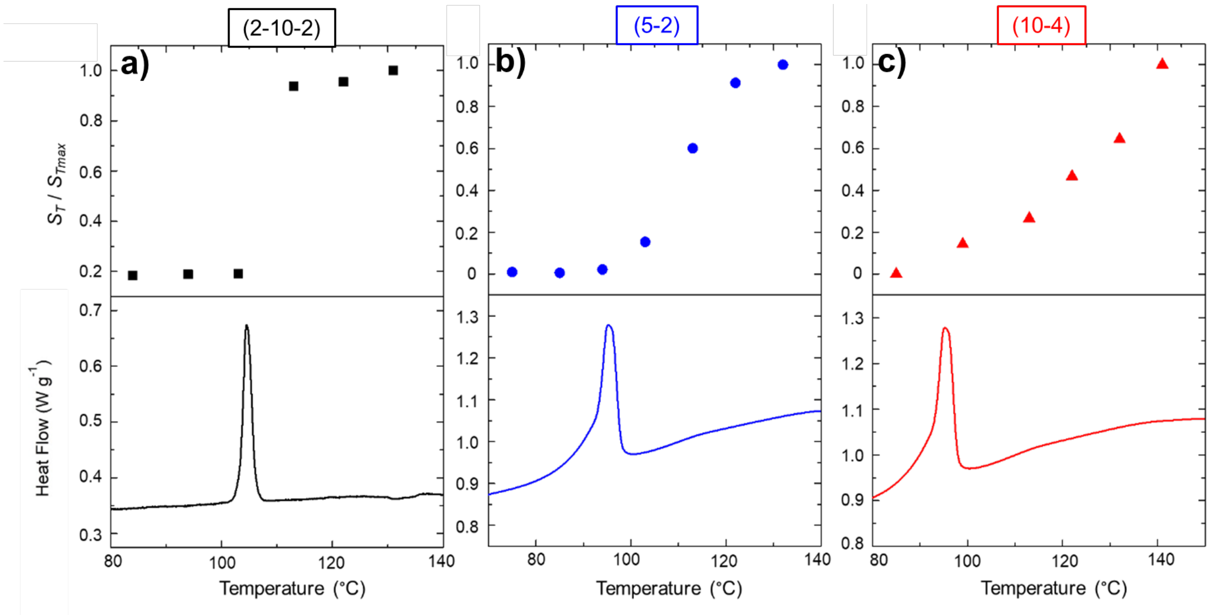

Figure 4.8. SAXS invariant and DSC. Invariant of SAXS peaks at $q = q^*$ normalized by invariant at highest temperature, S_T/S_{Tmax}, versus temperature (top) and DSC cooling thermogram (bottom) at $r = 0.02$ in a) POSS-PEO-POSS(2-10-2), b) PEO-POSS(5-2), c) PEO-POSS(10-4).

Figure 4.8a-c shows SAXS data in the form of S_T / S_{Tmax} versus temperature alongside DSC thermograms upon cooling, where S_T is invariant at $q = q^*$ of the SAXS profile calculated at temperature, T, and S_{Tmax} is the invariant at the highest temperature where the SAXS profiles were recorded (132 °C for POSS-PEO-POSS(2-10-2) and PEO-POSS(5-2); 141 °C for PEO-POSS(10-4) $r = 0.02$ samples). S_T is calculated as follows:

$$S = \int_{q1}^{q2} Iq^2 dq \text{ [5].}$$

The top panel in Figure 4.8 shows the temperature dependence of S_T/S_{Tmax}, quantifying the qualitative changes in the SAXS profiles as a function of temperature (r = 0.02). In all cases, S_T/S_{Tmax} increases with increasing temperature indicating the thermodynamic driving force for order formation increases with increasing temperature. This is opposite of what is typically observed in conventional block copolymers. [123] The bottom panel in Figure 4.8 shows the DSC cooling data over the same temperature window. The increase in S_T/S_{Tmax} coincides with the melting of the POSS domain. In the case of POSS-PEO-POSS(2-10-2), the increase in S_T/S_{Tmax} is discontinuous at T_c. A more gradual increase is seen in the case of PEO-POSS(5-2) as temperatures increase above T_c. An even more gradual increase is seen in the case of PEO-POSS(10-4).

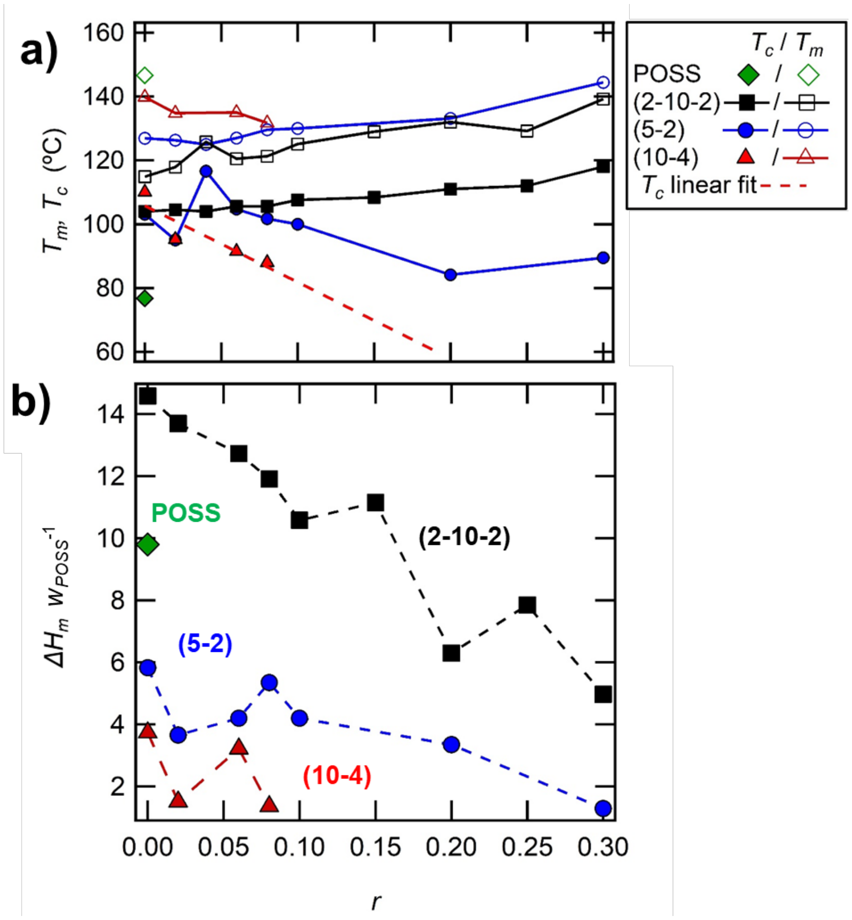

Figure 4.9. Summary of all DSC experiments in neat POSS and POSS-PEO-POSS(2-10-2), PEO-POSS(5-2), and PEO-POSS(10-4)/salt mixtures. a) POSS block T_m and T_c b) $\Delta H_m w_{POSS}^{-1}$ as a function of salt concentration, r.

Our discussion thus far has only included samples at salt concentration $r = 0.02$. We now expand our DSC analysis to the copolymers without salt and higher salt concentrations to understand the effect of r on the crystallization of the POSS block in all copolymer/salt mixtures. Figure 4.9a shows the POSS block T_m and T_c versus r for all three copolymer systems and neat POSS homopolymer. We note the T_m is greatest and T_c is lowest in the POSS homopolymer as compared to all neat copolymers and copolymer/salt mixtures. The T_m result is not surprising as it indicates that the melting of POSS crystals is facilitated by microphase separation. The T_c result is a little more interesting, as it indicates that nucleation of POSS crystals is facilitated by microphase separation. In the POSS-PEO-POSS(2-10-2) system, T_m and T_c both slightly increase with increasing salt concentration. Similarly, PEO-POSS(5-2) samples T_c increases slightly, while T_m decreases slightly over the experimental salt concentration range. For these two systems, T_m, and T_c are relatively weak functions of salt concentration. On the other hand, in the PEO-POSS(10-4) samples, T_m and T_c both decrease substantially in the salt concentration range between $0 \leq r \leq 0.08$. At $r > 0.08$, the POSS block is completely amorphous (*i.e.* no melting or crystallization transitions are discernable in the DSC thermograms). The dashed line through T_c is the linear fit through the data and will be used in subsequent analysis to estimate T_c in PEO-POSS(10-4)/salt mixtures at $r > 0.08$. These results suggest that salt ions do not interact exclusively with PEO chains. (We did try to dissolve LiTFSI in POSS homopolymer but found that the two materials were immiscible.)

Figure 4.9b shows the enthalpy of POSS block melting normalized by weight percent of POSS, $\Delta H_m w_{POSS}^{-1}$ as a function of *r.* All three copolymer/salt mixtures exhibit a decrease in $\Delta H_m w_{POSS}^{-1}$ with increasing *r*, indicating weaker POSS block crystallization at higher salt concentrations. Surprisingly, the POSS block in the POSS-PEO-POSS(2-10-2) system appears more strongly crystalline than neat POSS homopolymer over a large range of salt concentrations, $0 \leq r \leq 0.15$. Above $r = 0.15$, $\Delta H_m w_{POSS}^{-1}$ of POSS-PEO-POSS(2-10-2)/salt mixtures decreases below that of the neat POSS homopolymer. At all salt concentrations, the triblock copolymer/salt mixtures exhibit stronger POSS crystallinity than both diblock copolymer/salt mixtures. PEO-POSS(10-4)/salt mixtures exhibits the weakest POSS block crystallinity of all three copolymers up to $r = 0.08$ (above this salt concentration, the POSS block is amorphous).

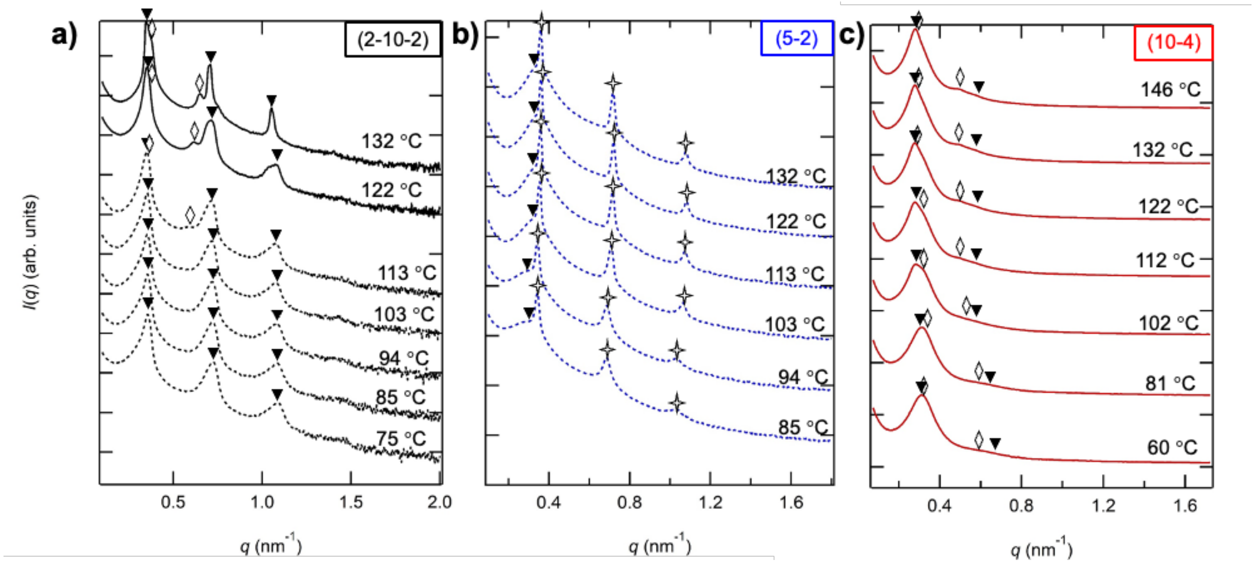

Figure 4.10. SAXS scattering profiles of copolymers at $r = 0.20$ and $60\ °\mathrm{C} \le T \le 146\ °\mathrm{C}$ in a) POSS-PEO-POSS(2-10-2), b) PEO-POSS(5-2), and c) PEO-POSS(10-4). Profiles are shifted vertically. Solid lines indicate amorphous POSS block, dashed lines indicate samples containing a semicrystalline POSS block. Temperatures are indicated on the right. ▼, ✧, and ◊ indicate peaks characteristic of lamellae ($q = q^*, 2q^*, 3q$), coexisting lamellae, and hexagonally packed cylinders ($q = q^*, \sqrt{3}q^*, 2q^*$).

Figure 4.10a shows SAXS profiles of POSS-PEO-POSS(2-10-2) $r = 0.20$ at a temperature range $75\ °\mathrm{C} \le T \le 132\ °\mathrm{C}$, obtained during cooling. The dashed lines indicate SAXS profiles wherein the POSS block in the sample is semicrystalline (i.e. $T < T_c$) in the temperature regime $75\ °\mathrm{C} \le T \le 113\ °\mathrm{C}$. The SAXS profiles show clear peaks at $q = q^*$, $2q^*$, and $3q^*$, indicative of well-ordered *LAM*, denoted by filled triangles. The solid line SAXS profiles indicate measurements wherein the POSS block is amorphous (*i.e.*, $T > T_c$) between $122\ °\mathrm{C} \le T \le 132\ °\mathrm{C}$. At 112 °C, we see the emergence of a second primary peak at $q = q_{,2}^*$. Additionally, a broad peak appears at $q = \sqrt{3}q_{,2}^*$, a signature of *CYL* phase coexisting with the *LAM*. In the profiles at 122 °C and 132 °C, the peaks representative of *LAM* as well as the peaks representative of *CYL* sharpen and grow with intensity. Figure 4.10a shows the POSS-PEO-POSS(2-10-2) $r = 0.20$ sample undergoes an order-order transition from *LAM* to *LAM*/*CYL* upon heating at 117.5 ± 4.5 °C, coinciding with T_c measured by DSC.

Figure 4.10b shows SAXS profiles of PEO-POSS(5-2) at the same salt concentration as Figure 4.10a ($r = 0.20$) at a temperature range $85\ °\mathrm{C} \le T \le 132\ °\mathrm{C}$, obtained during a cooling run. The highest temperature is below the melting temperature of the POSS block ($T_m = 133.1$ °C). Thus, the POSS block is semicrystalline throughout the accessible temperature regime. We see *LAM* characteristic peaks in all profiles (*i.e.* peaks centered at $q = q^*$, $2q^*$), denoted by triangles. The peaks grow in intensity and sharpen with increasing temperature. However, in all measurements, we note the appearance of a broad, Gaussian peak coexisting with the ordered *LAM* peaks. These SAXS peaks are qualitatively similar to those obtained at $r = 0.02$ (Figure 4.6a). We thus posit the presence of two coexisting *LAM* phases (*LAM*/*LAM*).

Figure 4.10c shows SAXS data for PEO-POSS(10-4) $r = 0.20$ at a temperatures 60 °C $\leq T \leq$ 146 °C (the POSS block is amorphous at this salt concentration in this sample). We see *LAM* characteristic peaks in all profiles (*i.e.* peaks centered at $q = q^*$ and $2q^*$) as well as coexisting *CYL* characteristic peaks (*i.e.* peaks centered at $q = q_{,2}^*$ and $\sqrt{3}q_{,2}^*$). Thus, this sample contains an ordered phase of *LAM*/*CYL* with two different domain spacings, similar to POSS-PEO-POSS(2-10-2)/salt mixture (Figure 7a) at 122 °C $\leq T \leq$ 132 °C.

Figure 4.10 demonstrates that only *LAM* are seen in crystalline samples (dashed curves in Figure 10) as predicted by Whitmore and Noolandi. [95] Curved interfaces are only seen in samples above T_c as might be expected of asymmetric copolymer/salt mixtures ($0.76 \leq f_{EO/LiTFSI} \leq 0.85$). However, *CYL* always coexist with *LAM* despite the fact the PEO and POSS blocks are both amorphous.

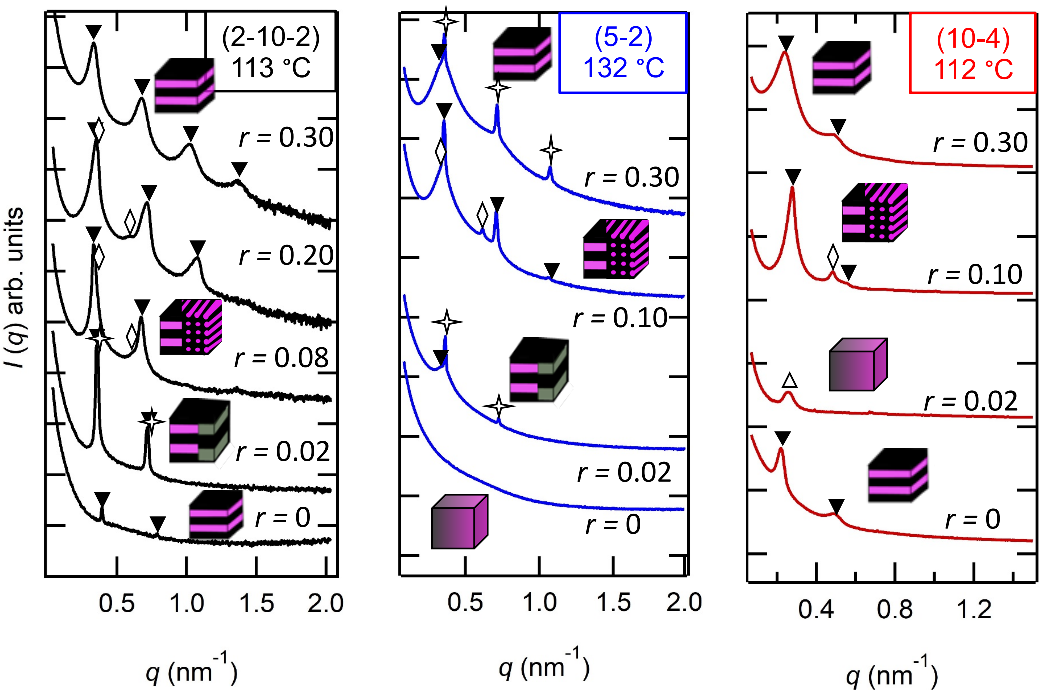

Figure 4.11. SAXS scattering profiles of copolymer/salt mixtures at constant temperature and varied salt concentration, $0 \leq r \leq 0.30$. a) POSS-PEO-POSS(2-10-2), b) PEO-POSS(5-2), and c) PEO-POSS(10-4). Profiles are shifted vertically. Salt concentration are indicated on the right. ▼, ✧, and ◊ indicate peaks characteristic of lamellae ($q = q^*$, $2q^*$, $3q$), coexisting lamellae, and hexagonally packed cylinders ($q = q^*$, $\sqrt{3}q^*$, $2q^*$).

The effect of added salt on the morphology is shown in Figure 4.11a-c, where SAXS data is shown in each system at varied salt concentrations but at constant temperature. Figure 11a shows data for the POSS-PEO-POSS(2-10-2)/salt mixtures at 132 °C. All samples are ordered at this temperature. In the neat sample (r = 0), a *LAM* phase is obtained. At r = 0.02, *LAM/LAM* coexistence is obtained, and the peaks are much sharper than the neat sample. Increasing the salt concentration to r = 0.08 results in the emergence of additional scattering peaks at $q = q_{,2}*$ and $\sqrt{3}q_{,2}*$ that are superimposed on the scattering profile of the lamellar phase, standard signatures of *CYL*. Increasing salt concentration further to r = 0.20 results in the sharpening and increased intensity of both the *LAM* and *CYL* peaks. Finally, the highest salt concentration r = 0.30 results in *LAM*.

PEO-POSS(5-2)/salt mixtures at 132 °C are shown in Figure 4.11b. The neat sample is *DIS*, while all salt containing samples are ordered. At low salt concentration, r = 0.02 the profile indicates *LAM/LAM*. Increasing the salt concentration to r = 0.10 results in *LAM*/*CYL* coexistence. Increasing salt concentration further to r = 0.30 results in *LAM*/*LAM* coexistence.

PEO-POSS(10-4)/salt mixtures at 112 °C are shown in Figure 4.11c. The neat sample is *LAM* while the r = 0.02 is *DIS*. Increasing the salt concentration to r = 0.10 results in *LAM*/*CYL*. Increasing salt concentration further to r = 0.30 results in a *LAM* phase as seen in POSS-PEO-POSS(2-10-2) r = 0.30.

Figure 4.12 summarizes the morphology of the block copolymer electrolytes and the semicrystalline properties of the POSS-rich microphase in the temperature range 70 °C $\leq T \leq$ 140 °C and salt concentration range $0 \leq r \leq 0.30$. The different morphologies, *LAM*, *DIS*, *LAM*/*CYL*, and *LAM*/*LAM* are shaded in gray, yellow, and hatched green and hatched gray regions respectively. T_m (triangles) and T_c (squares) are plotted on top of the morphology data. The colors of T_m and T_c markers indicate the magnitude of $\Delta H_m w_{POSS}^{-1}$, as indicated by the accompanying color scale.

The POSS-PEO-POSS(2-10-2) system (Figure 4.12a) is ordered at all temperatures and salt concentrations. The neat polymer is *LAM* throughout the accessible temperature window (both above and below T_c). The addition of salt results in the emergence of a wide *LAM*/*LAM* window at high temperature. The rest of the phase diagram is dominated by *LAM* morphology with a wide window of *LAM*/*CYL* above T_c. Phase transitions occur close to T_c in all salt-containing samples. It is evident that phase coexistence is not an intrinsic property of the copolymer but is induced by the addition of salt.

In the POSS-PEO-POSS(5-2) system (Figure 4.12b), small pockets of *DIS* appear. A *LAM* to *DIS* transition upon heating is seen in the neat block copolymer above T_c. A *DIS* phase is seen at r = 0.02 that form *LAM* upon heating. At higher temperatures, a coexisting phase of *LAM*/*LAM* appears. *LAM/LAM* is seen over a wide window giving way to *LAM*/*CYL* coexistence at intermediate salt concentrations and high temperatures above T_c. At r = 0.20 and 0.30, the *LAM*/*LAM* phase dominates. We note that all SAXS scans at these salt concentrations were performed at temperatures below the melting transition (*i.e.*, $T < T_m$). We also note that in phase coexistence is only seen in the salt-containing systems in POSS-PEO-POSS(5-2).

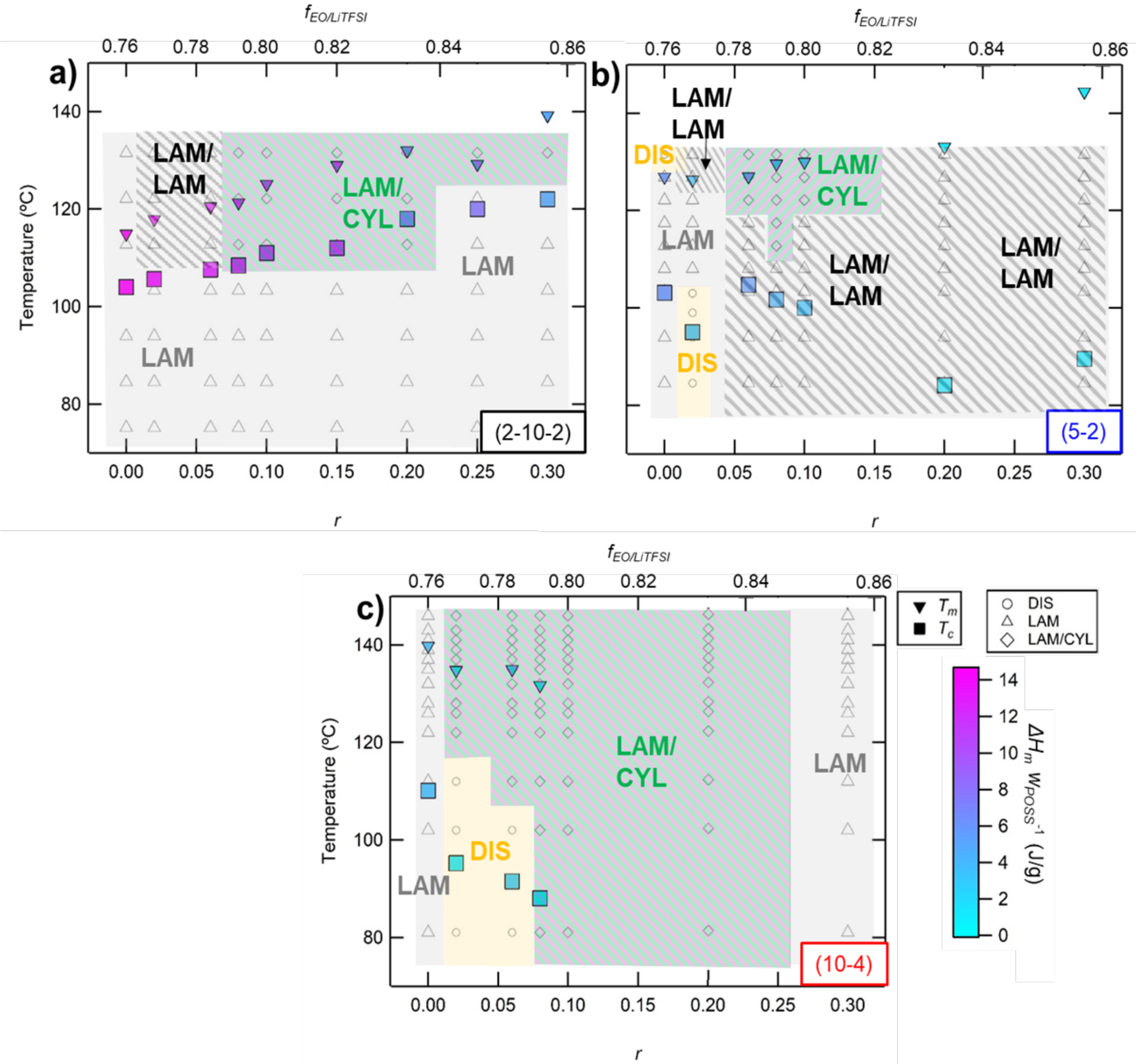

Figure 4.12. Phase diagrams of a) POSS-PEO-POSS(2-10-2), b) PEO-POSS(5-2), and c) PEO-POSS(10-4)/ salt mixtures summarizing morphology data determined by SAXS as a function salt concentration, *r*, and temperature upon cooling. The top axis is the EO/LiTFSI volume fraction, $f_{EO/LiTFSI}$. The green hatched, gray, gray hatched, and yellow regions represent lamellae/hexagonally packed cylinders (*LAM/CYL*), lamellar (*LAM*), coexisting lamellar (*LAM*/*LAM*), and disordered (*DIS*) morphologies respectively. Melting (triangles) and crystallization (square) temperatures (T_m, T_c) are shown with color scale representing normalized enthalpy of melting, $\Delta H_m w_{POSS}^{-1}$.

In the PEO-POSS(10-4) system (Figure 4.12c), the neat polymer does not exhibit any transition and is *LAM* throughout the accessible temperature window. The addition of salt results in the stabilization of a wider *DIS* window than in PEO-POSS(5-2) system at low salt concentration and temperature. The rest of the phase diagram is ordered *LAM*/*CYL* and *LAM* at highest salt concentration (r = 0.30). Note that we only observe thermally driven phase transitions in copolymer/salt mixtures wherein the POSS block undergoes crystalline to amorphous transition with the exception of $r = 0.08$, which lies at the border between the two regimes.

Figure 4.12 demonstrates that POSS crystallization drives thermally driven phase transitions in all 3 systems. Phase transitions occur most closely to T_c in systems exhibiting greater $\Delta H_m w_{POSS}^{-1}$ (*i.e.*, T_c markers shown in pink) versus those with weaker POSS crystallinity (*i.e.*, T_c markers shown in blue).

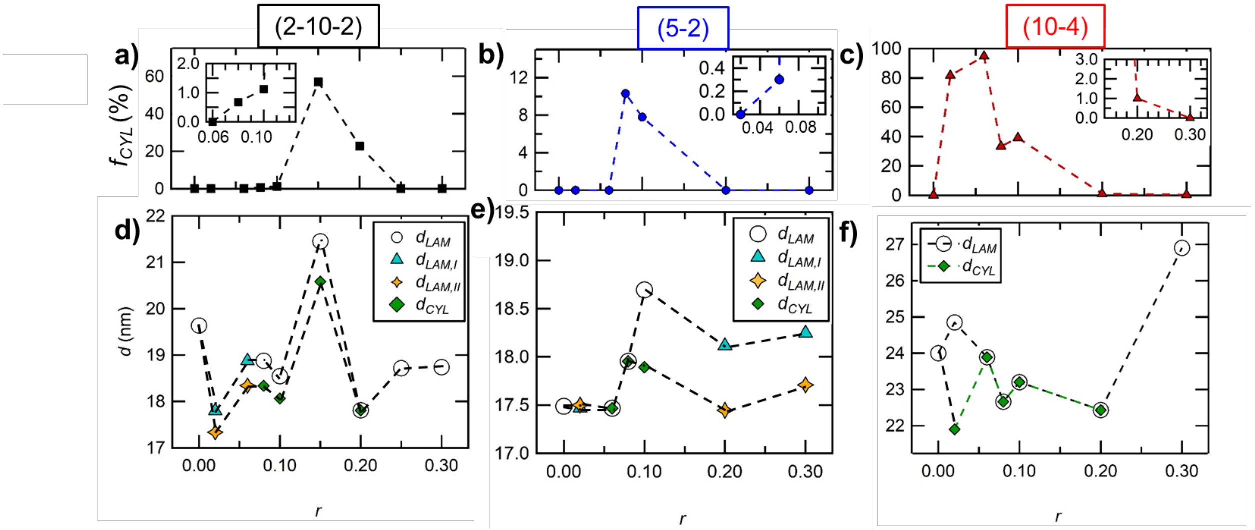

Figure 4.13. Fraction cylinders (f_{CYL}) and domain spacing, d, of lamellae (d_{LAM}), hexagonally packed cylinders (d_{CYL}), and coexisting lamellae ($d_{LAM,I}$, $d_{LAM,II}$), versus salt concentration, r, at 122 °C in a,d) POSS-PEO-POSS (2-10-2) b,e) PEO-POSS(5-2) and c,f) PEO-POSS(10-4).

At 122 °C, all three systems exhibit *LAM*/*CYL* coexistence windows at intermediate salt concentrations. This is quantified in Figure 13 where we estimate the fraction of *CYL* grains, f_{CYL}, as follows,

$$f_{CYL} = \frac{S_{\sqrt{3}q*}}{S_{\sqrt{3}q*} + S_{2q*}} [6],$$

where $S_{\sqrt{3}q*}$ is the SAXS invariant centered around $q = \sqrt{3}q*$, and S_{2q*} is the SAXS invariant centered around $q = 2q*$. f_{CYL} versus salt concentration is plotted in Figure 13a-c. Each plot shows a clear maximum in f_{CYL} near the middle of the *LAM*/*CYL* coexistence window shown in Figure 12a-c. While POSS-PEO-POSS(2-10-2)/salt exhibits a clear maximum in f_{CYL} at $r = 0.15$, both diblock copolymers exhibits peak f_{CYL} at $r = 0.08$. The relative amount of f_{CYL} is almost 95% at the maximum in PEO-POSS(10-4), which contains the largest *LAM*/*CYL* window. f_{CYL} is 60% at the maximum in POSS-PEO-POSS(2-10-2), which contains the second largest *LAM*/*CYL* window, and only 11% in PEO-POSS(5-2), which has the smallest *LAM*/*CYL* coexistence window.

Figure 4.13d-f show the domain spacing, d of ordered morphologies, d_{LAM} and d_{CYL} at 122 °C, as a function of r. The variables $d_{LAM,I}$ and $d_{LAM,II}$ are assigned as the domain spacings of coexisting lamellae.

The d_{LAM} in neat POSS-PEO-POSS(2-10-2) is 19.8 nm. A large decrease in d is observed with the addition of a small amount of salt ($r = 0.02$); the two coexisting *LAM* phases have domains spacings of 17.3 nm and 17.8 nm. The d in the presence of salt is affected by two competing effects: increased segregation between the blocks will increase d while the specific solvation motif on PEO chains around Li^+ ions will cause a decrease in d. [124] The observed decrease suggests that solvation effects dominate despite of the low salt concentration. d increases rapidly with increasing salt, reaching a maximum of 21.5 nm at $r = 0.15$. This is the salt concentration at which f_{CYL} also exhibits a maximum; compare Figures 13a and d. The sizes of the coexisting phases in POSS-PEO-POSS(2-10-2)/salt mixtures, appear to be codependent and within 1 nm between $0.02 \leq r \leq 0.20$ At $r = 0.20$, $d_{LAM} = d_{CYL}$, and at high salt concentrations (*i.e.,* $r > 0.20$), coexisting phases give way to a pure *LAM* phase.

The d of neat PEO-POSS(5-2) is smaller than that of neat POSS-PEO-POSS(2-10-2), as expected (Figure 4.13e). The effect of added salt on d is less dramatic in PEO-POSS(5-2). However, many of the features observed in Figures 13e are qualitatively similar to Figure 4.13d. The d of coexisting phases are codependent and the peak in d_{LAM} occurs at $r = 0.10$, while the peak in d_{CYL} occurs at $r = 0.08$ (the same salt concentration at which a peak in f_{CYL} is observed (Figure 4.13b)).

The d of neat PEO-POSS(10-4) is a factor of 1.4 larger than that of PEO-POSS(5-2), as expected from systems in the weak segregation limit (d is proportional to the square root of chain length). The addition of a small amount of salt ($r = 0.02$) leads to coexistence where d_{CYL} is more than 3 nm greater than d_{LAM}. At this salt concentration, it appears that the consequence of increased segregation is apparent in the cylinder phase while the consequence of ion solvation is apparent in the lamellar phase. At all other salt concentrations where coexistence is observed ($0.02 \leq r \leq 0.20$), the d of coexisting phases are codependent and indistinguishable. The domain spacing of the pure *LAM* phase at $r = 0.30$ is considerably larger than that of any of the other PEO-POSS(10-4) systems. We posit that the formation of coexisting phases relieves the chain stretching penalty associated with increased segregation.

In all three systems, the maximum in d_{CYL} occurs at the salt concentration for which we see the maximum of f_{CYL}.

In ref [125] we used the random phase approximation (RPA) to interpret scattering from disordered PEO-POSS/LiTFSI mixtures in terms of an effective Flory-Huggins interaction parameter, χ_{eff}. With one exception, all of the samples analyzed using RPA were amorphous and thus the fits of χ_{eff} reported in ref [125] are entirely valid. Interestingly, the disordered sample that is below T_c as measured by DSC exhibits a χ_{eff} that is a smooth extrapolation as a function of temperature from data obtained from amorphous systems. The data as presented in Figure 4.12 suggests that the crystallization of the POSS block is the most important driving force for phase separation, not the dependence of χ_{eff} on temperature and salt concentration.

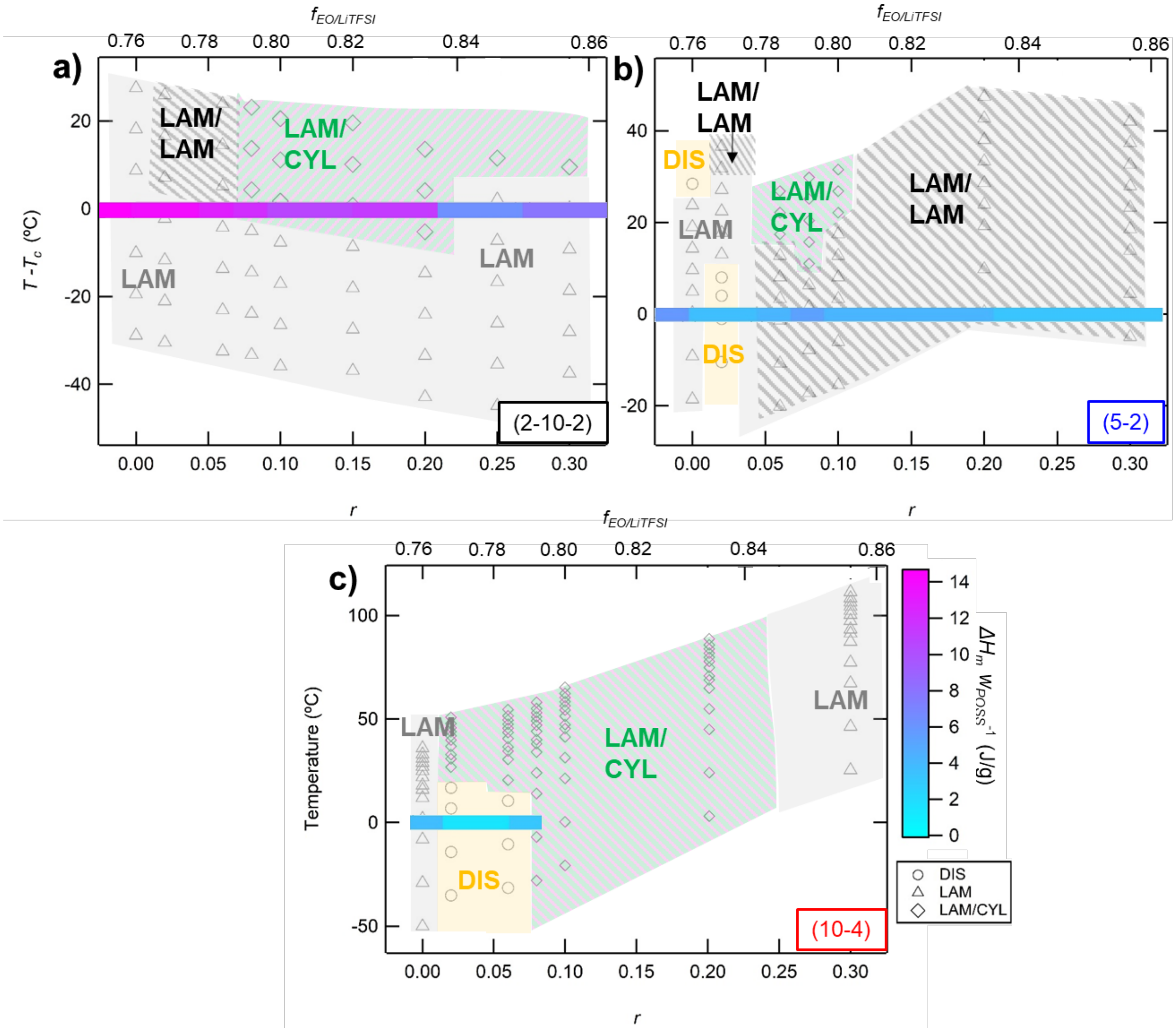

Figure 4.14. Phase diagram of a) POSS-PEO-POSS(2-10-2), b) PEO-POSS(5-2), and c) PEO-POSS(10-4)/salt mixtures recasting the data from Figure 4.12, replacing temperature with temperature subtracted by POSS block crystallization temperature ($T - T_c$) (T_c values in c) are extrapolated using the fit from Figure 4.9a).

Figure 4.14 recasts the data in Figure 12, replacing the vertical T axis with T- T_c. The color of the horizontal bars at T- $T_c = 0$ represents the magnitude of POSS domain melting enthalpy normalized by POSS weight fraction, $\Delta H_m w_{POSS}^{-1}$. This representation emphasizes the strong correlation between the crystallization and morphological transitions. Transitions from *LAM* to coexisting phases is seen close to T- $T_c = 0$ in POSS-PEO-POSS(2-10-2) (Figure 4.14a), which exhibits the largest ΔH_m. More complex behavior is seen in PEO-POSS(5-2) (Figure 4.14b). Featureless SAXS profiles are seen at high temperature in the neat sample, and at low temperatures in salt containing samples (r = 0.02). The *LAM*/*CYL* coexistence window is smaller in PEO-POSS(5-2) and it appears 20 °C above T_c. The value of T_c in PEO-POSS(10-4) at $r > 0.08$ is not discernable in DSC. For the purposes of plotting the data in Figure 14c and for completeness, we have used the fit shown in Figure 4.9a to estimate T_c. *DIS* to *LAM* transitions that coincide with T_c are seen in PEO-POSS(10-4) at salt concentrations $0 \leq r \leq 0.06$, that are quantitatively similar to those seen in PEO-POSS(5-2). At higher salt concentration, where the POSS block is amorphous, we see no thermal transitions with the emergence of a pure *LAM* phase at high salt concentrations.

4.4. Conclusion.

In this chapter, we elucidate the relationship between crystallization of the POSS block and self-assembly in a triblock copolymer, POSS-PEO-POSS, and two diblock copolymers, PEO-POSS, mixed with LiTFSI salt. In the copolymer/salt mixtures, the POSS block is semicrystalline and packs in a rhombohedral lattice, determined by DSC and WAXS. The percent crystallinity of the POSS block, determined by DSC, was greater in the triblock copolymer as compared to both diblock copolymers and the POSS homopolymer.

SAXS was used to determine the morphology of POSS-PEO-POSS and PEO-POSS/salt mixtures over a temperature range $60 \leq T \leq 140$ °C and $0 \leq r \leq 0.30$. Disorder or ordered phases with flat interfaces (*i.e.*, lamellae) are apparent in samples wherein the POSS block is semicrystalline. Pockets of POSS-rich cylinders form only in samples with amorphous POSS blocks and always coexist with lamellar grains. The copolymer/salt mixtures exhibit large windows of coexistence of lamellae and hexagonally packed cylinders, as well as coexisting lamellae with two different domain spacings over the experimental window. The correlation between POSS crystallization and phase transitions is greatest in systems wherein the POSS block exhibits the highest degree of crystallinity. The phase diagrams shown in Figure 11 are very different from other reports in the literature for two reasons: (1) the correlation between phase behavior and the crystallization of the POSS block, and (2) the presence of wide coexistence windows in the amorphous state that are not observed in the well-studied case of all-organic block copolymers.

In most theoretical phase diagrams of block copolymer/salt mixtures, the coexistence window that must lie between different ordered phases, due to the Gibbs Phase Rule, is ignored. [61,126–130] To our knowledge, the width of coexisting phases has only quantified for the case of symmetric lamellae, wherein the symmetry of both phases is assumed to be the same. [78] The presence of coexistence windows in all-organic copolymer/salt mixtures have been reported but are smaller as compared to the coexistence windows of the hybrid organic-inorganic/salt mixtures reported here. [74,131]

In the absence of crystallization, self-consistent field theory (SCFT) predicts that increasing *N* suppresses the disordered phases. [132,133] We find that when we compare the neat diblock copolymers, we see the disappearance of the *DIS* phase with increasing chain length as we would expect from SCFT. However, in the diblock copolymer/salt mixtures, the *DIS* window in diblock copolymer with larger *N* is greater than in the smaller diblock copolymer. This result is inconsistent with predicted phase diagrams using both classical SCFT as well as ionic SCFT. [103, 126,127,129]

Matsen demonstrated in analogous diblock and triblock copolymers the ordered phases in a theoretical phase diagram calculated by SCFT remains unchanged; however, the order-disorder phase boundary shifts to greater χN in triblock copolymers. [106] The triblock copolymer does not show *DIS* morphology in the neat state nor with added salt. The triblock copolymer neat data, therefore, is inconsistent with SCFT, which predicts the stabilization of *DIS*. [106, 122,126] It is possible that block copolymers with inorganic nanoparticles bonded to the terminus of pendant groups are fundamentally different from their classical all-organic counterparts.

4.5. Supporting Information

Table 4.2. DSC data for PEO-POSS diblock and POSS-PEO-POSS triblock copolymers mixed with LiTFSI salt

Polymer	*r*	T_M PEO (°C)	ΔH_m PEO (J/g)	T_g PEO (°C)	T_M POSS (°C)	ΔH_m POSS (J/g)	T_c POSS (°C)
(2-10-2)	0	53.8	93.61	-	114.9	4.17	104.0
(2-10-2)	0.005	50.7	75.43	-49.3	123.2	4.57	104.5
(2-10-2)	0.01	49.3	68.40	-41.7	123.4	4.48	104.0
(2-10-2)	0.02	48.8	65.68	-34.6	117.9	3.91	105.6
(2-10-2)	0.04	39.6	33.30	-38.6	125.8	3.77	105.6
(2-10-2)	0.06	35.6	28.64	-39.0	120.5	3.64	107.6
(2-10-2)	0.08	26.0	8.16	-40.4	121.3	3.40	108.4
(2-10-2)	0.1	-	-	-35.4	125.1	3.02	111.0
(2-10-2)	0.15	-	-	-24.2	129.0	3.19	112.0
(2-10-2)	0.2	-	-	-19.3	132.0	1.80	118.0
(2-10-2)	0.25	-	-	-10.3	129.2	2.24	120.0
(2-10-2)	0.3	-	-	-3.4	139.2	1.42	122.0
(10-4)	0	57.4	87.58	-	139.8	1.07	110.1
(10-4)	0.003	61.6	85.09	-	144.0	2.54	114.8
(10-4)	0.006	59.6	62.01	-	135.6	0.71	99.0
(10-4)	0.01	59.3	92.20	-	133.0	0.92	95.5
(10-4)	0.014	58.8	85.05	-	132.5	0.64	96.5
(10-4)	0.02	60.2	92.00	-34.2	134.8	0.43	95.2
(10-4)	0.025	57.8	74.19	-38.5	134.2	0.66	92.3
(10-4)	0.06	48.6	39.35	-33.6	135.0	0.92	91.5
(10-4)	0.08	43.3	0.50	-45.2	131.7	0.39	88.0
(10-4)	0.1	-	-	-39.8	-	-	-

(10-4)	0.2	-	-	-24.6	-	-	-
(10-4)	0.3	-	-	-11.0	-	-	-
(5-2)	0	54.2	97.05	-	126.9	1.67	103.1
(5-2)	0.002	53.5	87.50	-	122.8	1.06	112.0
(5-2)	0.004	55.3	92.30	-	121.1	0.35	110.6
(5-2)	0.006	54.7	81.32	-	118.8	0.98	113.6
(5-2)	0.008	52.9	78.87	-	123.1	0.71	110.3
(5-2)	0.01	53.6	84.43	-	125.8	0.24	113.8
(5-2)	0.012	53.0	90.22	-	124.3	0.77	113.9
(5-2)	0.014	53.5	87.28	-	124.2	1.27	115.0
(5-2)	0.016	50.7	61.39	-	122.8	1.09	110.0
(5-2)	0.018	49.8	73.17	-	122.1	1.49	110.3
(5-2)	0.02	54.2	65.22	-	126.3	1.05	95.0
(5-2)	0.04	49.5	58.68	-41.83	125.0	1.14	116.6
(5-2)	0.06	40.0	26.00	-49.3	127.0	1.20	104.7
(5-2)	0.08	33.2	9.00	-46.0	129.6	1.53	101.7
(5-2)	0.1	-	-	-40.0	130.0	1.20	100.0
(5-2)	0.2	-	-	-31.2	133.1	0.96	-
(5-2)	0.3	-	-	-24.4	144.4	0.37	89.5
POSS	0	-	-	-	147.31	9.80	76.8

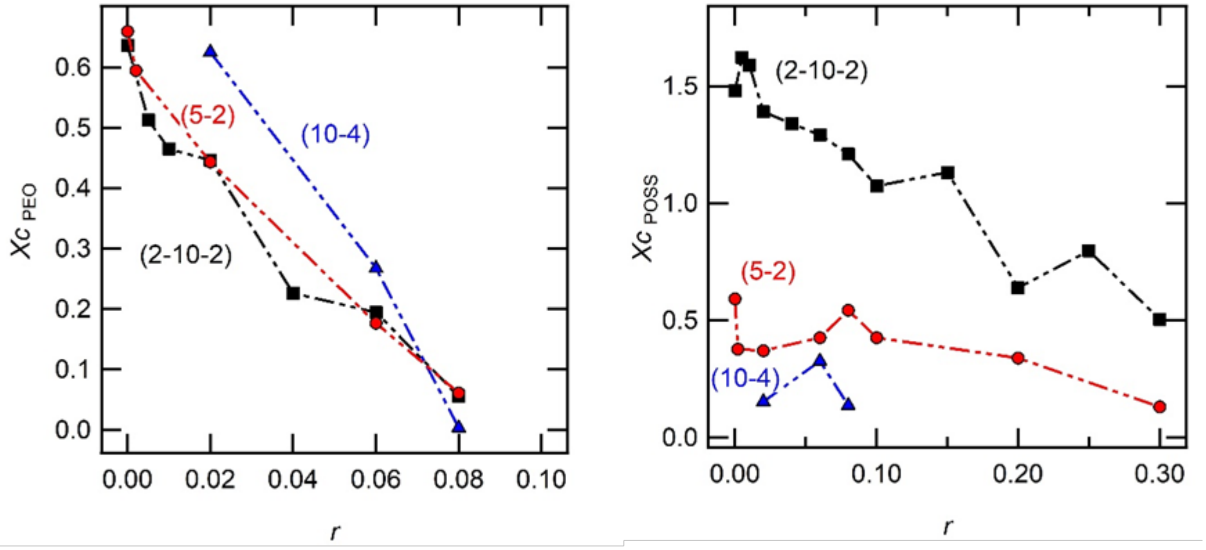

Figure 4.15. Percent crystallinity of PEO, $X_{c\ PEO}$ and POSS, $X_{c\ POSS}$

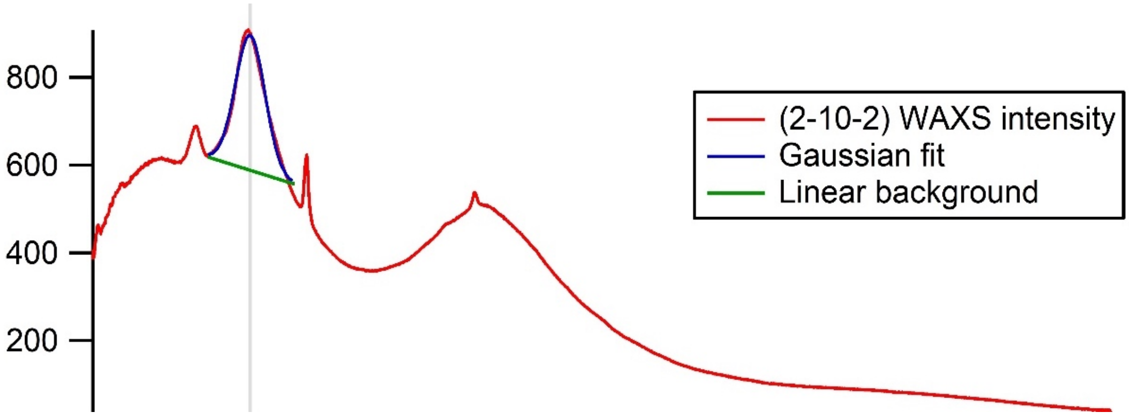

Figure 4.16. Gaussian fit to WAXS data in POSS-PEO-POSS(2-10-2) *r* = 0.02 at 113 °C

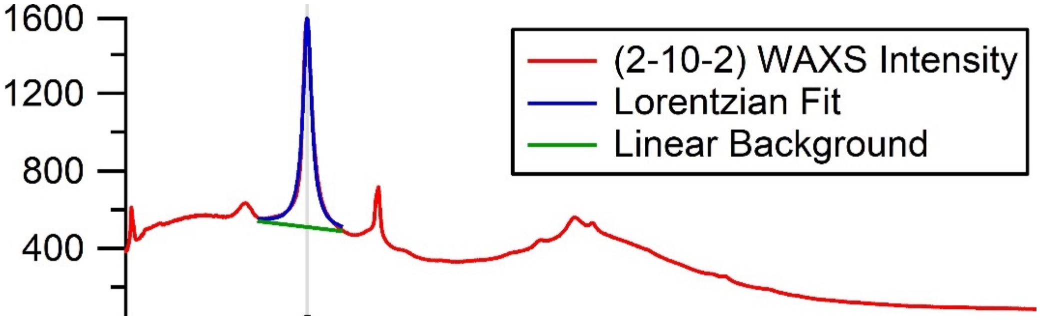

Figure 4.17. Lorentzian fit to WAXS data in POSS-PEO-POSS(2-10-2), *r* = 0.02 at 85 °C

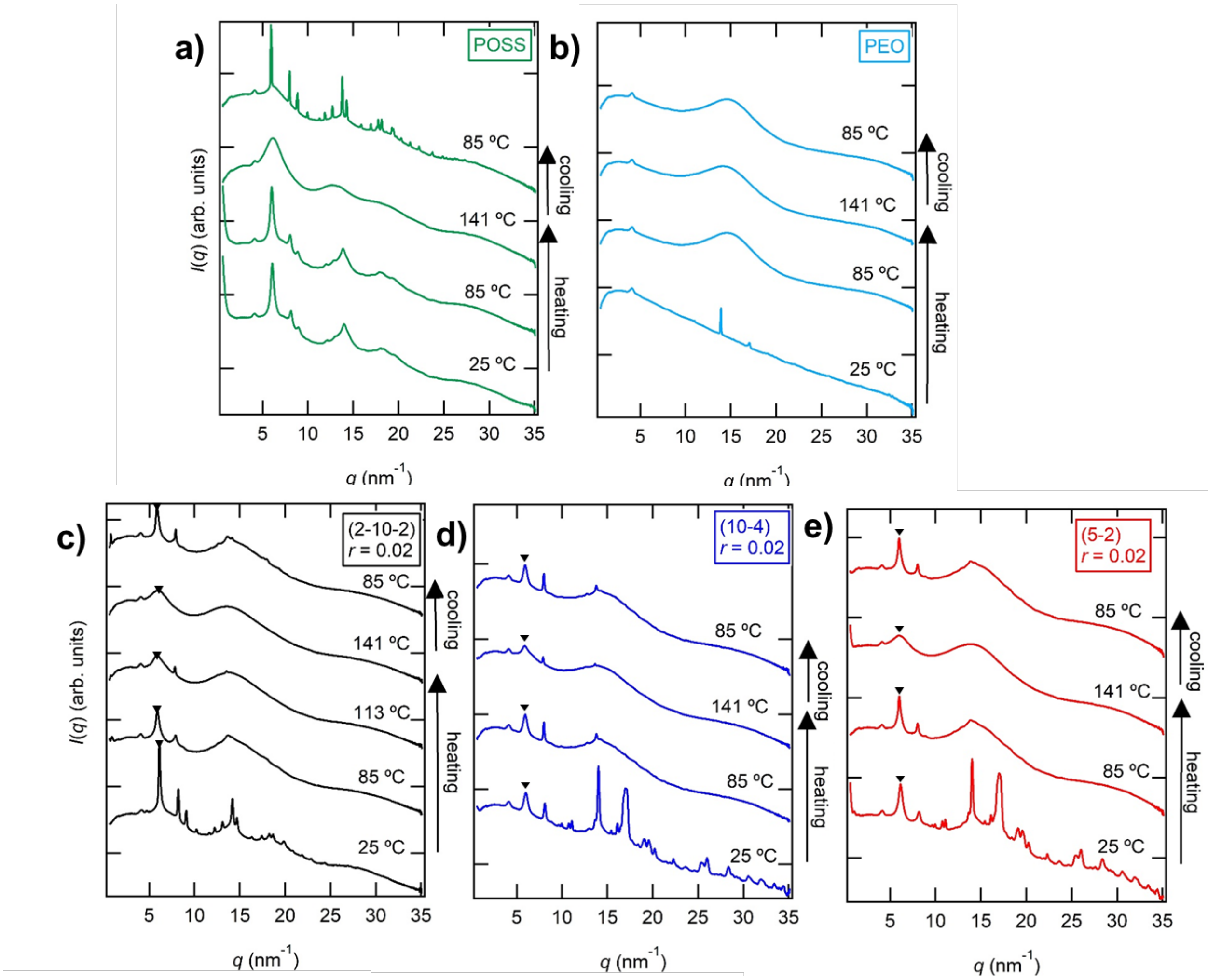

Figure 4.18. WAXS data in a) POSS homopolymer b) PEO homopolymer and in copolymers at *r* = 0.02 c) POSS-PEO-POSS(2-10-2), d) PEO-POSS(10-4), e) PEO-POSS(5-2)

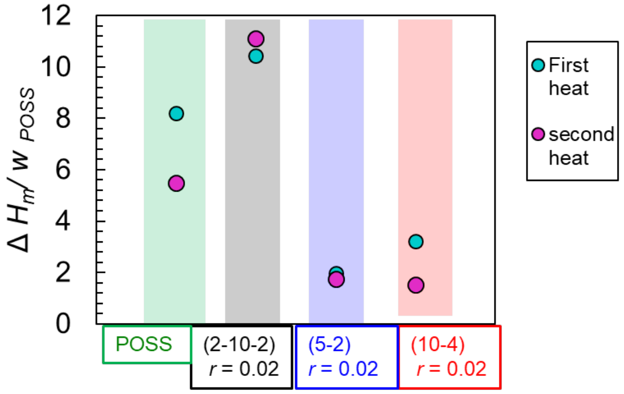

Figure 4.19. Enthalpy of melting of the POSS domain normalized by POSS weight percent ($\Delta H_m w_{POSS}^{-1}$) determined by the first and second DSC heating cycles in POSS homopolymer and copolymer/salt mixtures at $r = 0.02$.

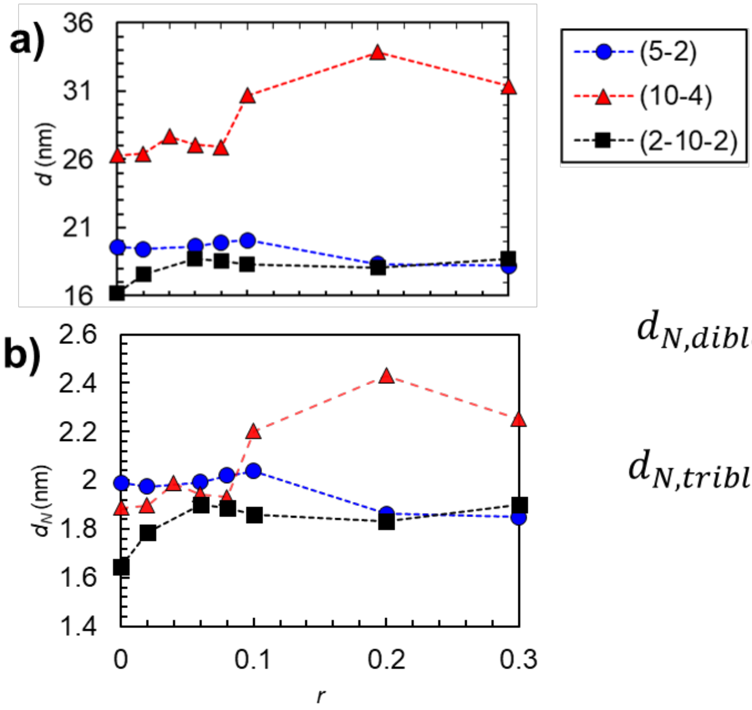

$$d_{N,diblock} = d\ N^{-1/2}$$

$$d_{N,triblock} = d\ (\frac{N}{2})^{-1/2}$$

Figure 4.20. a) Domain spacing, d and b) normalized domain spacing, d_N, at 90 °C as a function of salt concentration, r, in all copolymer/salt mix

LIST OF SYMBOLS

CYL	hexagonally packed cylinders morphology
d	domain spacing (nm)
d_{CYL}	domain spacing of hexagonally packed cylinders (nm)
d_{LAM}	domain spacing of lamellae (nm)
$d_{LAM,I}$	domain spacing of first lamellar phase (nm)
$d_{LAM,II}$	domain spacing of second lamellar phase (nm)
DIS	disordered morphology
f_{CYL}	fraction of hexagonally packed cylinders grains
f_{EO}	volume fraction of PEO microphase
$f_{EO/LiTFSI}$	volume fraction of PEO/LiTFSI microphase
I	X-ray scattering intensity
LAM	lamellar morphology
LAM/CYL	coexisting lamellar/hexagonally packed cylinders morphology
LAM/LAM	coexisting lamellar/lamellar morphology
M_{EO}	molecular weight of the poly(ethylene oxide) unit (kg mol^{-1})
M_i	molecular weight of species i (g mol^{-1})
M_P	molecular weight of the polyhedral oligomeric silsesquioxane unit (kg mol^{-1})
M_{PEO}	molecular weight of the poly(ethylene oxide) block (kg mol^{-1})
M_{POSS}	molecular weight of the polyhedral oligomeric silsesquioxane block (kg mol^{-1})
N	degree of polymerization
N_i	degree of polymerization of species i
q	scattering vector (nm^{-1})
$q*$	scattering vector at the primary scattering peak (nm^{-1})
q_1*	scattering vector at the first primary scattering peak (nm^{-1})
q_2*	scattering vector at the second primary scattering peak (nm^{-1})
r	salt concentration ([Li] [EO]$^{-1}$)
$S_{\sqrt{3}q*}$	SAXS invariant centered around $q = \sqrt{3}q*$

S_{2q*}	SAXS invariant centered around $2q*$
S_T	SAXS invariant at $q = q*$ of the SAXS profile calculated at temperature, T
S_{Tmax}	SAXS invariant at the maximum temperature
T	temperature (°C)
T_c	POSS block crystallization temperature (°C)
T_m	POSS block melting temperature (°C)
w_{POSS}	weight fraction of POSS block
X_c	percent crystallinity of POSS block
x	molecular weight of PEO chain (kg mol^{-1})
y	molecular weight of the POSS chain (kg mol^{-1})

GREEK

ΔH_m	Enthalpy of melting of the POSS block (J g^{-1})
θ	X-ray scattering angle
λ	X-ray wavelength (1.2398 Å)
v_{EO}	molar volume of ethylene oxide monomer unit (nm^3)
v_i	molar volume of unit i (nm^3)
v_{POSS}	molar volume of POSS monomer unit (nm^3)
v_{ref}	reference volume (0.1 nm^3)
ρ_i	density of unit i (g cm^{-3})
ρ_{PEO}	density of PEO chain (g cm^{-3})
ρ_{POSS}	density of POSS chain (g cm^{-3})

5. Effect of microphase separation on the limiting current density in hybrid organic-inorganic copolymer electrolytes

ABSTRACT

Hybrid organic-inorganic block copolymer electrolytes are of interest to enable batteries containing lithium metal anodes. The conductive block is a standard polymer electrolyte of poly(ethylene oxide) and the mechanically rigid block is an inorganic poly(acryloisobutyl polyhedral oligomeric silsesquioxane) polymer. In this paper, we compare a poly(acryloisobutyl polyhedral oligomeric silsesquioxane)-*b*-poly(ethylene oxide)-*b*-poly(acryloisobutyl polyhedral oligomeric silsesquioxane) (POSS-PEO-POSS) triblock copolymer and a poly(ethylene oxide)-*b*-poly(acryloisobutyl polyhedral oligomeric silsesquioxane) (PEO-POSS) diblock copolymer mixed with lithium bis(trifluoromethanesulfonyl)imide salt. We have experimentally measured the limiting current density in lithium symmetric cells containing hybrid organic-inorganic electrolytes at 90 °C. The cells were polarized at a large range of applied current density. The diblock copolymer electrolyte exhibited a clear plateau in cell potential at all current densities below the limiting current density. At low applied current density, the triblock copolymer electrolyte also exhibited a clear plateau in cell potential. At currents approaching the limiting current density, the triblock copolymer electrolyte exhibited an underdamped potential profile. The cell potential did not reach a plateau at current densities above the limiting current in both systems. The diblock and triblock copolymer electrolytes were fully characterized using electrochemical methods to determine the ionic conductivity, cation current fraction, salt diffusion coefficient, and open circuit voltage as a function of salt concentration. Cell potential and salt concentration as functions of position in the cell at various current densities were calculated using Newman's concentrated solution theory. The theoretical limiting current density was calculated to be the current density at which salt is depleted at the cathode. We see quantitative agreement between experimental measurements and theoretical predictions for the limiting current density in the diblock copolymer electrolyte which has an ordered structure at all salt concentrations, while the experimental limiting current density is lower than the theoretical prediction for the triblock copolymer electrolyte, which exhibits a disordered morphology at high salt concentrations.

5.1. Introduction.

There is continued interest to develop electrolytes in order to improve stability and cycle life of secondary lithium batteries.[57] One approach is block copolymer electrolytes, which combine the benefits of ionically conductive polymers with nonconducting, mechanically rigid polymers.[30] While the full electrochemical characterization of liquid electrolytes[5,134] and homopolymer electrolytes[33,135] have been extensively reported, there are relatively few systematic studies using copolymer electrolytes.[136]

Electrolytes are most often characterized by measuring ionic conductivity, k, using ac impedance spectroscopy. Recognizing that conductivity in Li$^+$ conductors is often dominated by the mobility of the anion, it is fairly common to report the cation current fraction, r_+, obtained in a symmetric lithium-electrolyte-lithium cell using the Bruce-Vincent method.[137,138] The product $\square\square_+$ indicates the efficacy of an electrolyte in the limit of small (infinitesimal) currents.[139] Whether or not an electrolyte can be used in practical batteries depends on the relationship between current and potential in the limit of large currents. While this relationship will depend on the specific battery used in the experiment, the lithium-electrolyte-lithium cell provides a standardized platform for reporting this relationship. The passage of a current through the battery results in the formation of salt concentration gradients through the electrolyte between the cathode and the anode. Salt concentration gradients in the electrolyte increase when the cell is polarized at higher current density. The limiting current density is defined as the current density at which salt is depleted at the cathode[38]. There is growing recognition that the limiting current density is, perhaps, the most important metric of an electrolyte.[140,141]

In this study we present measurements of limiting current density in a poly(acryloisobutyl polyhedral oligomeric silsesquioxane)-*b*-poly(ethylene oxide)-*b*-poly(acryloisobutyl polyhedral oligomeric silsesquioxane) (POSS-PEO-POSS) triblock copolymer and a poly(ethylene oxide)-*b*-poly(acryloisobutyl polyhedral oligomeric silsesquioxane) (PEO-POSS) diblock copolymer mixed with lithium bis(trifluoromethanesulfonyl)imide (LiTFSI) salt. In the triblock copolymer, the PEO block has a molecular weight of 35 kg mol^{-1} and POSS block molecular weight of 4.7 kg mol^{-1}. In the diblock copolymer, the PEO block has a molecular weight of 5 kg mol^{-1} and POSS block molecular weight of 1.9 kg mol^{-1}. The volume fraction of the PEO block, f_{EO}, is 0.81 and 0.76 in triblock and diblock copolymer, respectively. Schematic 1 demonstrates the chemical structure of the diblock and triblock copolymers. The salt concentration in lithium/electrolyte/lithium cells used in the limiting current density experiments is held constant at $[Li]/[EO] = r = 0.10$. Table 1 summarizes the characteristics of the polymer electrolytes used in this study. The synthesis of the polymers is described in previous studies.[108,142] Block copolymers microphase separate into nanophase separated domains, creating channels that are ionically conductive. The morphology is affected by salt concentration.[62] In previous studies, we have studied this effect in a series of POSS-containing block copolymers.[108,142,143] The most commonly observed morphology in POSS-containing block copolymer/salt mixtures at 90 °C is alternating POSS-rich and PEO/LiTFSI-rich lamellae.

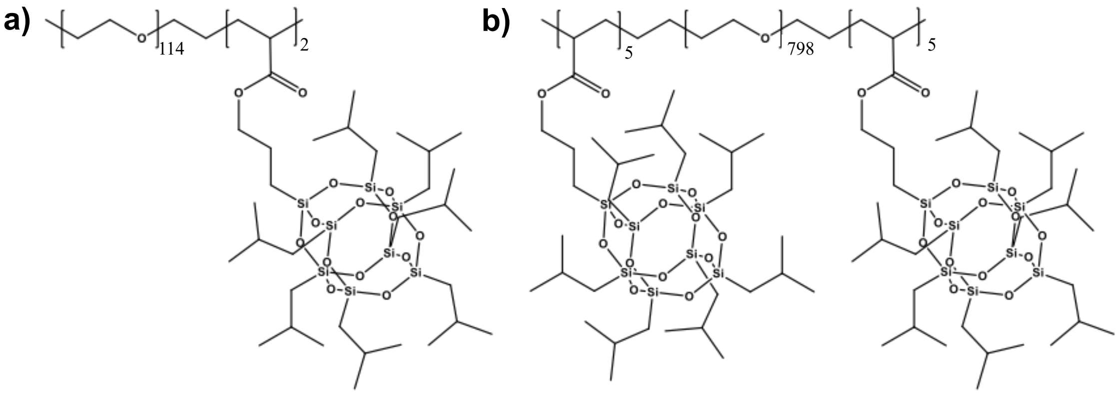

Figure 5.1. Chemical structure of a) diblock copolymer (PEO-POSS) and b) triblock copolymer (POSS-PEO-POSS) used in this study.

Table 5.1. Characteristics of neat polymer and polymer electrolytes

	M_{PEO} (kg mol^{-1})	M_{POSS} (kg mol^{-1})	N (120 °C)	$f_{EO/LiTFSI}$	d (90 °C) (nm)	Morphology (90 °C)
Triblock $r = 0$	35	9.28	634	0.81	26.1	*LAM*
Triblock $r = 0.10$	35	9.28	634	0.85	31.4	*LAM*
Diblock $r = 0$	5	1.86	97	0.76	19.6	*LAM*
Diblock $r = 0.10$	5	1.86	97	0.80	20.0/20.1	*LAM*/*LAM*

M_{PEO} = molecular weight of the PEO block; M_{POSS} = molecular weight of the POSS block determined by ^{1}H-NMR; N = chain length calculated at 120 °C and monomer reference volume of 0.1 nm^3; $f_{EO/LITFSI}$ = volume fraction of PEO/LiTFSI block; d = domain spacing at 90 °C determined by small-angle X-ray scattering.

Ion transport was characterized in triblock and diblock copolymer electrolytes by experimentally measuring κ, ρ_+, salt diffusion coefficient (D), and the concentration cell open-circuit potential (U) as a function of salt concentration. Newman's concentrated solution theory can be used to model the magnitude of salt concentration gradients as a function of position in an electrolyte at different applied currents density[139]. However, this theory was developed for 3-component homogenous electrolytes. The theoretical and experimental limiting current densities in a few homogenous electrolytes has been previously reported[40,144–149]. In contrast, block copolymers mixed with dissociated salt are 4-component heterogenous systems and complete characterization would require specification of 6 transport parameters and 2 thermodynamic factors. A theory that incorporates these parameters has not yet been developed. Our approach based on 3 transport coefficients and 1 thermodynamic factor is approximate. Nevertheless, this theoretical model was used to predict the limiting current density in both the triblock and diblock copolymer electrolytes. The theoretical limiting current density and the experimentally determined limiting current density are compared with no adjustable parameters.

5.2 Experimental

5.2.1 Electrolyte Preparation.

Electrolytes were prepared by mixing polymer with LiTFSI (Sigma-Aldrich). Due to the hygroscopic nature of LiTFSI, all sample preparation was carried out in an argon glovebox (MBraun) where H_2O and O_2 levels were maintained below 0.1 ppm and 0.6 ppm respectively. PEO-POSS and POSS-PEO-POSS polymers were dried at 90 °C under vacuum in the glovebox antechamber for 48 h and then transferred into the glovebox. LiTFSI was dried at 120 °C under vacuum in the glovebox antechamber for 48 h and then transferred into the glovebox. Dry polymer and LiTFSI salt were dissolved into anhydrous THF and the solutions were mixed at 55 °C for 24 hours. The caps were then removed from the vials allowing THF to evaporate and leave behind a homogeneous polymer/salt mixture inside of the glovebox. After drying on a hotplate at 60 °C for 48 h, the electrolytes were transferred to the glovebox antechamber and dried under vacuum for 48 h at 90 °C. The salt concentration in the copolymer was quantified by r, the molar ratio of lithium ions to ethylene oxide (EO) moieties. We assume that the salt resides exclusively in the PEO domain.

5.2.2 Blocking Electrode Cell Preparation.

Stainless steel symmetric cells were prepared for ionic conductivity measurements of electrolytes using ac impedance spectroscopy. Electrolytes were heated to 120 °C and pressed into a 3.175 mm diameter hole within a 250 μm thick silicone spacer. Two 200 μm- thick stainless-steel electrodes were pressed on either side of the electrolyte-filled spacer. The electrode thickness was measured using a micrometer. The thickness of each electrolyte (L) was determined by measuring the thickness of the cell and subtracting the thickness of the electrodes. Aluminum tabs were secured to the electrodes using Kapton tape. The entire cell was vacuum sealed in Showa-Denko pouch material leaving only the tab ends exposed.

5.2.3 Impedance Spectroscopy.

Each cell was placed in a custom-built heating stage. Cells were heated from 30 °C to 130 °C, cooled to 30 °C then heated back to 130 °C in 10 °C increments to ensure thermoreversibility of measurements. Cells were held at each temperature for 30 minutes before measurements were taken. Complex impedance measurements were acquired using a Biologic VMP3 potentiostat paired with EC-lab software for a frequency range of 1 MHz to 100 mHz at an amplitude of 50 mV. The resulting Nyquist plot was fit to an equivalent circuit, and the electrolyte bulk resistance (R_b) was extracted. This value was identical to the R_b determined from the low-frequency minimum on a Nyquist impedance plot. Ionic conductivity, κ, was calculated using the following expression,

$$\kappa = \frac{L}{aR_b}, [1]$$

where a is electrolyte area calculated using the inner diameter of the spacer, 3.175 mm. The standard deviation was used to estimate error bars from 3 or more cells. Results are reported for the second heating cycle at 90 °C.

5.2.4 Lithium symmetric cell preparation.

Lithium symmetric cells were prepared in a similar manner as the stainless-steel symmetric cells described in the preceding paragraph. Lithium electrodes were constructed by first brushing 150 μm thick lithium metal (MTI Corporation) then pressing using a pneumatic press inside of an argon glovebox to create a clean lithium surface. The lithium metal was backed by nickel foil to increase mechanical support and allow for even current distribution. Electrolytes were heated to 90 °C and pressed into a 3.175 mm diameter hole within a 250 μm thick silicone spacer. Cells were constructed by pressing the lithium electrodes on either side of the silicon spacer containing polymer electrolyte. The electrode thickness was measured using a micrometer. The thickness of each electrolyte was determined by measuring the thickness of the cell and subtracting the thickness of the electrodes. Nickel tabs were secured to the nickel side of the electrodes. These cells were vacuum sealed in pouch material leaving the nickel tabs exposed.

5.2.5 Lithium symmetric cell preconditioning.

Lithium symmetric cells were annealed at 90 °C in a custom heating stage for 4 h. Cells were preconditioned in order to stabilize the solid electrolyte interface (SEI) before electrochemical characterization at 90 °C using a Biologic VMP3 potentiostat paired with EC Lab software. Preconditioning consisted of five to eight polarization cycles with an applied current density (i) of 0.02 mA cm^{-2} for 4 h in both the positive and negative directions with a 2 h open circuit voltage (OCV) relaxation step between each polarization step. Impedance spectroscopy was performed in between each polarization cycle with a frequency range of 1 MHz to 100 mHz and amplitude of 50 mV. Time independent impedance spectroscopy data were taken as a signature of a stable SEI.

5.2.6 Chronoamperometry.

The steady-state current experiment was performed by polarizing preconditioned lithium symmetric cells at constant potential, ΔΦ, for 4 hours and measuring the current density reached at steady-state, i_{SS}. Impedance spectra were collected at every hour increment to probe the bulk and interfacial resistances (R_b, R_i). ΔΦ of 10 mV, -10 mV, 20 mV and -20 mV were utilized to ensure the results were independent of the sign and magnitude of the applied potential. The resistances of the cell initially ($R_{b,0}$ and $R_{i,0}$) and at steady-state ($R_{b,SS}$ and $R_{i,SS}$) were measured using impedance spectroscopy. The initial current density, i_Ω, is determined using Ohm's law,

$$i_\Omega = \frac{\Delta\Phi}{R_{i,0} + R_{b,0}} \ . [2]$$

The steady-state current fraction, ρ_+, is calculated as follows,

$$\rho_+ = \frac{i_{ss}(\Delta\Phi - i_\Omega R_{i,0})}{i_\Omega(\Delta\Phi - i_{ss} R_{i,ss})} \ . [3]$$

5.2.7 Concentration polarization.

Restricted diffusion measurements were obtained using the concentration polarization introduced by the steady-state current experiment outlined in the preceding paragraph. Upon removal of the applied potential, the open-circuit voltage, *OCV*, of the cell relaxed with time, *t*, for 4 h. The diffusion coefficient, *D*, is calculated as follows

$$\frac{-d \ \ln OCV}{dt} = \frac{\pi^2 D}{L^2}, [4]$$

where the left-hand side of the equation is the slope from the linear fit of –ln(*OCV*) vs. *t*. *L* is the thickness of the electrolyte. The standard deviation was used to estimate error bars from 3 or more cells.

5.2.8. Limiting current density experiments.

Current (*i*) was applied to preconditioned lithium symmetric cells containing polymer with salt concentration r = 0.10 in a stepwise manner, until the limiting current density was reached. All experiments were conducted at 90 °C. A cycle for one current experiment consisted of applying current in the positive direction until the potential reached steady state followed by applying current in the negative direction with 1h open circuit rest steps in between each step. A sample experiment is shown in Figure S1 in the Supporting Information. The time required to reach steady state potential (Φ_{ss}) varied from approximately 25 minutes to 4 h. In most cases, cells were used for one or two current cycles as the nucleation and growth of lithium dendrites short-circuited the cell. Polarization time was minimized to reduce the influence of dendritic growth. Impedance spectroscopy experiments were performed before and after each polarization step to determine the bulk and interfacial impedances.

5.2.9. Concentration cell potential experiments.

Concentration cells were prepared by creating a channel with dimensions 4 cm by 1.5 mm in a 250 μm thick silicone. Half of the channel was filled with reference electrolyte with salt concentration r = 0.08, and the other half was filled with electrolytes at different r. Lithium electrodes (lithium foil backed by nickel foil) were placed on both ends of the channel. Nickel tabs were secured to the electrodes. The assembly was vacuum sealed in pouch material. Each cell was annealed at 90 °C for 24 h before the value of cell potential, U was recorded; this length of time ensures the formation of stable interface layers prior to the electrochemical measurement. The concentration gradient relaxation process was measured over the course of several days. Three concentration cells were prepared at each salt concentration.

5.2.10 Small angle X-ray scattering.

The morphologies of the electrolytes were determined using small-angle X-ray scattering (SAXS). Samples were prepared inside an argon glovebox. Electrolytes were heated to 120 °C, then pressed into rubber spacers (1 mm thick, 1/8 in. inner diameter). Kapton windows were attached to either side of the electrolyte, and the assembly was sealed inside custom airtight aluminum holders. The samples were annealed at 120 °C under vacuum for at least 48 h. Measurements were performed at Beamline 7.3.3. at the Advanced Light Source (ALS) at Lawrence Berkeley National Laboratory and Beamline 1–5 at the Stanford Synchrotron Radiation Lightsource (SSRL) at SLAC National Accelerator Laboratory. Samples were held at 90 °C for at least 30 minutes in a custom-built heating stage before scans were taken. Silver behenate was used to determine the beam center and sample-to-detector distance. Two-dimensional scattering patterns were integrated azimuthally using the Nika program for IGOR Pro to produce one-dimensional scattering profiles.[109] Here we report the scattering intensity as a function of the magnitude of the scattering vector, q ($q = 4\pi \sin(\theta/2)/\lambda$) where θ is the scattering angle, and λ is the wavelength of the X-rays equal to 1.2398 Å at the ALS and 1.03232 Å at SSRL.

5.3 Results and Discussion.

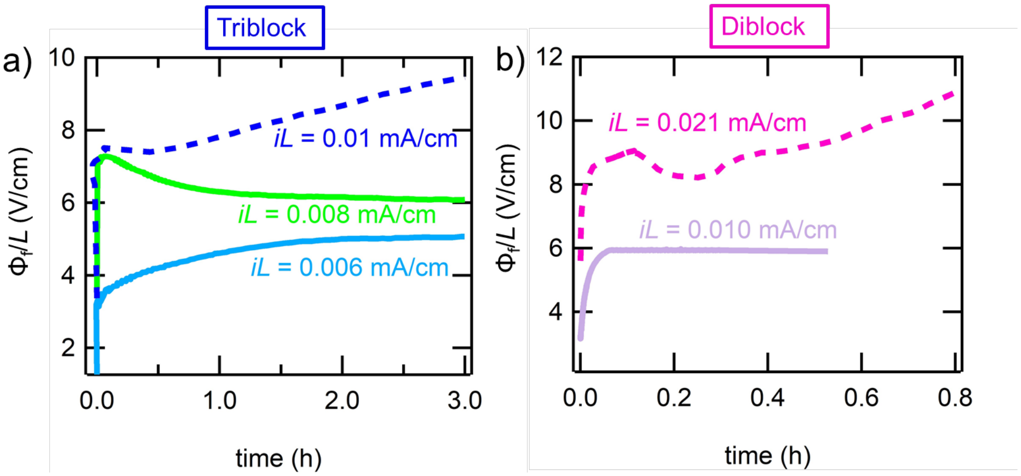

Figure 5.2. Length-normalized measured cell potential, Φ_f/L versus time for lithium symmetric cells of salt concentration $r = 0.1$ at different magnitudes of normalized applied current density, iL in a) triblock copolymer and b) diblock copolymer electrolytes at 90 °C. Solid lines indicate profiles where the cell reaches a steady-state potential during polarization current density below the limiting current. Dashes lines indicate profiles where potential diverges due to transport limitations above the limiting current density during polarization at high current density. Figure a) also demonstrates profiles in which an underdamped potential profile is observed at a polarization current density approaching the limiting current. Such profiles are not observed in b).

Figure 5.2a demonstrates time-dependence of the potential gradient, Φ_f/L, at several applied normalized current densities, iL, in lithium symmetric cells containing the triblock copolymer electrolytes with a salt concentration of [Li]/[EO] = r = 0.10. The parameter Φ_f is the potential drop across the cell after correcting for interfacial impedances. It thus accounts for the potential drop across the bulk electrolyte. In a symmetric cell, the dependence of Φ_f obtained at steady state at a given current density, i, will depend on electrolyte thickness, L. We have chosen to display our results on a plot of Φ_f/L versus iL because, in theory, this dependence should be independent of electrolyte thickness. Our choice of parameters used in Figure 5.2 facilitates comparisons with measurements conducted in other laboratories. The value of Φ_f is obtained after contributions from the interfacial impedance are subtracted according to Ohm's law as follows

$$\Phi_f = \Phi - iR_i a. \quad [5]$$

The value of interfacial resistance, R_i was obtained by impedance spectra taken in between each current step, and a is electrolyte area calculated using the inner diameter of the spacer used to contain the electrolyte in the lithium symmetric cell (3.175 mm). At iL = 0.006 mA/cm, Φ_f/L increases with time then reaches a plateau after 2 hours at approximately 5 V/cm. The overdamped time-dependence seen in Figure 1a is a standard signature of a potential profile wherein $i < i_{lim}$. When iL is increased to 0.008 mA/cm, we see a fundamentally different profile. Φ_f/L initially increases with time to a value of 7.5 V/cm. However, over the course of the next 2 hours, Φ_f/L decreases and reaches a plateau at a value of 6 V/cm. In many non-linear dynamical systems, increasing the magnitude of the perturbation results in a change from overdamped to underdamped behavior.[150] The result in Figure 5.2a is thus not surprising, given the highly non-linear nature of electrochemical systems, especially as they approach the limiting current.[38,151] The behavior shown in Figures 5.2a is reversible; decreasing the current density back to iL = 0.006 mA/cm results in a return to overdamped dynamics and thus, is not ascribed to the unstable deposition of lithium metal on the electrode. At iL = 0.01 mA/cm, Φ_f/L continually increases with time and does not plateau over the course of 4 hours. This is an indication of $i > i_{lim}$. The crossover from overdamped to underdamped behavior appears to be an announcement that the triblock copolymer electrolyte is in the vicinity of the limiting current.

Figure 5.2b demonstrates Φ_f/L versus time in two lithium symmetric cells containing the diblock copolymer electrolyte with salt concentration r = 0.10 at two different applied currents. At iL = 0.01 mA/cm, a similar overdamped profile to that seen in Figure 5.2a at iL = 0.006 mA/cm is seen, indicating $i < i_{lim}$. At iL = 0.021 mA/cm, a similar profile to that seen in Figure 1a at iL = 0.010 mA/cm, is seen indicating $i > i_{lim}$. We note that underdamped time-dependence is not seen in any of the diblock copolymer electrolyte potential profiles.

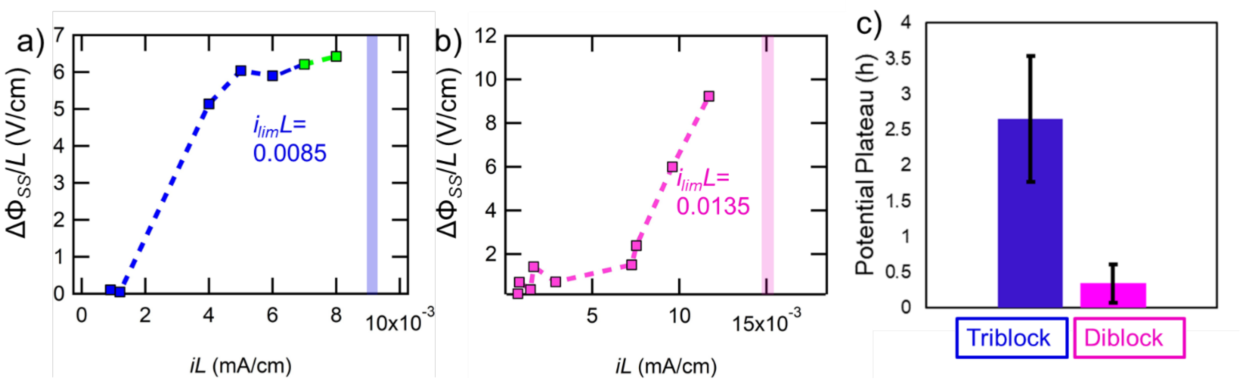

Figure 5.3. Length-normalized steady-state cell potential, $\Delta\Phi_{SS}/L$, plotted against normalized applied current density, iL, in a) triblock copolymer and b) diblock copolymer electrolytes in lithium symmetric cells of approximate thickness L = 300 µm at salt concentrations r = 0.10 at 90 °C. Each data point represents a unique cell. Horizontal bars indicate measurements where potential diverges due to transport limitations above the limiting current density during polarization. The limiting current density, $i_{lim}L$, is the average between the last normal measurement, and the horizontal bar. c) Time required to reach the potential plateau averaged across all experiments conducted at currents below the limiting current.

The results of all current density experiments performed on the triblock copolymer electrolyte (r = 0.10) at 90 °C are summarized in Figure 5.3a where the steady-state potential gradient $\Delta\Phi_{SS}/L$, is plotted as a function of normalized current density, iL. $\Delta\Phi_{SS}$ represents the plateau in potential that is reached in experiments performed at $i < i_{lim}$. $\Delta\Phi_{SS}$ was subtracted by the OCV potential which was slightly greater or less than zero due to the Seebeck effect and unavoidable temperature gradients in the cell. Closed blue data points represent profiles in which an overdamped potential profile is seen (see Figure 5.2a, iL = 0.006 mA/cm). Green data points represent an underdamped potential profile (see Figure 5.2a, iL = 0.008 mA/cm). The vertical bar at iL = 0.009 mA/cm indicates $i > i_{lim}$ (see Figure 1a, iL = 0.01 mA/cm). We observe a general increase in $\Delta\Phi_{SS}/L$ with increasing iL. We define the length normalized limiting current, $i_{lim}L$, as the average of the highest current density for which $\Delta\Phi_{SS}$ was observed and the current density at which $\Delta\Phi_{SS}$ was not observed. Thus, $i_{lim}L$ = 0.0085 mA/cm for the triblock copolymer electrolyte. Half of the difference between these two current densities is taken as the error (± 0.0005 mA/cm).

The results of all current density experiments performed on the diblock copolymer electrolyte (r = 0.10) at 90 °C are summarized in Figure 5.3b. At all current densities classical overdamped potential profiles were observed. As in Figure 5.3b, the vertical bar at iL = 0.015 indicates $i > i_{lim}$. Using the same method outlined in the preceding paragraph, $i_{lim}L = 0.0135 \pm 0.0015$ mA/cm in the diblock copolymer electrolyte.

Figure 5.3c plots time to reach plateau potential averaged over all experiments performed in the triblock copolymer (Figure 5.3a) and the diblock copolymer (Figure 5.3b) at r = 0.10. The triblock copolymer electrolytes on average took 2.5 hours to plateau, while the diblock copolymer electrolytes on average took 0.4 hours to plateau. While a rigorous analysis of the time-dependent profiles that underlie the data in Figure 5.3a and 5.3b, it is outside of the scope of this paper, a possible reason for this difference will be discussed shortly.

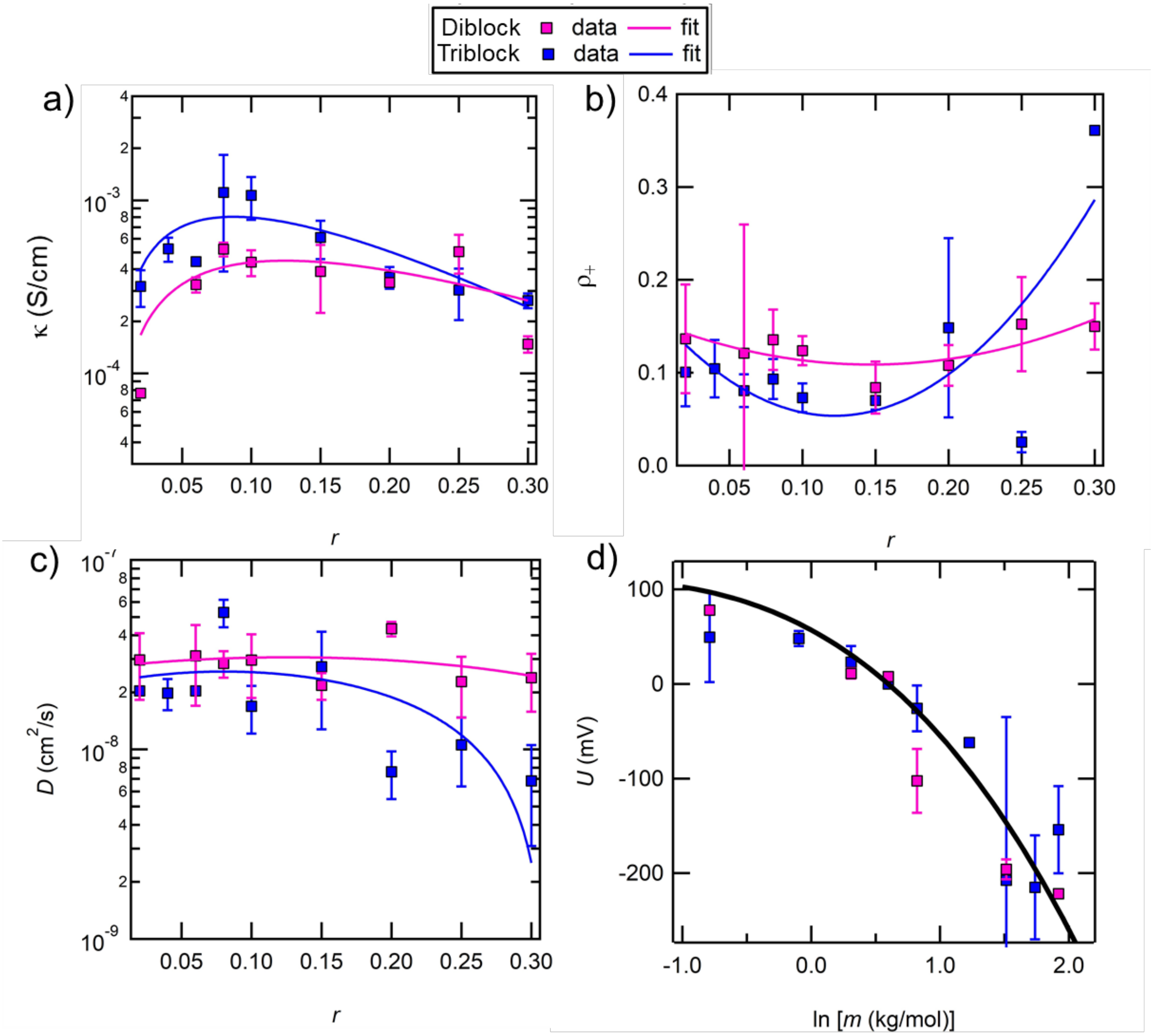

Figure 5.4. Measured transport coefficients. a) Ionic conductivity (κ) b) current fraction (ρ_+) c) diffusion coefficient (D) as a function of salt concentration, r, and d) concentration cell open-circuit potential (U) as a function of natural log molality (ln[m]) at 90 °C. Fits are shown as solid lines through data points.

We use Newman's concentrated solution theory to predict the limiting current in our electrolytes (i_{lim}) using process described by Pesko *et al*[145]. This requires the full electrochemical characterization of the triblock and diblock copolymer electrolytes at 90 °C, shown in Figure 5.4a-d.

Figure 5.4a demonstrates the ionic conductivity (κ) as a function of r at 90 °C shown as markers and fits shown as solid lines to the following expression of the form proposed by Mongcopa *et. al.*[41]

$$\kappa = A_{\kappa}\, r_{av} * \exp[-r_{av} / B_{\kappa}], \ [6]$$

where A_{κ} and B_{κ} are fitting parameters shown in Table 5.2 for both the diblock and triblock copolymer electrolytes.

Table 5.2. Fitting parameters used in Figure 5.4

Diblock	A_x	B_x	C_x
κ	0.0097865	0.12447	--
ρ_+	2.0854	-0.6129	0.1538
D	-2.0534E-07	5.1663E-08	2.7385E-08
U	-13.8	66	74

Triblock	A_x	B_x	C_x
κ	0.025046	0.087231	--
ρ_+	7.2688	1.7677	0.1621
D	-4.8153E-07	7.7335E-08	2.2657E-08
U	-13.8	66	74

Figure 5.4b demonstrates current fraction (ρ_+) and Figure 5.4c demonstrates diffusion coefficient (D) as a function of r at 90 °C shown as markers and fits shown as solid lines to the following second-order polynomials

$$\rho_+ = A_{\rho+}\, r_{av}^2 + B_{\rho+}\, r_{av} + C_{\rho+}, \ [7]$$

$$D = A_D\, r_{av}^{\ 2} + B_D\, r_{av} + C_D. \ [8]$$

where $A_{\rho+}$, $B_{\rho+}$, $C_{\rho+}$, A_D, B_D, and C_D are fitting parameters to the data shown in Figure 3b and 3c for both copolymer electrolytes, shown in Table 5.2.

The symbols in Figure 5.4d show the dependence of the concentration cell open-circuit potential (U) on salt molality (m) in the PEO/salt rich microphase. This is calculated assuming all the added salt resides in the PEO-rich microphase. The solid curve in Figure 5.4d is taken from the work of Galluzzo *et. al.* who studied the open circuit potential in both poly (ethylene oxide) and poly (ethylene oxide)-b-poly(styrene) block copolymer electrolytes.[136] That studied compared a wide variety of electrolytes with block copolymer of different molecular weights and compositions and it was found that the open circuit potential from all systems collapsed when plotted as a function of m. This collapse indicates that in block copolymer electrolytes where the salt resides exclusively in one of the domains, the open-circuit potential mainly reflects interactions between the lithium ions and that microphase. It is evident from Figure 3d that the fit that the data obtained by our POSS-containing block copolymers is consistent with the fit presented in ref [136]. In this study, we will thus use the parameters given in ref [136].

$$U = A_U \ln[m]^2 + B_U \ln[m] + C_U, \text{ [9]}$$

We note that the concentration cell reference salt concentration used in ref [136] was r_{av} = 0.065. In our experiments, a reference salt concentration used was $r = 0.08$. A vertical shift was used to adjust the equation used in ref [136] to our data. Our analysis requires evaluation of $\frac{dU}{d\ln[m]}$, which is independent of the vertical shift, and has the following form,

$$\frac{dU}{d\ln[m]} = 2A_U \ln[m] + B_U. \text{ [10]}$$

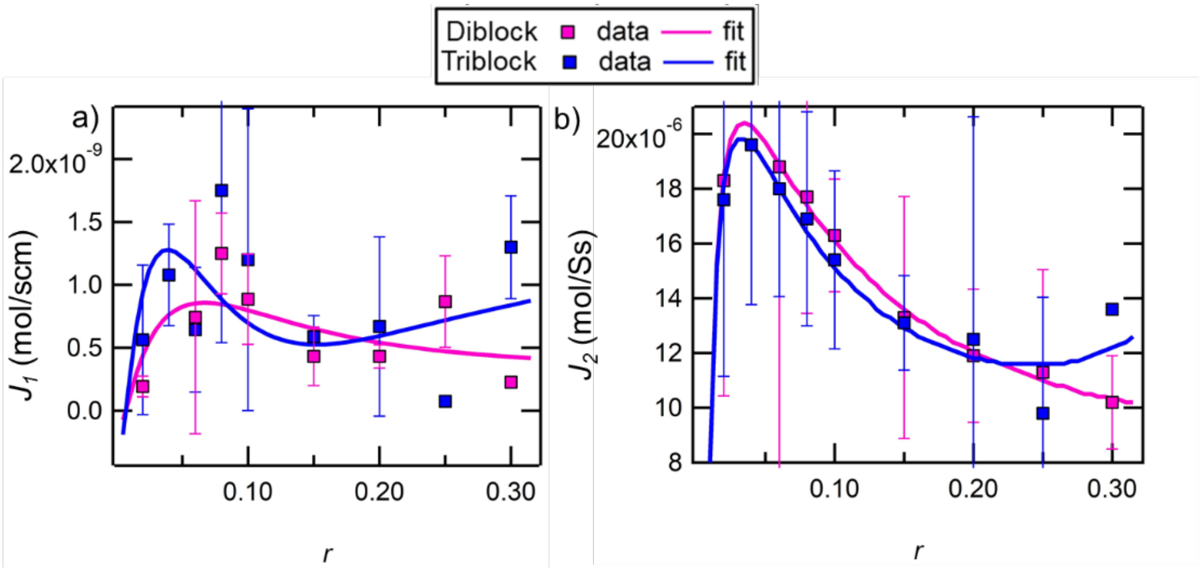

Figure 5.5. Integrand expressions. a) J_1 b) J_2 as a function of r at 90 °C in the diblock and triblock copolymer electrolytes. Fits are shown as solid lines through the data.

For a given value of fixed applied current density, i, the salt concentration as a function of position in the cell, $r_{sp}(x)$, is given by the following expression

$$\int_{r_{sp}(x=0)}^{r_{sp}(x)} \frac{\kappa(r)[\frac{dU}{d\ln[m]}(r)]}{r(z_+v_+)f_{EO/LiTFSI}(1-\frac{1}{\rho_+(r)})}dr = \int_{r_{sp}(x=0)}^{r_{sp}(x)} J_1 dr = -iL\,(x/L)\,, [11]$$

where z_+ is the charge number and v_+ is the number of cations. The integrand in the left side of Equation 11 is called J_1. Our objective is to determine $r_{sp}(x)$ for a given value of average salt concentration, r_{av} and iL. This is done by first guessing $r_{sp}(x = 0)$ and solving for $r_{sp}(x)$ using Equation 11 between $0 \leq x/L \leq 1$ by numerical integration. The average of all calculated $r_{sp}(x)$ for all positions within the cell is then calculated. If it does not agree with the specified value of r_{av}, then $r_{sp}(x = 0)$ is changed until convergence. Once all $r_{sp}(x)$ at different points within the electrolyte are known, then the spatially dependent steady-state potential, $\Phi_{SS}(x)$, can be calculated using the following expression,

$$\Phi_{SS}(x) = \int_{r_{sp}(x=L)}^{r_{sp}(x)} \frac{\frac{dU}{d\ln[m]}(r)}{r(\rho_+(r)-1)(z_+v_+)f_{EO/LiTFSI}}dr = \int_{r_{sp}(x=L)}^{r_{sp}(x)} J_2 dr\,. [12]$$

where J_2 is the integrand in Equation 12, analogous to J_1.

The integrands J_1 and J_2 are plotted as a function of r in Figures 5.5a and 5.5b. The fitted equation to the data in Figure 5.5a used to compute the right side of Equation 11 is

$$J_1 = A_1 r \, Exp\left[-\frac{r}{B_1}\right](C_1 r^2 + D_1 r + E_1). [13]$$

The fitted equation to the data in Figure 4b used to compute the right side of Equation 12 is

$$J_2 = A_2 r \, Exp\left[-\frac{r}{B_2}\right](C_2 r^2 + D_2 r + E_2). [14]$$

Table 5.3. Fitting parameters used in Figure 5.5.

Diblock	A_x	B_x	C_x	D_x	E_x
1	5.0738e-006 ± 0.000155	0.11973 ± 0.0122	0.078773 ± 2.4	-0.032477 ± 0.991	0.0061345 ± 0.187
2	0.018888 ± 60.6	0.071005 ± 0.0053	2.3706 ± 7.6e+003	-0.52126 ± 1.67e+003	0.063286 ± 203

Triblock	A_x	B_x	C_x	D_x	E_x
1	-0.017759 ± 281	0.086436 ± 0.00341	-0.00015541 ± 2.46	4.3448e-005 ± 0.687	-4.1163e-006 ± 0.0651
2	0.015181 ± 42	0.077453 ± 0.00575	2.7411 ± 7.58e+003	-0.66356 ± 1.84e+003	0.075376 ± 208

All fitting parameters for the fits demonstrated in Figure 5.5a and 5.5b using Equations 13 and 14 are shown in Table 3 for both copolymer electrolytes. We note that Equation 13 and 14 have the same form, but different fitted parameters (*A*-*E*). The required integrations were performed analytically using Equations 15 and 16:

$$\int_{r_{sp}(x=0)}^{r_{sp}(x)} J_1 dr = -(A_1 B_1\{6B_1^3 C_1 + 2B_1^2(D_1 + 3C_1 r) + r\,[E_1 + r\,(D_1 + C_1 r)]\} + B_1\,[E_1 + r\,(2D_1 + 3C_1 r)]\,Exp[-r/B_1]\,\Big|_{r_{sp}(x=0)}^{r_{sp}(x)}. \quad [15]$$

$$\int_{r_{sp}(x=0)}^{r_{sp}(x)} J_2 dr = -(A_2 B_2\{6B_2^3 C_2 + 2B_2^2(D_2 + 3C_2 r + r\,[E_2 + r\,(D_2 + C_2 r)]\} + B_2\,[E_2 + r\,(2D_2 + 3C_2 r)]\,Exp[-r/B_2]\,\Big|_{r_{sp}(x=0)}^{r_{sp}(x)}. \quad [16]$$

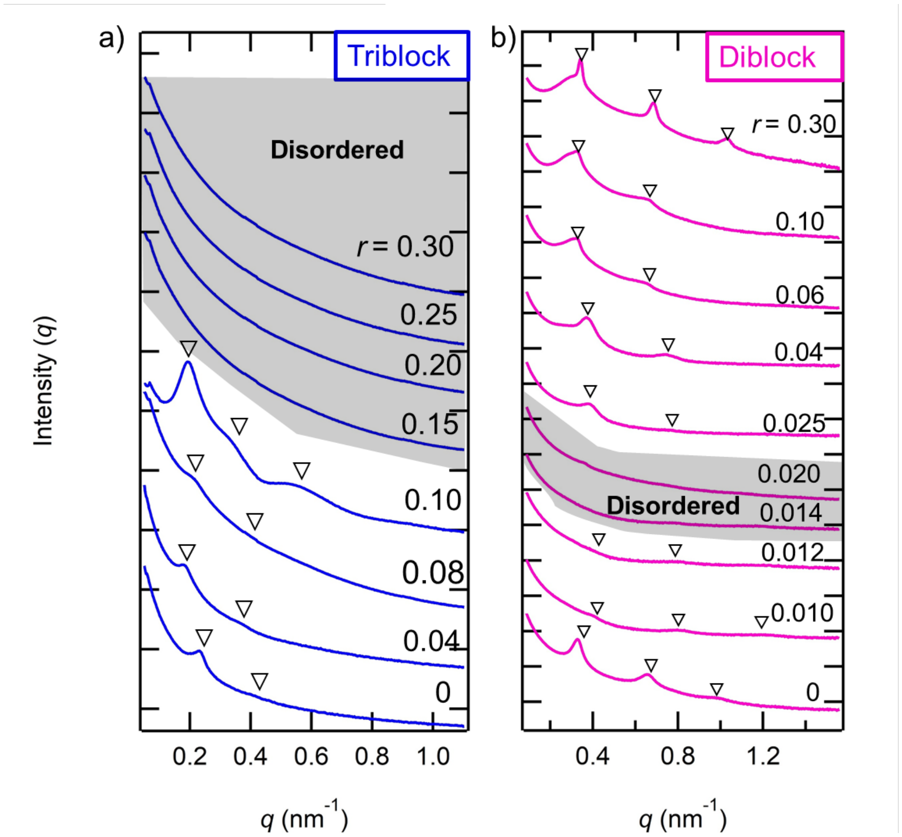

Figure 5.6. SAXS profiles. SAXS intensity is plotted as a function of the magnitude of the scattering vector, *q,* in a) triblock and b) diblock copolymer/salt mixtures at 90 °C. Salt concentration, *r*, is indicated on the right ($0 \leq r \leq 0.30$). ▼indicate peaks characteristic of lamellae ($q = q^*$, $2q^*$, $3q^*$). Shaded gray scans indicate disordered scattering profiles.

The effect of added salt on the morphology is shown in Figure 5.6a and 5.6b, where SAXS intensity is plotted as a function of the magnitude of the scattering vector, *q* at varied *r*. Figure

5.6a shows data for the triblock copolymer/salt mixtures. In the neat sample (r = 0), the SAXS pattern exhibits two peaks at $q = q^* = 0.22$ nm^{-1} and $q = 2q^*$, denoted by triangles, indicating the presence of alternating PEO/salt-rich and POSS-rich lamellae layers (*LAM*). The *LAM* morphology persists in the salt concentration range $0 \leq r \leq 0.10$. At $r = 0.15$, we see a monotonically decaying scattering profile, a standard signature of a disordered phase (*DIS*). *DIS* persists in the salt concentration range $0.15 \leq r \leq 0.30$. Thus, a transition from *LAM* to *DIS* occurs with increasing salt concentration at $r = 0.125 \pm 0.025$.

Figure 5.6a shows SAXS profiles for the diblock copolymer/salt mixtures. At salt concentrations $0 \leq r \leq 0.012$, the SAXS pattern reveals 3 peaks at $q = q^* = 0.35 \pm 0.02$ nm^{-1}, $q = 2q^*$, and $q = 3q^*$, denoted by triangles, indicating *LAM*. At $r = 0.014$, we see a monotonically decaying scattering profile, a standard signature of a disordered phase (*DIS*). *DIS* persists in the salt concentration range $0.014 \leq r \leq 0.02$. At $r \geq 0.025$, a *LAM* phase is observed in the scattering profiles and persists in the accessible salt concentration range ($0.025 \leq r \leq 0.30$). Thus, the diblock copolymer system exhibits a small *DIS* window with a lower boundary at salt concentration r = 0. 013 ± 0.001 and an upper boundary at r = 0. 0225 ± 0.0025.

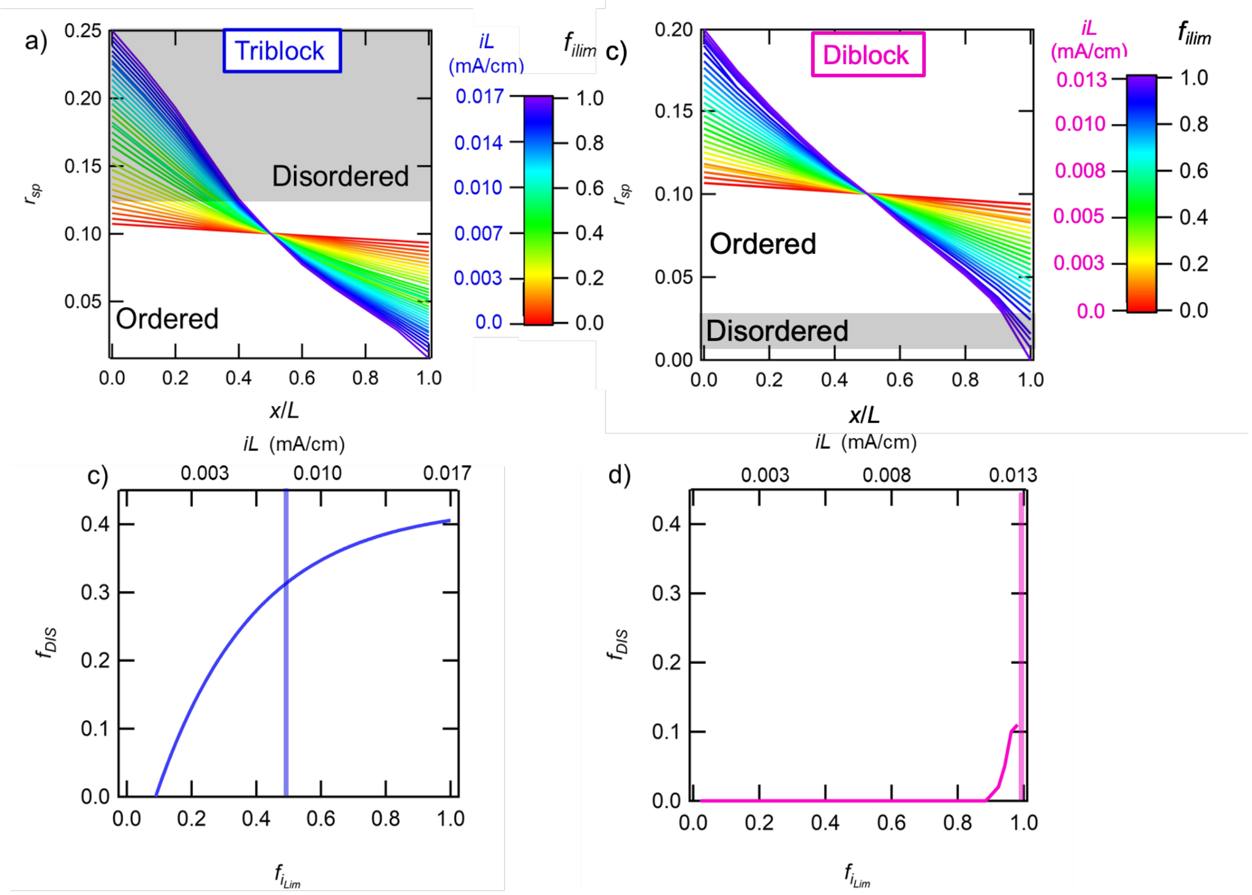

Figure 5.7. Salt concentration profiles, $r_{sp}(x/L)$ as functions of position through the cell at a range of current densities, i, with average salt concentration $r_{av} = 0.10$ in a) triblock copolymer and b) diblock copolymer electrolytes. $x/L = 1$ is the cathode side of the cell; $x/L = 0$ is the anode side of

the cell. Fraction of disordered morphology, f_{DIS}, as a function of fraction of theoretical limiting current f_{ilim} in c) triblock copolymer and d) diblock copolymer electrolytes.

Figure 5.7a and 5.7b plot the spatially determined salt concentration, r_{sp}, as a function of position ($0 \leq x/L \leq 1$), calculated using Equation 11, for both electrolytes with average salt concentration $r_{av} = 0.10$. $x/L = 1$ is the electrolyte/cathode interface; $x/L = 0$ is the electrolyte/anode interface. The current density, i, is incrementally increased until the theoretical limiting current density, $i_{lim,th}$ is reached, (i.e $r_{sp} = 0$ at $x/L = 1$). We define a fraction of theoretical limiting current density as follows: $f_{ilim} = i/i_{lim.th}$. The color of each salt concentration gradient corresponds to different values of f_{ilim} and iL. We observe an increase in the salt concentration gradient with increasing f_{ilim} in both electrolytes. $i_{lim,th}$ in the triblock copolymer electrolyte is 0.017 mA/cm, while $i_{lim,th}$ in the diblock copolymer electrolyte is 0.013 mA/cm. We note that the data in the salt concentration range $0 \leq r_{av} < 0.02$ is outside of the range of experimentally determined electrochemical transport parameters and thus is an estimated based upon the fit demonstrated in Figure 5.5a.

The *DIS* salt concentration window is shaded in gray in Figure 6a and 6b. As shown in Figure 5.6a and 5.6b, the *DIS* phase occurs at a larger range of salt concentrations in the triblock copolymer electrolytes as compared to the diblock copolymer electrolytes. The fraction of *DIS*, f_{DIS} is defined as the fraction of electrolyte in the salt concentration range that exhibits *DIS* morphology. Figure 5.7c and 5.7d plot f_{ilim} as a function of fraction of f_{DIS} in the triblock copolymer and diblock copolymer electrolyte respectively, where the secondary x-axis plots the corresponding value of *iL*. The triblock copolymer electrolyte exhibits a steep increase in f_{DIS} at $f_{ilim} > 0.10$. At $f_{ilim} = 1$, f_{DIS} reaches a maximum of 0.40. Figure 6d demonstrates f_{DIS} is much lower in the diblock copolymer electrolyte at all f_{ilim}. f_{DIS} is 0, with the exception of $0.9 < f_{ilim} < 1.0$, where f_{DIS} reaches a maximum of 0.10. Experimentally determined i_{lim} is plotted alongside the data in Figures 6b and 6d, shown as a vertical bar. Figure 5.7b demonstrates that the triblock copolymer electrolyte i_{lim} is reached when $f_{ilim} = 0.46$, while Figure 5.7d shows the diblock copolymer electrolyte i_{lim} is reached when $f_{ilim} = 1$. This large difference is attributed to $f_{DIS} = 0.30$ in the triblock copolymer electrolyte, while $f_{DIS} = 0.10$ in the diblock copolymer electrolyte.

The results shown in Figure 5.7a-d demonstrate that morphology is an important parameter in determining i_{lim}. The model used to estimate the limiting current density does not account for changes in morphology.

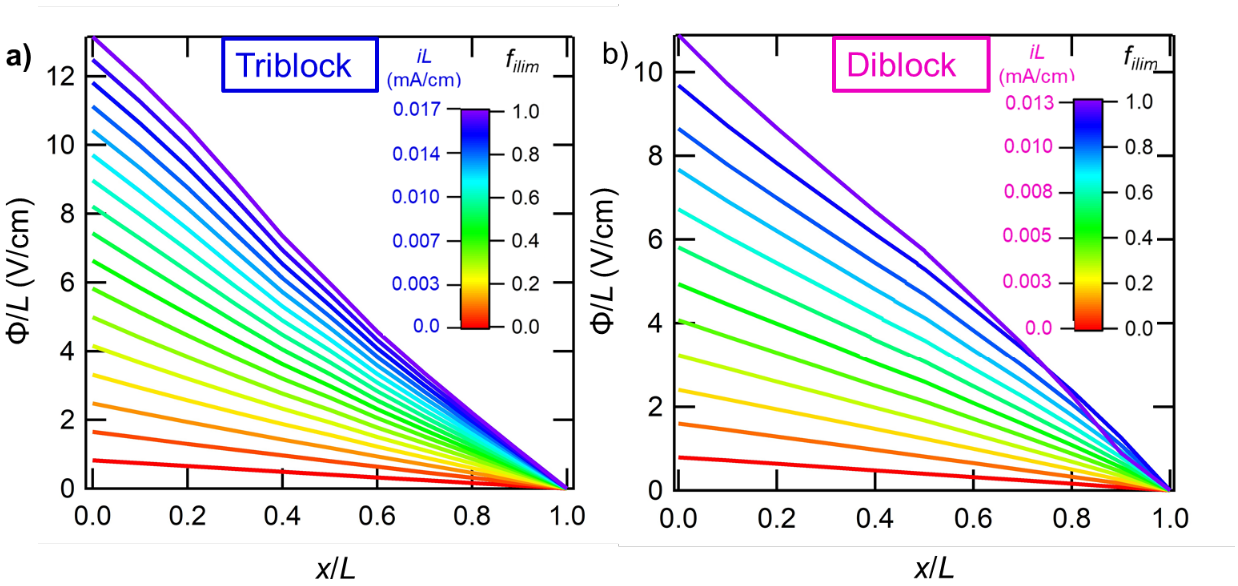

Figure 5.8. a) Simulated spatially dependent potential normalized by cell thickness (Φ/L) as a function of position in cell (x/L) for a range of r calculated at various current densities, iL in a) triblock copolymer and b) diblock copolymer electrolytes with average salt concentration $r = 0.10$.

Figure 5.8a and 5.8b demonstrates the potential normalized by cell thickness (Φ/L) as a function of position in electrolyte (x/L) calculated using Equation 12 in the triblock and diblock copolymer electrolytes respectively. The applied currents are the same as those shown in Figure 5.7 and range from $0 < i < i_{lim,th}$. The color scale bar notes the corresponding values of iL and f_{ilim}. As in Figure 5.7a and 5.7b, the results of the triblock and diblock copolymer simulations are comparable. The magnitude of Φ/L at $x/L = 0$ is greater in the triblock copolymer electrolytes as compared to the diblock copolymer electrolytes.

The theoretically predicted Φ_{SS} is taken to be the value of Φ at $x/L = 0$ and $iL < i_{lim}L$. The dashed curve in Figure 5.9 shows the theoretically predicted $\Delta\Phi_{SS}/L$. The terminus of this curve, represented by an 'x', represents the theoretical prediction for the limiting current. The data points represent the experimentally measured $\Delta\Phi_{SS}/L$ versus iL, recast from Figure 5.3a and 5.3b for the triblock and diblock copolymer electrolytes respectively at $r_{av} = 0.10$.

Figure 8a shows results for the triblock copolymer electrolyte and demonstrates quantitative agreement between experimental and theoretical $\Delta\Phi_{SS}/L$ when $iL < 0.009$ mA/cm. When $iL > 0.009$ mA/cm, the theoretical model predicts a continued linear increase in measured $\Delta\Phi_{SS}/L$. Experimentally, $iL > 0.009$ mA/cm $> i_{lim}L$. As previously discussed, the measured $i_{lim}L$ is 46% of the theoretical $i_{lim}L$. The shaded regions show the limit $f_{DIS} > 0.30$.

Figure 5.9b shows the results for diblock copolymer electrolyte and demonstrates lower measured $\Delta\Phi_{SS}/L$ than theoretically predicted $0 < iL < 0.008$ mA/cm. There is better quantitative agreement between experimental and theoretical $\Delta\Phi_{SS}/L$ when $iL > 0.010$. As previously discussed, the measured $i_{lim}L$ (0.0135 ± 0.015) is within error of theoretically predicted $i_{lim}L$ (0.013 mA/cm).

The mismatch between this theory and our experiments suggests our approach based on 3 transport coefficients and 1 thermodynamic factor does not account for all interactions within our complex systems.

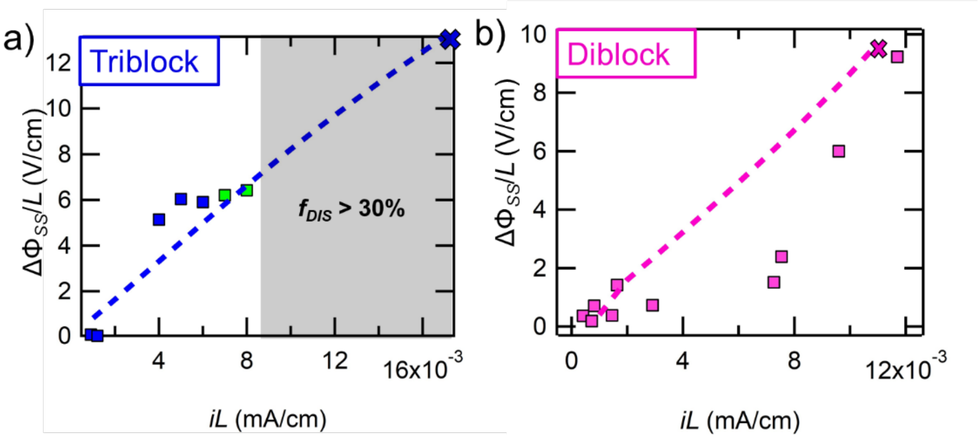

Figure 5.9. A comparison of experimentally measured (markers) (Figure 5.3) and modeled steady-state potentials (dashed line), $\Delta\Phi_{SS}/L$, versus applied current density, iL normalized by thickness in a) triblock copolymer and b) diblock copolymer electrolytes with r_{av} = 0.10. "X" indicates the experimentally determined limiting current. The area shaded in gray indicates where salt concentration profiles indicate that $f_{DIS} > 0.30$.

5.4. Conclusion.

The limiting current density in symmetric lithium cells at 90°C was determined experimentally in hybrid inorganic-organic triblock and diblock copolymer electrolytes. The time-dependence of the cell potential was recorded at fixed applied current densities. The steady-state cell potential was a smooth function of current density until a threshold; this threshold was taken as an indication that the applied current exceeded the limiting current density. While the diblock copolymer electrolytes exhibited overdamped profiles similar to those in homopolymer PEO, the triblock copolymer exhibited underdamped profiles at applied current densities close to the limiting current.

The diblock and triblock copolymer electrolytes were fully characterized at a large range of salt concentrations using electrochemical methods to determine the ionic conductivity, salt diffusion coefficient, current fraction, and the concentration cell steady-state potential as a function of average salt concentration. Newman's concentrated solution theory was used to simulate cell potential and salt concentration profiles to determine a theoretical limiting current (*i.e.,* the current at which the simulation predicted that the salt concentration at the cathode equals zero). The predicted limiting current is a factor of 2 greater than the experimentally determined limiting current in the triblock copolymer electrolyte. While the diblock copolymer electrolyte remains more-or-less ordered in the accessible salt concentration range, the triblock copolymer electrolyte exhibits a large, disordered window at high salt concentrations. Further work must be performed to better theoretically predict limiting current in complex, multicomponent systems.

5.5 Supporting Information

Table 5.4. Interfacial impedance (R_i) of preconditioned lithium/lithium symmetric cells containing the diblock copolymer electrolyte with salt concentration [Li]/[EO] = 0.10 and the corresponding steady state potential $\Delta\Phi_{SS}$ and steady state potential with the correction for potential drop due to interfacial layers ($\Delta\Phi_{SS} - iR_ia$). The spacer area (a) is constant at 0.079173 cm^2.

Cell #	R_i	i (mA/cm^2)	$\Delta\Phi_{SS}$ (V)	($\Delta\Phi_{SS} - iR_ia$) (V)	$iR_ia / \Delta\Phi_{SS}$ (%)
1	585	0.02	0.00700	0.006999990	0.000142857
2	1685	0.02	0.00610	0.006099990	0.000163934
3	582	0.02	0.00664	0.006639990	0.000150602
4	585	0.04	0.01370	0.013699993	5.10949E-05
5	645	0.04	0.01450	0.014499991	6.2069E-05
6	331	0.08	0.07200	0.071999840	0.000222222
7	1447	0.13	0.12000	0.119999210	0.000658333

Table 5.5. Interfacial impedance (R_i) of preconditioned lithium/lithium symmetric cells containing the triblock copolymer electrolyte with salt concentration [Li]/[EO] = 0.10 and the corresponding steady state potential $\Delta\Phi_{SS}$ and steady state potential with the correction for potential drop due to interfacial layers ($\Delta\Phi_{SS} - iRia$). The spacer area (a) is constant at 0.079173 cm^2.

Cell #	R_i	i (mA/cm^2)	$\Delta\Phi_{SS}$ (V)	($\Delta\Phi_{SS} - iR_ia$) (V)	$iR_ia / \Delta\Phi_{SS}$ (%)
1	18310	0.171306	0.30	0.29999800000	0.00066667
2	17258	0.247934	0.40	0.3999973637	0.00065907
3	28259	0.149893	0.35	0.34999737491	0.00075002
4	30252	0.107066	0.282	0.28199799101	0.00071241
5	30487	0.085653	0.240	0.23999839281	0.00066966

Table 5.4 and 5.5 show the experimentally determined values of interfacial impedance (R_i) of preconditioned lithium/lithium symmetric cells and the corresponding steady state potential ($\Delta\Phi_{SS}$) and steady state potential with the correction for potential drop due to interfacial layers ($\Delta\Phi_{SS}$ - iR_ia) for the diblock copolymer and triblock copolymer electrolyte respectively. We note that in both systems, the magnitude of iR_ia /$\Delta\Phi_{SS}$ is very small, and thus, the potential drop due to the interfacial layer does not alter our results substantially.

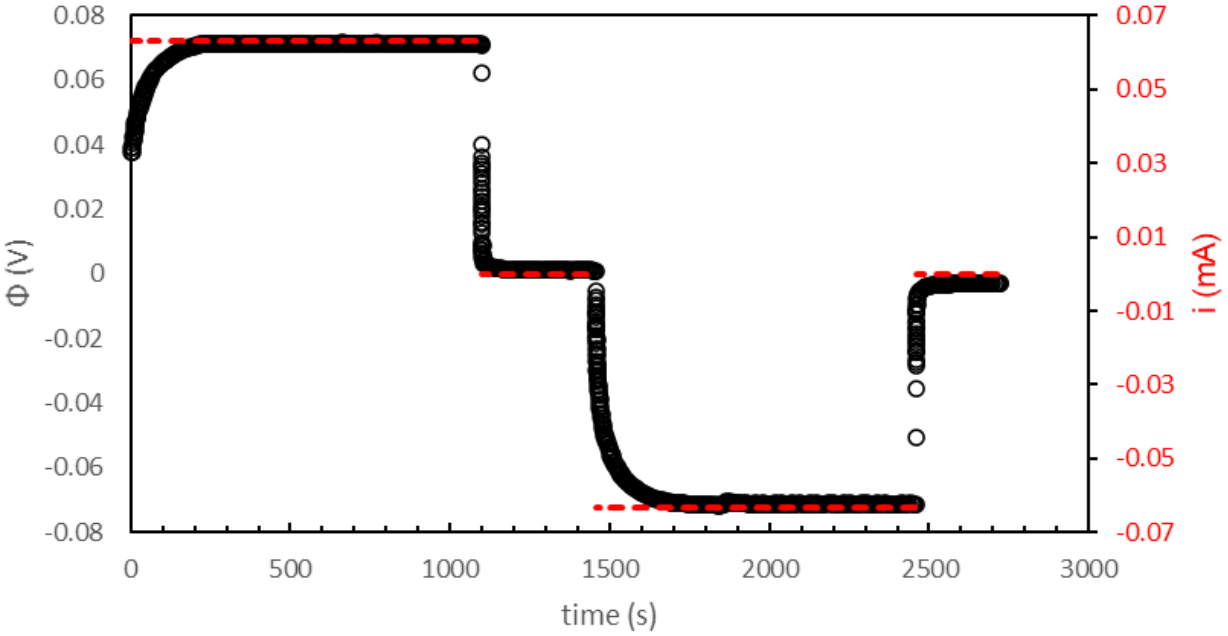

Figure 5.10. Example current experiment in diblock copolymer electrolyte, PEO-POSS(5-2), r = 0.10, at applied current density multiplied by thickness (iL) = 0.01 mA/cm.

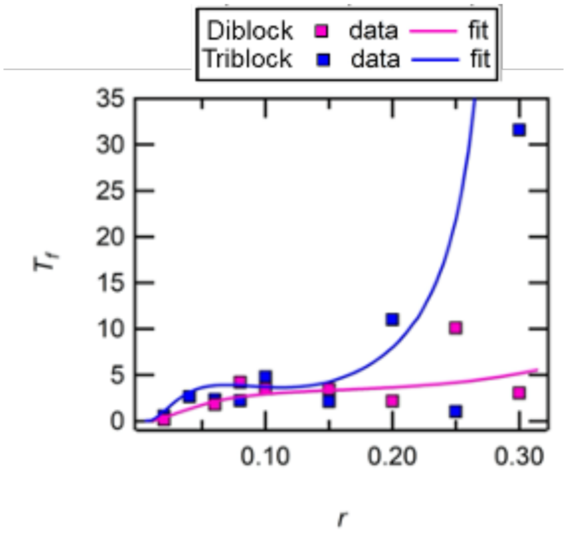

Figure 5.11. Thermodynamic factor (T_f) as a function of salt concentration, r. Fits calculated from Figure 5.4a-d are shown as solid lines through the data.

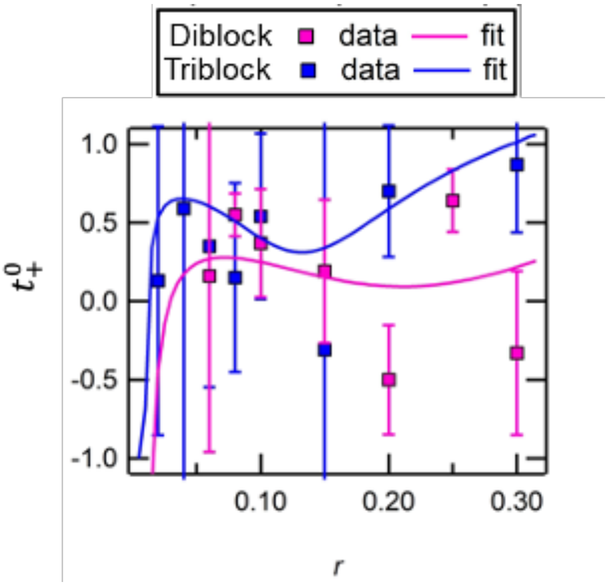

Figure 5.12. Transference number (t_+^0) as a function of salt concentration (r). Fits calculated from Figure 5.4a-d are shown as solid lines through the data.

LIST OF SYMBOLS

a	electrolyte area (cm^2)
A_κ	ionic conductivity versus salt concentration expression prefactor
$A_{\rho+}$	first fitting parameter cation current fraction versus salt concentration expression
A_D	first fitting parameter salt diffusion coefficient versus salt concentration expression
A_U	first fitting parameter open circuit potential versus salt concentration expression
B_κ	ionic conductivity versus salt concentration expression exponential factor
$B_{\rho+}$	second fitting parameter cation current fraction versus salt concentration expression
B_D	second fitting parameter salt diffusion coefficient versus salt concentration expression
B_U	second fitting parameter open circuit potential versus salt concentration expression
$C_{\rho+}$	third fitting parameter cation current fraction versus salt concentration expression
C_D	third fitting parameter salt diffusion coefficient versus salt concentration expression
C_U	third fitting parameter open circuit potential versus salt concentration expression
d	domain spacing (nm) at 90 °C

D	salt diffusion coefficient (cm/s)
f_{DIS}	fraction of disordered phase
f_{EO}	volume fraction of the PEO block
$f_{EO/LiTFSI}$	volume fraction of the PEO/LiTFSI-rich block
f_{ilim}	fraction of current density to theoretical limiting current density
i	current density (mA/cm^2)
i_{lim}	limiting current density (mA/cm^2)
$i_{lim,th}$	theoretical limiting current density (mA/cm^2)
J_1	integrand expression for spatially determined salt concentration expression
J_2	integrand expression for spatially dependent steady-state potential
L	thickness of the electrolyte (cm)
m	molality (mol/kg)
M_{PEO}	molecular weight of the PEO block (kg/mol)
M_{POSS}	molecular weight of the POSS block (kg/mol)
N	chain length calculated at 120 °C and monomer reference volume of 0.1 nm^3
q	magnitude of scattering vector (nm^{-1})
q^*	magnitude of scattering vector at the primary scattering peak (nm^{-1})
r	salt concentration equal to the ratio of lithium to ethylene oxide moieties
r_{av}	average electrolyte ratio of lithium to ethylene oxide moieties
r_{sp}	spatially determined ratio of lithium to ethylene oxide moieties
R_i	interfacial resistance (Ω)
U	concentration cell open circuit potential (V)
v_+	number of cations in salt
x	position in electrolyte (cm)
z_+	charge number of cation

GREEK

κ	ionic conductivity (S/cm^2)

ρ_+	cation current fraction
Φ	cell potential (V)
Φ_f	cell potential corrected for interfacial impedances (V)
$\Delta\Phi_{ss}$	steady-state potential (V)
θ	SAXS scattering angle
λ	SAXS wavelength (nm)

6. Conclusions

Hybrid organic-inorganic block copolymer electrolytes are of interest to enable batteries containing lithium metal anodes. The conductive block is a standard polymer electrolyte of poly(ethylene oxide) and the mechanically rigid block is an inorganic poly(acryloisobutyl polyhedral oligomeric silsesquioxane) polymer. Polymers are mixed with lithium bis(trifluoromethanesulfonyl)imide salt

In this dissertation, the structure-properties relationship of hybrid inorganic-organic block copolymer electrolytes were examined at different temperature (T) and salt concentration (r). In Chapter 2, one PEO-POSS diblock copolymer was mixed with varying amounts of LiTFSI. The phase behavior was studied using small angle X-ray scattering (SAXS) and TEM. The neat polymer exhibited a classical order-to-disorder phase transition. When a small amount of salt is added, the phase transition from disorder-to-order is seen. As more salt is added, a lamellar to coexisting lamellar and hexagonally packed cylinders phase transition upon heating is seen. At the highest salt concentrations, we see a singular lamellar phase. We show that the ionic conductivity is greater than the all-organic counterpart, poly(styrene)-*block*-poly(ethylene oxide) (SEO) at all salt concentrations. The storage modulus is about 4 orders of magnitude greater than SEO.

Chapter 3 examines the phase behavior using SAXS and TEM in 4 PEO-POSS diblock copolymers with the same chain length of PEO and POSS units ranging from 1 to 4. Salt concentration is varied from $0 \leq [\mathrm{Li}]/[\mathrm{EO}] = r \leq 0.3$ and temperature is varied from $60\ ^{\circ}\mathrm{C} \leq T \leq 140\ ^{\circ}\mathrm{C}$. The same phase transitions are seen as those described in Chapter 2. Leibler's Random Phase Approximation is employed to extract the segregation strength in disordered SAXS profiles and create a universal expression for an effective interaction parameter χ_{eff} with two adjustable parameters (T,r). The phase behavior of PEO-POSS is plotted on a phase diagram wherein the x-axis is volume fraction of the conducting block and the y-axis is the segregation strength. The phase behavior falls onto contiguous regions of this diagram.

Chapter 4 examines the molecular underpinnings of the phase behavior of PEO-POSS and POSS-PEO-POSS/salt mixtures. The crystallization effect of the POSS block is examined in the experimental window wherein the PEO block is amorphous. Wide angle X-ray scattering in conjunction with differential scanning calorimetry is used to elucidate the effect of block structure, salt concentration, and chain length on the POSS block crystal structure, crystallization temperature, and percent crystallinity. SAXS is used to compare the phase transition temperatures to crystallization and melting temperatures as well as domain spacing of coexisting phases.

Chapter 5 investigates the effect of morphology on limiting current density in PEO-POSS and POSS-PEO-POSS copolymer electrolytes. Lithium/lithium symmetric cells are used to determine the experimental limiting current density. The diblock and triblock copolymer electrolytes were fully characterized using electrochemical methods to determine the ionic conductivity, cation current fraction, salt diffusion coefficient, and open circuit voltage as a function of salt concentration. SAXS was used to determine the morphology as a function of *r*. Cell potential and salt concentration as functions of position in the cell at various current densities were calculated using Newman's concentrated solution theory. There is quantitative agreement between experimental measurements and theoretical predictions for the limiting current density in PEO-POSS which has an ordered structure at all salt concentrations, while the experimental limiting current density is lower than the theoretical prediction for the POSS-PEO-POSS electrolyte, which exhibits a disordered morphology at high salt concentrations.

References

1. Ma, S., Lin, M., Lin, T. E., Lan, T., Liao, X., Maréchal, F., Van herle, J., Yang, Y., Dong, C. & Wang, L. Fuel cell-battery hybrid systems for mobility and off-grid applications: A review. *Renew. Sustain. Energy Rev.* **135,** (2021).

2. Abas, N., Kalair, A. & Khan, N. Review of fossil fuels and future energy technologies. *Futures* **69,** 31–49 (2015).

3. Sorrell, S. Reducing energy demand: A review of issues, challenges and approaches. *Renew. Sustain. Energy Rev.* **47,** 74–82 (2015).

4. Scrosati, B. Advanced lithium ion battery materials. *Ionics (Kiel).* **6,** 127–132 (2000).

5. Bazak, J. D., Allen, J. P., Krachkovskiy, S. A. & Goward, G. R. Mapping of Lithium-Ion Battery Electrolyte Transport Properties and Limiting Currents with In Situ MRI. *J. Electrochem. Soc.* **167,** 140518 (2020).

6. Lu, L., Han, X., Li, J., Hua, J. & Ouyang, M. A review on the key issues for lithium-ion battery management in electric vehicles. *J. Power Sources* **226,** 272–288 (2013).

7. Bandhauer, T. M., Garimella, S. & Fuller, T. F. A Critical Review of Thermal Issues in Lithium-Ion Batteries. *J. Electrochem. Soc.* **158,** R1 (2011).

8. Lisbona, D. & Snee, T. A review of hazards associated with primary lithium and lithium-ion batteries. *Process Saf. Environ. Prot.* **89,** 434–442 (2011).

9. Qian, J., Henderson, W. A., Xu, W., Bhattacharya, P., Engelhard, M., Borodin, O. & Zhang, J. G. High rate and stable cycling of lithium metal anode. *Nat. Commun.* **6,** (2015).

10. Lin, D., Liu, Y. & Cui, Y. Reviving the lithium metal anode for high-energy batteries. *Nat. Nanotechnol.* **12,** 194–206 (2017).

11. Kim, W. S. & Yoon, W. Y. Observation of dendritic growth on Li powder anode using optical cell. *Electrochim. Acta* **50,** 541–545 (2004).

12. Love, C. T., Baturina, O. A. & Swider-Lyons, K. E. Observation of lithium dendrites at ambient temperature and below. *ECS Electrochem. Lett.* **4,** A24–A27 (2014).

13. Sun, F., Zielke, L., Markötter, H., Hilger, A., Zhou, D., Moroni, R., Zengerle, R., Thiele, S., Banhart, J. & Manke, I. Morphological Evolution of Electrochemically Plated/Stripped Lithium Microstructures Investigated by Synchrotron X-ray Phase Contrast Tomography. *ACS Nano* **10,** 7990–7997 (2016).

14. Steiger, J., Richter, G., Wenk, M., Kramer, D. & Mönig, R. Comparison of the growth of lithium filaments and dendrites under different conditions. *Electrochem. commun.* **50,** 11–14 (2015).

15. Schauser, N. S., Harry, K. J., Parkinson, D. Y., Watanabe, H. & Balsara, N. P. Lithium

Dendrite Growth in Glassy and Rubbery Nanostructured Block Copolymer Electrolytes. *J. Electrochem. Soc.* **162,** A398–A405 (2014).

16. Harry, K. J., Hallinan, D. T., Parkinson, D. Y., MacDowell, A. A. & Balsara, N. P. Detection of subsurface structures underneath dendrites formed on cycled lithium metal electrodes. *Nat. Mater.* **13,** 69–73 (2014).

17. Brissot, C., Rosso, M., Chazalviel, J.-N., Baudry, P. & Lascaud, S. In situ study of dendritic growth inlithium/PEO-salt/lithium cells. *Electrochim. Acta* **43,** 1569–1574 (1998).

18. Pei, A., Zheng, G., Shi, F., Li, Y. & Cui, Y. Nanoscale Nucleation and Growth of Electrodeposited Lithium Metal. *Nano Lett.* **17,** 1132–1139 (2017).

19. Harry, K. J., Higa, K., Srinivasan, V. & Balsara, N. P. Influence of Electrolyte Modulus on the Local Current Density at a Dendrite Tip on a Lithium Metal Electrode. *J. Electrochem. Soc.* **163,** A2216–A2224 (2016).

20. Cheng, X. B., Zhang, R., Zhao, C. Z. & Zhang, Q. Toward Safe Lithium Metal Anode in Rechargeable Batteries: A Review. *Chem. Rev.* **117,** 10403–10473 (2017).

21. Agrawal, R. C. & Pandey, G. P. Solid polymer electrolytes: Materials designing and all-solid-state battery applications: An overview. *J. Phys. D. Appl. Phys.* **41,** (2008).

22. Zhou, W., Li, Y., Xin, S. & Goodenough, J. B. Rechargeable Sodium All-Solid-State Battery. *ACS Cent. Sci.* **3,** 52–57 (2017).

23. Seitzman, N., Guthrey, H., Sulas, D. B., Platt, H. A. S., Al-Jassim, M. & Pylypenko, S. Toward All-Solid-State Lithium Batteries: Three-Dimensional Visualization of Lithium Migration in β-Li 3 PS 4 Ceramic Electrolyte. *J. Electrochem. Soc.* **165,** A3732–A3737 (2018).

24. Hallinan, D. T., Villaluenga, I. & Balsara, N. P. Polymer and composite electrolytes. *MRS Bull.* **43,** 759–767 (2018).

25. Croce, F., Appetecchi, G. B., Persi, L. & Scrosati, B. Nanocomposite polymer electrolytes for lithium batteries. *Nature* **394,** 456–458 (1998).

26. Ren, Y., Shen, Y., Lin, Y. & Nan, C. W. Direct observation of lithium dendrites inside garnet-type lithium-ion solid electrolyte. *Electrochem. commun.* **57,** 27–30 (2015).

27. Cheng, E. J., Sharafi, A. & Sakamoto, J. Intergranular Li metal propagation through polycrystalline Li6.25Al0.25La3Zr2O12 ceramic electrolyte. *Electrochim. Acta* **223,** 85–91 (2017).

28. Bruce, P. G. & Gray., F. M. *Polymer electrolytes II: physical principles.* (1995).

29. Kim, J., Jung, H. Y. & Park, M. J. End-Group Chemistry and Junction Chemistry in Polymer Science: Past, Present, and Future. *Macromolecules* **53,** 746–763 (2020).

30. Panday, A., Mullin, S., Gomez, E. D., Wanakule, N., Chen, V. L., Hexemer, A., Pople, J. & Balsara, N. P. Effect of molecular weight and salt concentration on conductivity of block copolymer electrolytes. *Macromolecules* **42,** 4632–4637 (2009).

31. Fenton, D. E., Parker, J. M. & Wright, P. V. Complexes of alkali metal ions with poly(ethylene oxide). *Polymer (Guildf).* **14,** 589 (1973).

32. J.R. MacCallum, C. A. V. Polymer Electrolyte Reviews, Volume 1. 351 (1987). doi:10.1002/pi.4980200325

33. Edman, L., Doeff, M. M., Ferry, A., Kerr, J. & De Jonghe, L. C. Transport properties of the solid polymer electrolyte system P(EO)nLiTFSI. *J. Phys. Chem. B* **104,** 3476–3480 (2000).

34. MacGlashan, G. S. & Andreev, Y. G. Structure of the polymer electrolyte poly (ethylene oxide) 6: LiAsF6. *Nature* **398,** 792–794 (1999).

35. Diddens, D., Heuer, A. & Borodin, O. Understanding the lithium transport within a rouse-based model for a PEO/LiTFSI polymer electrolyte. *Macromolecules* **43,** 2028–2036 (2010).

36. Shi, J. & Vincent, C. A. The effect of molecular weight on cation mobility in polymer electrolytes. *Solid State Ionics* **60,** 11–17 (1993).

37. Gao, K. W. & Balsara, N. P. Electrochemical properties of poly (ethylene oxide) above the entanglement threshold. **364,** (2021).

38. Newman, J. & Balsara, N. P. *Electrochemical Systems*. (John Wiley & Sons, Ltd, 2021).

39. Pesko, D. M., Timachova, K., Bhattacharya, R., Smith, M. C., Villaluenga, I., Newman, J. & Balsara, N. P. Negative Transference Numbers in Poly(ethylene oxide)-Based Electrolytes. *J. Electrochem. Soc.* **164,** E3569–E3575 (2017).

40. Gribble, D. A., Frenck, L., Shah, D. B., Maslyn, J. A., Loo, W. S., Mongcopa, K. I. S., Pesko, D. M. & Balsara, N. P. Comparing Experimental Measurements of Limiting Current in Polymer Electrolytes with Theoretical Predictions. *J. Electrochem. Soc.* **166,** A3228–A3234 (2019).

41. Mongcopa, K. I. S., Tyagi, M., Mailoa, J. P., Samsonidze, G., Kozinsky, B., Mullin, S. A., Gribble, D. A., Watanabe, H. & Balsara, N. P. Relationship between Segmental Dynamics Measured by Quasi-Elastic Neutron Scattering and Conductivity in Polymer Electrolytes. *ACS Macro Lett.* **7,** 504–508 (2018).

42. Monroe, C. & Newman, J. Dendrite Growth in Lithium/Polymer Systems A Propagation Model for Liquid Electrolytes under Galvanostatic Conditions. *J. Electrochem. Soc.* **150,** A1377–A1384 (2003).

43. Monroe, C. & Newman, J. The Impact of Elastic Deformation on Deposition Kinetics at Lithium/Polymer Interfaces. *J. Electrochem. Soc.* **152,** A396 (2005).

44. Barai, P., Higa, K. & Srinivasan, V. Effect of Initial State of Lithium on the Propensity for Dendrite Formation: A Theoretical Study. *J. Electrochem. Soc.* **164,** A180–A189 (2017).

45. Kraus, G. & Gruver, J. T. Properties of random and block copolymers of butadiene and styrene. II. Melt flow. *J. Appl. Polym. Sci.* **11,** 2121–2129 (1967).

46. Bates, F. S. Polymer-Polymer Phase Behavior. **251,** (1990).

47. Bates, F. S., Cohen, R. E. & Berney, C. V. Small-Angle Neutron Scattering Determination of Macrolattice Structure in a Polystyrene-Polybutadiene Diblock Copolymer. *Macromolecules* **15,** 589–592 (1982).

48. Singh, M., Odusanya, O., Wilmes, G. M., Eitouni, H. B., Gomez, E. D., Patel, A. J., Chen, V. L., Park, M. J., Fragouli, P., Iatrou, H., Hadjichristidis, N., Cookson, D. & Balsara, N. P. Effect of molecular weight on the mechanical and electrical properties of block copolymer electrolytes. *Macromolecules* **40,** 4578–4585 (2007).

49. Bouchet, R., Phan, T. N. T., Beaudoin, E., Devaux, D., Davidson, P., Bertin, D. & Denoyel, R. Charge transport in nanostructured PS-PEO-PS triblock copolymer electrolytes. *Macromolecules* **47,** 2659–2665 (2014).

50. Sethuraman, V., Mogurampelly, S. & Ganesan, V. Multiscale Simulations of Lamellar PS-PEO Block Copolymers Doped with LiPF6 Ions. *Macromolecules* **50,** 4542–4554 (2017).

51. Fauré, M. C., Bassereau, P., Lee, L. T., Menelle, A. & Lheveder, C. Phase transitions in monolayers of PS-PEO copolymer at the air-water interface. *Macromolecules* **32,** 8538–8550 (1999).

52. Utpalla, P., Sharma, S. K., Deshpande, S. K., Bahadur, J., Sen, D., Sahu, M. & Pujari, P. K. Role of free volumes and segmental dynamics on ion conductivity of PEO/LiTFSI solid polymer electrolytes filled with SiO 2 nanoparticles: a positron annihilation and broadband dielectric spectroscopy study . *Phys. Chem. Chem. Phys.* **23,** 8585–8597 (2021).

53. Blanco, I. The rediscovery of POSS: A molecule rather than a filler. *Polymers (Basel).* **10,** (2018).

54. Ayandele, E., Sarkar, B. & Alexandridis, P. Polyhedral Oligomeric Silsesquioxane (POSS)-Containing Polymer Nanocomposites. *Nanomaterials* **2,** 445–475 (2012).

55. Berthier, C., Gorecki, W., Minier, M., Armand, M. B., Chabagno, J. M. & Rigaud, P. Microscopic investigation of ionic conductivity in alkali metal salts-poly(ethylene oxide) adducts. *Solid State Ionics* **11,** 91–95 (1983).

56. Bouchet, R., Maria, S., Meziane, R., Aboulaich, A., Lienafa, L., Bonnet, J. P., Phan, T. N. T., Bertin, D., Gigmes, D., Devaux, D., Denoyel, R. & Armand, M. Single-ion BAB triblock copolymers as highly efficient electrolytes for lithium-metal batteries. *Nat. Mater.* **12,** 452–457 (2013).

57. Armand, M. & Tarascon, J. M. Building better batteries. *Nature* **451,** 652–657 (2008).

58. Devaux, D., Glé, D., Phan, T. N. T., Gigmes, D., Giroud, E., Deschamps, M., Denoyel, R. & Bouchet, R. Optimization of Block Copolymer Electrolytes for Lithium Metal Batteries. *Chem. Mater.* **27,** 4682–4692 (2015).

59. Gomez, E. D., Panday, A., Feng, E. H., Chen, V., Stone, G. M., Minor, A. M., Kisielowski, C., Downing, K. H., Borodin, O., Smith, G. D. & Balsara, N. P. Effect of ion distribution on conductivity of block copolymer electrolytes. *Nano Lett.* **9,** 1212–1216 (2009).

60. Oparaji, O., Narayanan, S., Sandy, A., Ramakrishnan, S. & Hallinan, D. Structural Dynamics of Strongly Segregated Block Copolymer Electrolytes. *Macromolecules* **51,** 2591–2603 (2018).

61. Wanakule, N. S., Virgili, J. M., Teran, A. A., Wang, Z. G. & Balsara, N. P. Thermodynamic properties of block copolymer electrolytes containing imidazolium and lithium salts. *Macromolecules* **43,** 8282–8289 (2010).

62. Loo, W. S., Galluzzo, M. D., Li, X., Maslyn, J. A., Oh, H. J., Mongcopa, K. I. S., Zhu, C., Wang, A. A., Wang, X., Garetz, B. A. & Balsara, N. P. Phase Behavior of Mixtures of Block Copolymers and a Lithium Salt. *J. Phys. Chem. B* **122,** acs.jpcb.8b04189 (2018).

63. Russell, T. P., Karis, T. E., Gallot, Y. & Mayes, A. M. A lower critical ordering transition in a diblock copolymer melt. *Nature* **368,** 729–731 (1994).

64. Ruzette, A.-V. G., Banerjee, P., Mayes, A. M., Pollard, M., Russell, T. P., Jerome, R., Slawecki, T., Hjelm, R. & Thiyagarajan, P. Phase Behavior of Diblock Copolymers between Styrene and *n* -Alkyl Methacrylates. *Macromolecules* **31,** 8509–8516 (1998).

65. Yeh, C. L., Hou, T., Chen, H. L., Yeh, L. Y., Chiu, F. C., M??ller, A. J. & Hadjichristidis, N. Lower critical ordering transition of poly(ethylene oxide)-block-poly(2- vinylpyridine). *Macromolecules* **44,** 440–443 (2011).

66. Mulhearn, W. D. & Register, R. A. Lower critical ordering transition of an all-hydrocarbon polynorbornene diblock copolymer. *ACS Macro Lett.* **6,** 808–812 (2017).

67. Sakamoto, N. & Hashimoto, T. Order-Disorder Transition of Low Molecular Weight Polystyrene-block-Polyisoprene. 1. SAXS Analysis of Two Characteristic Temperatures. *Macromolecules* **28,** 6825–6834 (1995).

68. Leibler, L. Theory of Microphase Separation in Block Copolymers. *Macromolecules* **13,** 1602–1617 (1980).

69. Fredrickson, G. H. & Helfand, E. Fluctuation effects in the theory of microphase separation in block copolymers. *J. Chem. Phys.* **87,** 697–705 (1987).

70. Bates, F. S., Rosedale, J. H. & Fredrickson, G. H. Fluctuation effects in a symmetric diblock copolymer near the order-disorder transition. *J. Chem. Phys.* **92,** 6255–6270 (1990).

71. Haris, T. E., Russell, T. P., Gallot, Y. & Mayes, A. M. Rheology of the Lower Critical Ordering Transition. *Macromolecules* **28,** 1129–1134 (1995).

72. Pollard, M., Russell, T. P., Ruzette, A. V., Mayes, A. M. & Gallot, Y. The effect of hydrostatic pressure on the lower critical ordering transition in diblock copolymers. *Macromolecules* **31,** 6493–6498 (1998).

73. Ryu, D. Y., Shin, C., Cho, J., Lee, D. H., Kim, J. K., Lavery, K. A. & Russell, T. P. Effective interaction parameter for homologous series of deuterated polystyrene-block-poly(n-alkyl methacrylate) copolymers. *Macromolecules* **40,** 7644–7655 (2007).

74. Loo, W. S., Jiang, X., Maslyn, J. A., Oh, H. J., Zhu, C., Downing, K. H. & Balsara, N. P.

Reentrant phase behavior and coexistence in asymmetric block copolymer electrolytes. *Soft Matter* **14,** 2789–2795 (2018).

75. Teran, A. A. & Balsara, N. P. Thermodynamics of block copolymers with and without salt. *J. Phys. Chem. B* **118,** 4–17 (2014).

76. Young, W. S. & Epps, T. H. Salt doping in PEO-containing block copolymers: Counterion and concentration effects. *Macromolecules* **42,** 2672–2678 (2009).

77. Gunkel, I. & Thurn-Albrecht, T. Thermodynamic and structural changes in ion-containing symmetric diblock copolymers: A small-angle X-ray scattering study. *Macromolecules* **45,** 283–291 (2012).

78. Nakamura, I. & Wang, Z.-G. Salt-doped block copolymers: ion distribution, domain spacing and effective χ parameter. *Soft Matter* **8,** 9356 (2012).

79. Mai, S. M., Fairclough, J. P. A., Hamley, I. W., Matsen, M. W., Denny, R. C., Liao, B. X., Booth, C. & Ryan, A. J. Order-disorder transition in poly(oxyethylene)-poly(oxybutylene) diblock copolymers. *Macromolecules* **29,** 6212–6221 (1996).

80. Qin, J. & De Pablo, J. J. Ordering Transition in Salt-Doped Diblock Copolymers. *Macromolecules* **49,** 3630–3638 (2016).

81. Schulze, M. W., McIntosh, L. D., Hillmyer, M. A. & Lodge, T. P. High-modulus, high-conductivity nanostructured polymer electrolyte membranes via polymerization-induced phase separation. *Nano Lett.* **14,** 122–126 (2014).

82. Almdal, K., koppi, K. A., Bates, F. S. & Mortensen, K. Multiple Ordered Phases in a Block Copolymer Melt. *Macromolecules* **25,** 1743–1751 (1992).

83. Hasegawa, H., Tanaka, H., Yamasaki, K. & Hashimoto, T. Bicontinuous Microdomain Morphology of Block Copolymers: 1: Tetrapod-Network Structure of Polystyrene-Polyisoprene Diblock Polymers. *Macromolecules* **20,** 1651–1662 (1987).

84. Bates, F. S. & Fredrickson, G. H. Block copolymers-designer soft materials. *Phys. Today* **52,** 32–38 (1999).

85. Lascaud, S., Perrier, M., Vallée, A., Besner, S., Prud'homme, J. & Armand, M. Phase Diagrams and Conductivity Behavior of Poly(ethylene oxide)-Molten Salt Rubbery Electrolytes. *Macromolecules* **27,** 7469–7477 (1994).

86. Chintapalli, M., Le, T. N. P., Venkatesan, N. R., Mackay, N. G., Rojas, A. A., Thelen, J. L., Chen, X. C., Devaux, D. & Balsara, N. P. Structure and Ionic Conductivity of Polystyrene-block-poly(ethylene oxide) Electrolytes in the High Salt Concentration Limit. *Macromolecules* **49,** 1770–1780 (2016).

87. Kim, S. K., Kim, D. G., Lee, A., Sohn, H. S., Wie, J. J., Nguyen, N. A., MacKay, M. E. & Lee, J. C. Organic/inorganic hybrid block copolymer electrolytes with nanoscale ion-conducting channels for lithium ion batteries. *Macromolecules* **45,** 9347–9356 (2012).

88. Liu, Y., Ma, X., Sun, K., Yang, K. & Chen, F. Preparation and characterization of gel polymer electrolyte based on electrospun polyhedral oligomeric silsesquioxane-

poly(methyl methacrylate)8/polyvinylidene fluoride hybrid nanofiber membranes for lithium-ion batteries. *J. Solid State Electrochem.* **22,** 581–590 (2018).

89. Zhang, J., Ma, C., Liu, J., Chen, L., Pan, A. & Wei, W. Solid polymer electrolyte membranes based on organic/inorganic nanocomposites with star-shaped structure for high performance lithium ion battery. *J. Memb. Sci.* **509,** 138–148 (2016).

90. Lee, J. Y., Lee, Y. M., Bhattacharya, B., Nho, Y. C. & Park, J. K. Solid polymer electrolytes based on crosslinkable polyoctahedral silsesquioxanes (POSS) for room temperature lithium polymer batteries. *J. Solid State Electrochem.* **14,** 1445–1449 (2010).

91. Polu, A. R. & Rhee, H. W. Nanocomposite solid polymer electrolytes based on poly(ethylene oxide)/POSS-PEG (n=13.3) hybrid nanoparticles for lithium ion batteries. *J. Ind. Eng. Chem.* **31,** 323–329 (2015).

92. Mansky, P., Tsui, O. K. C., Russell, T. P. & Gallot, Y. Phase coherence and microphase separation transitions in diblock copolymer thin films. *Macromolecules* **32,** 4832–4837 (1999).

93. Fischer, H., Weidisch, R., Stamm, M., Budde, H. & Höring, S. The phase diagram of the system poly (styrene-block-n-butyl methacrylate). *Colloid Polym. Sci.* **278,** 1019–1031 (2000).

94. Gee, G. & Flory, P. J. Statistical Thermodynamics of Semi-Flexible Chain Molecules. *Proc. R. Soc. A Math. Phys. Eng. Sci.* **234,** 60–73 (1956).

95. Douglas Whitmore, M. & Noolandi, J. Theory of Crystallizable Block Copolymer Blends. *Macromolecules* **21,** 1482–1496 (1988).

96. Zhu, L., Cheng, S. Z. D., Calhoun, B. H., Ge, Q., Quirk, R. P., Thomas, E. L., Hsiao, B. S., Yeh, F. & Lotz, B. Crystallization temperature-dependent crystal orientations within nanoscale confined lamellae of a self-assembled crystalline - Amorphous diblock copolymer. *J. Am. Chem. Soc.* **122,** 5957–5967 (2000).

97. Keller, A. & Machin, M. J. Oriented Crystallization in Polymers. *J. Macromol. Sci. Part B* **1,** 41–91 (1967).

98. Wu, K., Huang, M., Yue, K., Liu, C., Lin, Z., Liu, H., Zhang, W., Hsu, C. H., Shi, A. C., Zhang, W. Bin & Cheng, S. Z. D. Asymmetric giant 'bolaform-like' surfactants: Precise synthesis, phase diagram, and crystallization-induced phase separation. *Macromolecules* **47,** 4622–4633 (2014).

99. Rangarajan, P., Register, R. A., Adamson, D. H., Fetters, L. J., Bras, W., Naylor, S. & Ryan, A. J. Dynamics of Structure Formation in Crystallizable Block Copolymers. *Macromolecules* **28,** 1422–1428 (1995).

100. Gervais, M. & Gallot, B. Phase Diagram and Structural Study of Polystyrene - Poly(ethy1ene oxide) Block Copolymers, 1. *Die Makromol. Chemie* **178,** 157–178 (1973).

101. Rangarajan, P., Register, R. A. & Fetters, L. J. Morphology of Semicrystalline Block Copolymers of Ethylene-(Ethylene-alt-propylene). *Macromolecules* **26,** 4640–4645 (1993).

102. Bates, F. S. & Fredrickson, G. H. Block Copolymer Thermodynamics: Theory And Experiment. *Annu. Rev. Phys. Chem.* **41,** 525–557 (1990).

103. Mayes, A. M. & Olvera De La Cruz, M. Concentration fluctuation effects on disorder-order transitions in block copolymer melts. *J. Chem. Phys.* **95,** 4670–4677 (1991).

104. Giles, J. R. M., Gray, F. M., MacCallum, J. R. & Vincent, C. A. Synthesis and characterization of ABA block copolymer-based polymer electrolytes. *Polymer (Guildf).* **28,** 1977–1981 (1987).

105. Lin, C. C., Jonnalagadda, S. V., Kesani, P. K., Dai, H. J. & Balsara, N. P. Effect of Molecular Structure on the Thermodynamics of Block Copolymer Melts. *Macromolecules* **27,** 7769–7780 (1994).

106. Matsen, M. W. & Thompson, R. B. Equilibrium behavior of asymmetric ABA triblock copolymer melts. *J. Chem. Phys.* **113,** 5539–5544 (2000).

107. Chakraborty, S., Jiang, X., Ho, Z. J., Sethi, G. K., Zhu, C. & Balsara, N. P. Reversible Changes in the Grain Structure and Conductivity in a Block Copolymer Electrolyte. (2020). doi:10.1021/acs.macromol.0c00466

108. Sethi, G. K., Jiang, X., Chakraborty, R., Loo, W. S., Villaluenga, I. & Balsara, N. P. Anomalous Self-Assembly and Ion Transport in Nanostructured Organic–Inorganic Solid Electrolytes. *ACS Macro Lett.* 1056–1061 (2018). doi:10.1021/acsmacrolett.8b00583

109. Ilavsky, J. Nika: Software for two-dimensional data reduction. *J. Appl. Crystallogr.* **45,** 324–328 (2012).

110. Liu, H., Luo, J., Shan, W., Guo, D., Wang, J., Hsu, C. H., Huang, M., Zhang, W., Lotz, B., Zhang, W. Bin, Liu, T., Yue, K. & Cheng, S. Z. D. Manipulation of Self-Assembled Nanostructure Dimensions in Molecular Janus Particles. *ACS Nano* **10,** 6585–6596 (2016).

111. Lichtenhan, J. D., Otonari, Y. A. & Carr, M. J. Linear Hybrid Polymer Building Blocks: Methacrylate-Functionalized Polyhedral Oligomeric Silsesquioxane Monomers and Polymers. *Macromolecules* **28,** 8435–8437 (1995).

112. Miao, J., Cui, L., Lau, H. P., Mather, P. T. & Zhu, L. Self-assembly and chain-folding in hybrid coil-coil-cube triblock oligomers of polyethylene-b-poly(ethylene oxide)-b-polyhedral oligomeric silsesquioxane. *Macromolecules* **40,** 5460–5470 (2007).

113. Zheng, L., Waddon, A. J., Farris, R. J. & Coughlin, E. B. X-ray characterizations of polyethylene polyhedral oligomeric silsesquioxane copolymers. *Macromolecules* **35,** 2375–2379 (2002).

114. Waddon, A. J., Zheng, L., Farris, R. J. & Coughlin, E. B. Nanostructured Polyethylene-POSS Copolymers: Control of Crystallization and Aggregation. *Nano Lett.* **2,** 1149–1155 (2002).

115. Waddon, A. J. & Coughlin, E. B. Crystal Structure of Polyhedral Oligomeric Silsequioxane (POSS) Nano-materials: A Study by X-ray Diffraction and Electron Microscopy. *Chem. Mater.* **15,** 4555–4561 (2003).

116. Larsson, K. Larsson, K. Ark. Kemi 1960, 16, 203. *Ark. Kemi* **16,** 203 (1960).

117. Barry, A. J., Daudt, W. H., Domicone, J. J. & Gilkey, J. W. Crystalline Organosilsesquioxanes. *J. Am. Chem. Soc.* **77,** 4248–4252 (1955).

118. Mather, P. T., Jeon, H. G., Romo-Uribe, A., Haddad, T. S. & Lichtenhan, J. D. Mechanical Relaxation and Microstructure of Poly(norbornyl-POSS) Copolymers. *Macromolecules* **32,** 1194–1203 (1999).

119. Li, X., Loo, W. S., Jiang, X., Wang, X., Galluzzo, M. D., Mongcopa, K. I., Wang, A. A., Balsara, N. P. & Garetz, B. A. Confined versus Unconfined Crystallization in Block Copolymer/Salt Mixtures Studied by Depolarized Light Scattering. *Macromolecules* **52,** 982–991 (2019).

120. Thelen, J. L., Wang, A. A., Chen, X. C., Jiang, X., Schaible, E. & Balsara, N. P. Correlations between Salt-Induced Crystallization, Morphology, Segmental Dynamics, and Conductivity in Amorphous Block Copolymer Electrolytes. *Macromolecules* **51,** 1733–1740 (2018).

121. Pielichowski, K. & Flejtuch, K. Differential scanning calorimetry studies on poly(ethylene glycol) with different molecular weights for thermal energy storage materials. *Polym. Adv. Technol.* **13,** 690–696 (2002).

122. Mayes, A. M. & Olvera De La Cruz, M. Microphase separation in multiblock copolymer melts. *J. Chem. Phys.* **91,** 7228–7235 (1989).

123. Wang, C., Li, X. & Deng, H. Synthesis of a Fluoromethacrylate Hydroxystyrene Block Copolymer Capable of Rapidly Forming Sub-5 nm Domains at Low Temperatures. *ACS Macro Lett.* **8,** 368–373 (2019).

124. Borodin, O. & Smith, G. D. Mechanism of ion transport in amorphous poly(ethylene oxide)/ LiTFSI from molecular dynamics simulations. *Macromolecules* **39,** 1620–1629 (2006).

125. Sethi, G. K., Jung, H. Y., Loo, W. S., Sawhney, S., Park, M. J., Balsara, N. P. & Villaluenga, I. Structure and Thermodynamics of Hybrid Organic-Inorganic Diblock Copolymers with Salt. *Macromolecules* **52,** 3165–3175 (2019).

126. Hou, K. J., Loo, W. S., Balsara, N. P. & Qin, J. Comparing Experimental Phase Behavior of Ion-Doped Block Copolymers with Theoretical Predictions Based on Selective Ion Solvation. *Macromolecules* **53,** 3956–3966 (2020).

127. Sing, C. E., Zwanikken, J. W. & Olvera De La Cruz, M. Ion correlation-induced phase separation in polyelectrolyte blends. *ACS Macro Lett.* **2,** 1042–1046 (2013).

128. Nakamura, I. & Wang, Z. G. Thermodynamics of salt-doped block copolymers. *ACS Macro Lett.* **3,** 708–711 (2014).

129. Hou, K. J. & Qin, J. Solvation and Entropic Regimes in Ion-Containing Block Copolymers. *Macromolecules* **51,** 7463–7475 (2018).

130. Mester, Z., Lynd, N. A. & Fredrickson, G. H. Numerical self-consistent field theory of

multicomponent polymer blends in the Gibbs ensemble. *Soft Matter* **9,** 11288–11294 (2013).

131. Epps, T. H., Bailey, T. S., Pham, H. D. & Bates, F. S. Phase behavior of lithium perchlorate-doped poly (styrene-b-isoprene-b-ethylene oxide) triblock copolymers. *Chem. Mater.* **14,** 1706–1714 (2002).

132. Cochran, E. W., Garcia-Cervera, C. J. & Fredrickson, G. H. Stability of the gyroid phase in diblock copolymers at strong segregation. *Macromolecules* **39,** 2449–2451 (2006).

133. Vavasour, J. D. & Whitmore, M. D. Self-Consistent Field Theory of Block Copolymers with Conformational Asymmetry. *Macromolecules* **26,** 7070–7075 (1993).

134. Ehrl, A., Landesfeind, J., Wall, W. A. & Gasteiger, H. A. Determination of Transport Parameters in Liquid Binary Lithium Ion Battery Electrolytes. *J. Electrochem. Soc.* **164,** A826–A836 (2017).

135. Bouridah, A., Dalard, F., Deroo, D. & Armand, M. B. Potentiometric measurements of ionic transport parameters in poly(ethylene oxide)-LiX electrolytes. *J. Appl. Electrochem.* **17,** 625–634 (1987).

136. Galluzzo, M. D., Loo, W. S., Wang, A. A., Walton, A., Maslyn, J. A. & Balsara, N. P. Measurement of Three Transport Coefficients and the Thermodynamic Factor in Block Copolymer Electrolytes with Different Morphologies. *J. Phys. Chem. B* **124,** 921–935 (2020).

137. Bruce, P. G., Hardgrave, M. T. & Vincent, C. A. The determination of transference numbers in solid polymer electrolytes using the Hittorf method. *Solid State Ionics* **53–56,** 1087–1094 (1992).

138. Andrews, S., Evans, J., Vincent, C. A. & Bruce, P. G. Electrochemical measurement of transference numbers in polymer electrolytes. *Polymer (Guildf).* **28,** 2324–2328 (1987).

139. Yanping, M., Doyle, M., Fuller, T. F., Doeff, M. M., Jonghe, L. C. De, Newman, J., Ma, Y., Doyle, M., Fuller, T. F., Doeff, M. M., De Jonghe, L. C. & Newman, J. The Measurement of a Complete Set of Transport Properties for a Concentrated Solid Polymer Electrolyte Solution. *J. Electrochem. Soc.* **142,** 1859 (1995).

140. Chang, H. J., Ilott, A. J., Trease, N. M., Mohammadi, M., Jerschow, A. & Grey, C. P. Correlating Microstructural Lithium Metal Growth with Electrolyte Salt Depletion in Lithium Batteries Using 7 Li MRI. *J. Am. Chem. Soc.* **137,** 15209–15216 (2015).

141. Frenck, L., Sethi, G. K., Maslyn, J. A. & Balsara, N. P. Factors That Control the Formation of Dendrites and Other Morphologies on Lithium Metal Anodes. *Front. Energy Res.* **7,** (2019).

142. Sethi, G. K., Jung, H. Y., Loo, W. S., Sawhney, S., Park, M. J., Balsara, N. P. & Villaluenga, I. Structure and Thermodynamics of Hybrid Organic–Inorganic Diblock Copolymers with Salt. *Macromolecules* acs.macromol.9b00042 (2019). doi:10.1021/acs.macromol.9b00042

143. Sethi, G. K., Chakraborty, S., Zhu, C., Schaible, E., Villaluenga, I. & Balsara, N. P. Effect

of crystallization of the polyhedral oligomeric silsesquioxane block on self-assembly in hybrid organic-inorganic block copolymers with salt. *Giant* **6,** 100055 (2021).

144. Shah, D. B., Kim, H. K., Nguyen, H. Q., Srinivasan, V. & Balsara, N. P. Comparing Measurements of Limiting Current of Electrolytes with Theoretical Predictions up to the Solubility Limit. *J. Phys. Chem. C* **123,** 23872–23881 (2019).

145. Pesko, D. M., Feng, Z., Sawhney, S., Newman, J., Srinivasan, V., Balsara, N. P. & Berkeley, L. Comparing Cycling Characteristics of Symmetric Lithium-Polymer-Lithium Cells with Theoretical Predictions. *J. Electrochem. Soc.* **165,** 3186–3194 (2018).

146. Frenck, L., Veeraraghavan, V. D., Maslyn, J. A., Müller, A., Ho, A. S., Loo, W. S., Minor, A. M. & Balsara, N. P. Effect of salt concentration profiles on protrusion growth in lithium-polymer-lithium cells. *Solid State Ionics* **358,** (2020).

147. Park, J. W., Yoshida, K., Tachikawa, N., Dokko, K. & Watanabe, M. Limiting current density in bis(trifluoromethylsulfonyl)amide-based ionic liquid for lithium batteries. *J. Power Sources* **196,** 2264–2268 (2011).

148. Lee, S. I., Jung, U. H., Kim, Y. S., Kim, M. H., Ahn, D. J. & Chun, H. S. A study of electrochemical kinetics of lithium ion in organic electrolytes. *Korean J. Chem. Eng.* **19,** 638–644 (2002).

149. Georén, P. & Lindbergh, G. Characterisation and modelling of the transport properties in lithium battery polymer electrolytes. *Electrochim. Acta* **47,** 577–587 (2001).

150. Bequette, B. *Process control: modeling, design, and simulation*. (2003).

151. Ugata, Y., Thomas, M. L., Mandai, T., Ueno, K., Dokko, K. & Watanabe, M. Li-ion hopping conduction in highly concentrated lithium bis(fluorosulfonyl)amide/dinitrile liquid electrolytes. *Phys. Chem. Chem. Phys.* **21,** 9759–9768 (2019).